
DEVELOPMENT OF MECHANISTIC MODELS OF TWO-PHASE FLOWS FOR THE NPHASE CODE

M. Z. Podowski, S. P. Antal, E. A. Tselishcheva and B. Z. Wierzbicki
Center for Multiphase Research, Rensselaer Polytechnic Institute
Troy, New York 12080-3590, USA

Final Report

Prepared for the U.S. Nuclear Regulatory Commission under Contract No.
NRC-04-03-048, Task Order No. 2, "Two-Phase CFD Enhancements"; Task 2.
Development of Algorithms and Modeling Capabilities.

December, 2007

Table of Contents

	Page
1. Introduction	3
2. Multifield Modeling Concept of Two-Phase Flow	5
2.1. Generic Ensemble-Averaged Conservation Equations of Multifield Model of Interpenetrating Media	5
2.2. Effect of Interactions between Fields Representing the Same Phase	8
2.3. Governing Equations for Dispersed Two-Phase Flows	
3. Closure Laws for Gas-Liquid Two-Phase Flows	16
3.1. Overview of Existing Models of Interfacial Forces for Dispersed Gas/Liquid Two-Phase Flows	16
3.2. New Model of Turbulent-Dispersion-Induced Force	19
3.3. Interfacial Forces in Horizontal Gas/Liquid Two-Phase Flows	23
4. Two-Phase Flow Turbulence	26
4.1. $k-\epsilon$ Model of Turbulence for Single-Phase Flows	26
4.2. $k-\epsilon$ Model of Turbulence for Two-Phase Flows	26
5. Multiphase Flow Modeling in the NPHASE Code	29
5.1. Overview of NPHASE	29
5.2. Solver Description	30
5.3. Generic Form of Interfacial Forces in NPHASE	32
5.4. Two-phase Turbulence Modeling in NPHASE	37
5.5. Interfacial Area Transport Equation in NPHASE	38
6. Modeling of Moving Gas/Liquid Interfaces	40
6.1. Problem Overview	40
6.2. Large Deformable Bubbles – Experiment, Theory, Computations	42
6.3. Interface Tracking Methods	44
6.4. Level-Set Method	45
6.5. Novel Approach to Mass/Volume Conservation for Level-Set Method	48
6.6. NPHASE/Level-Set Coupling	52
6.7. Motion of Large Deformable Bubble in Contact with Solid Surface	59
6.7.1. Problem Formulation	59
6.7.2. First-Principle Approach to Model Contact Angle and triple-Line for Stationary Bubbles	61
6.7.3. External Force Concept for Numerical Control of Advancing Contact Angle of Moving Bubble	63

7. Testing and Application of NPHASE-based Multifield Model of Gas/Liquid Flows	66
7.1. Two-Phase Flow in Vertical Pipes	66
7.2. Multidimensional Analysis of Horizontal Gas/Liquid two-Phase flow	69
7.2.1. Overview of Experimental Facility and Data	70
7.2.2. Model Validation	76
7.3. Shape Evolution of Large Deformable Bubbles	102
7.3.1. Oscillating U-tube Manometer	102
7.3.2. Free Interface in Inclined and Vertical Channels	107
7.3.3. Gas Bubble at Zero Gravity	108
7.3.4. Motion of Cap Bubble in Vertical Tube	110
7.3.5. Influence of Liquid Viscosity	111
7.3.6. Effect of Surface Tension	112
7.3.7. Effect of Channel Inclination Angle on Maximum Rise Velocity	113
7.3.8. Large bubble Rising in Converging Nozzle	114
7.3.9. Large Bubble Moving along Inclined Wall	116
8. Conclusions and Recommendations for Future Work	120
References	121
Appendix: NPHASE Files	127

1. Introduction

Recent progress in both the understanding of the basic physics of two-phase flows and in the computational capabilities using CFD methods clearly show the great potential of detailed mechanistically-based numerical simulations of two-phase flows for application in reactor safety studies.

The purpose of this report is to present new multidimensional modeling concepts for two- and multiphase flows. In parallel with the physical modeling, numerical advancements in the NPHASE CMFD code have also been carried out. The proposed models have been implemented in the NPHASE code. The results of NPHASE-based model testing and validation are documented in this report.

A discussion of the multifield modeling concept of multiphase multicomponent flows is given in Chapter 2, including an overview of the generic ensemble-averaged conservation equations of multifield model of interpenetrating media, the effect of interactions between fields representing the same physical phase, and the derivation of the conservation equations for dispersed two-phase flows.

Chapter 3 is concerned with the discussion of major closure laws for gas-liquid two-phase flows, and the derivation of new mechanistic laws for dispersed gas/liquid flows and the formulation of additional laws governing horizontal flows.

Chapter 4 presents the k - ϵ model of turbulence, including both the basic formulation for single-phase flows and its modification/extension which is applicable to two- and multiphase flows.

The objective of Chapter 5 is to document the approach used in the NPHASE code to implement numerically the various models of two-phase flow and heat transfer in a manner consistent with the solver's structure and the overall computational modeling framework.

Details concerning the new model of gas/liquid interfaces are given in Chapter 6. Issues discussed in this Chapter include: (a) an overview of the state-of-the-art in the theory, experimental evidence and computational methods of interface tracking, for the motion of large deformable bubbles, (b) the formulation of the proposed approach, based on coupling the level-set method with the NPHASE solver, and (c) a new concept of modeling the motion of large bubbles in contact with solid surfaces.

The results of testing and application of the new multiphase flow models using the NPHASE code are shown in Chapter 7. Three major issues are discussed there: two-phase flow in vertical pipes, a multidimensional analysis of horizontal gas/liquid flow, and the predictions of shape and motion of large deformable bubbles in vertical and inclined conduits.

The final conclusions and recommendations for future work are given in Chapter 8.

The remaining portions of this report are the: References and Appendix. The Appendix presents the NPHASE program listing for selected two-phase flow routines, including models, Sample Input and Sample Output.

Furthermore, a recording of the complete program listing of the new models which have been implemented in the NPHASE code can be found on the CD which accompanies the report.

2. Multifield Modeling Concept of Two-Phase Flow

2.1. Generic Ensemble-Averaged Conservation Equations of Multifield Model of Interpenetrating Media

Assuming that the k -th ($k=1,2,\dots$) component of the multifluid flow can be modeled using the concept of continuum, the corresponding Eulerian conservation equations for mass, momentum and energy, respectively, become

$$\frac{\partial \rho_k}{\partial t} + \nabla \cdot (\rho_k \mathbf{v}_k) = 0 \quad (2.1)$$

$$\frac{\partial (\rho_k \mathbf{v}_k)}{\partial t} + \nabla \cdot (\rho_k \mathbf{v}_k \mathbf{v}_k) = -\nabla p_k + \nabla \cdot \underline{\underline{\tau}}_k + \rho_k \mathbf{g} \quad (2.2)$$

$$\frac{\partial (\rho_k e_k)}{\partial t} + \nabla \cdot (\rho_k \mathbf{v}_k e_k) = -\nabla \cdot [(-p_k \underline{\underline{I}} + \underline{\underline{\tau}}_k) \cdot \mathbf{v}_k] - \nabla \cdot \mathbf{q}_k'' + \rho_k \mathbf{g} \cdot \mathbf{v}_k \quad (2.3)$$

For any k , these equations are valid only at locations that pertain to fluid- k at a given time instant. At the boundaries between the fluids or phases (which may vary with time), appropriate boundary conditions must be formulated, such as those for the continuity of velocity, shear stress and heat flux. Note that if the interfaces are being modeled as sharp discontinuities in fluid density and other properties, parameters such as pressure and velocity and temperature gradients, may also experience discontinuities.

The multifield modeling concept of interpenetrating fluids is based on applying the time and space, or, in general, ensemble (statistical) averaging techniques to instantaneous conservation equations for each fluid. The resultant equations are determined with respect to a common physical and computational domain, and include terms accounting for the various interfacial effects between the individual fields.

A typical form of conservation equations for mass, momentum and energy, respectively, obtained by applying the appropriate averaging procedure to Eqs. (2.1)-(2.3), respectively, can be written as

$$\frac{\partial(\alpha_k \rho_k)}{\partial t} + \nabla \cdot (\alpha_k \rho_k \bar{\mathbf{v}}_k) = \Gamma_k \quad (2.4)$$

$$\frac{\partial(\alpha_k \rho_k \bar{\mathbf{v}}_k)}{\partial t} + \nabla \cdot (\alpha_k \rho_k \bar{\mathbf{v}}_k \bar{\mathbf{v}}_k) = -\nabla(\alpha_k \bar{p}_k) + \nabla \cdot (\alpha_k \underline{\underline{\boldsymbol{\tau}}}'_k) + \alpha_k \rho_k \mathbf{g} + \tilde{\mathbf{M}}_k^i \quad (2.5)$$

$$\frac{\partial(\alpha_k \rho_k \bar{e}_k)}{\partial t} + \nabla \cdot (\alpha_k \rho_k \bar{\mathbf{v}}_k \bar{e}_k) = -\nabla \cdot (\alpha_k \bar{\mathbf{q}}_k'') - \nabla \cdot [\alpha_k (-\bar{p}_k \mathbf{I} + \underline{\underline{\boldsymbol{\tau}}}'_k) \cdot \bar{\mathbf{v}}_k] + \alpha_k \rho_k \mathbf{g} \cdot \bar{\mathbf{v}}_k + E_k^i \quad (2.6)$$

where $\underline{\underline{\boldsymbol{\tau}}}'_k = \underline{\underline{\boldsymbol{\tau}}}_k^{\mu} + \underline{\underline{\boldsymbol{\tau}}}_k^{\text{Re}}$ is the total combined shear and turbulent shear stress, $\bar{\mathbf{q}}_k'' = \bar{\mathbf{q}}_k''^k + \bar{\mathbf{q}}_k''^{\text{Re}}$ is the total heat flux, and the corresponding interfacial source terms for fluid- k are given by

$$\Gamma_k = -\frac{1}{\Delta t} \sum_{i \in [\Delta t]} \frac{1}{|\mathbf{v}_k^i \cdot \mathbf{n}_k|} \rho_k (\mathbf{v}_k - \mathbf{v}_k^i) \cdot \mathbf{n}_k \quad (2.7)$$

$$\tilde{\mathbf{M}}_k^i = -\frac{1}{\Delta t} \sum_{i \in [\Delta t]} \frac{1}{|\mathbf{v}_k^i \cdot \mathbf{n}_k|} [\rho_k \mathbf{v}_k (\mathbf{v}_k - \mathbf{v}_k^i) + p_k \mathbf{I} - \underline{\underline{\boldsymbol{\tau}}}'_k] \cdot \mathbf{n}_k \quad (2.8)$$

$$E_k^i = -\frac{1}{\Delta t} \sum_{i \in [\Delta t]} \frac{1}{|\mathbf{v}_k^i \cdot \mathbf{n}_k|} [\rho_k e_k (\mathbf{v}_k - \mathbf{v}_k^i) + p_k \mathbf{I} - \bar{\mathbf{q}}_k''] \cdot \mathbf{n}_k \quad (2.9)$$

It is common to rewrite Eq.(2.5) and Eq.(2.6), respectively, as

$$\begin{aligned} \frac{\partial(\alpha_k \rho_k \bar{\mathbf{v}}_k)}{\partial t} + \nabla \cdot (\alpha_k \rho_k \bar{\mathbf{v}}_k \bar{\mathbf{v}}_k) &= -\alpha_k \nabla \bar{p}_k - (\bar{p}_k - p_k^i) \nabla \alpha_k + \alpha_k \nabla \cdot \underline{\underline{\boldsymbol{\tau}}}'_k \\ &+ (\underline{\underline{\boldsymbol{\tau}}}'_k - \underline{\underline{\boldsymbol{\tau}}}_k^i) \nabla \alpha_k + \mathbf{M}_k^i + \alpha_k \rho_k \mathbf{g} + \Gamma_k \mathbf{v}_k^i \end{aligned} \quad (2.10)$$

$$\begin{aligned} \frac{\partial(\alpha_k \rho_k \bar{e}_k)}{\partial t} + \nabla \cdot (\alpha_k \rho_k \bar{\mathbf{v}}_k \bar{e}_k) = -\nabla \cdot [\alpha_k (-\bar{p}_k \underline{\underline{I}} + \underline{\underline{\boldsymbol{\tau}}}_k') \cdot \bar{\mathbf{v}}_k] \\ -\alpha_k \nabla \cdot \bar{\mathbf{q}}_k'' - (\bar{\mathbf{q}}_k'' - \mathbf{q}_k'') \cdot \nabla \alpha_k + \alpha_k \rho_k \mathbf{g} \cdot \bar{\mathbf{v}}_k + \Gamma_k (e_k^i + 0.5 \bar{\mathbf{v}}_k'^2) \end{aligned} \quad (2.11)$$

where $\underline{\underline{\boldsymbol{\tau}}}_k^i$ is the average interfacial shear stress for field- k , \mathbf{M}_k^i is the interfacial force per

unit volume exerted on field- k by the other fields, $\bar{\mathbf{v}}_k^i$ is the average interfacial velocity of field- k , $\bar{\mathbf{q}}_k''$ is the average interfacial heat flux between field- k and other fields, and e_k^i is the average specific energy of field- k at the interface between this field and other fields.

The multifield modeling concept has become a very popular approach to simulate multidimensional two- and multiphase flow and heat transfer. Although the multifield conservation equations seem to be a direct extension of those governing single-phase flows, it turns out that the averaging procedure introduces several constraints on the formulation of individual models.

One of the objectives of this paper is to present selected theoretical aspects of applying the multifield modeling framework to dispersed gas/liquid flows. The emphasis is given to a consistent formulation of ensemble-averaged conservation equations, and the associated models of interfacial phenomena between the continuous and disperse fields.

The accuracy of computational predictions of gas/liquid two-phase flow and heat transfer strongly depends on the proper physical formulation of the governing interfacial phenomena. Several models of the mechanisms governing interfacial interactions have been developed to date, in particular for dispersed particle flows [Drew and Passman, 1998; Tiwari et al. 2006], but also for slug flows [Anglart and Podowski, 2002] and annular flows [Antal et al., 2001]. Whereas most theoretical/analytical models are based on mechanistic principles, they are

normally complemented by additional phenomenologically-based closure laws and/or adjustable coefficients.

New mechanistic models of gas-bubble/liquid interfacial forces are introduced in this paper. In particular, a complete turbulence-induced interfacial force is formulated, which is defined uniquely (i.e., without using arbitrary adjustable coefficients). This force is responsible for driving bubbles either away from the wall in both the central flow area and in the near wall region, although in each region, a different force component plays the dominant role. Thus, the new force combines the roles of the commonly used turbulent-dispersion force and the wall force.

2.2. Effect of Interactions between Fields Representing the Same Phase

The model given by Eqs.(2.4)-(2.6) has been derived for gas-liquid two-phase flows with well defined topology. Specifically, it applies to dispersed bubbly flows where the interfacial interactions occur across bubble/liquid interfaces that gradually evolve in time and space. However, in the case where the interfacial interactions occur within a given phase, e.g., between dispersed liquid droplets and a liquid film, or as a result of bubble coalescence or breakup, the ensemble-averaged conservation equations, Eqs.(2.4)-(2.6), must be complemented with additional terms. This, in turn, leads to the formulation of a general multifield model of multiphase flows. In this model, which is a generalization of the well-established two-fluid model, the individual fields may represent either separate fluids and phases, or geometrically/topologically distinct flow configurations within a given physical fluid or phase (e.g., continuous liquid field, dispersed small bubbles or particles, large deformed bubbles or bubble clusters, continuous gas/vapor field, and dispersed liquid field -

droplets). In such model, the interfacial source terms in Eqs.(2.4), (2.5) and (2.6), respectively, must be expanded by adding the appropriate interfacial transfer terms associated with the interfacial mass transfer from field-n into field-k, $m_{m,k}'''$, both representing the same phase. The mass, momentum and energy, respectively, conservation equations for a multifield model of gas/liquid flow can be written as:

$$\frac{\partial(\alpha_k \rho_k)}{\partial t} + \nabla \cdot (\alpha_k \rho_k \bar{\mathbf{v}}_k) = \Gamma_k + m_k''' \quad (2.12)$$

$$\begin{aligned} \frac{\partial(\alpha_k \rho_k \bar{\mathbf{v}}_k)}{\partial t} + \nabla \cdot (\alpha_k \rho_k \bar{\mathbf{v}}_k \bar{\mathbf{v}}_k) = & -\alpha_k \nabla \bar{p}_k - \sum_j (\bar{p}_k - p_{kj}^i) \nabla \alpha_k + \alpha_k \nabla \cdot \underline{\underline{\boldsymbol{\tau}}}_k' \\ & + \sum_j (\underline{\underline{\boldsymbol{\tau}}}_k^j - \underline{\underline{\boldsymbol{\tau}}}_{kj}^i) \nabla \alpha_k + \sum_j \mathbf{M}_{kj}^i + \alpha_k \rho_k \mathbf{g} + \sum_n \Gamma_{n,k} \mathbf{v}_n^i + \sum_m m_{m,k}''' \mathbf{v}_m^i \end{aligned} \quad (2.13)$$

$$\begin{aligned} \frac{\partial(\alpha_k \rho_k \bar{e}_k)}{\partial t} + \nabla \cdot (\alpha_k \rho_k \bar{\mathbf{v}}_k \bar{e}_k) = & -\nabla \cdot [\alpha_k (-\bar{p}_k \mathbf{I} + \underline{\underline{\boldsymbol{\tau}}}_k') \cdot \bar{\mathbf{v}}_k] \\ & -\alpha_k \nabla \cdot \bar{\mathbf{q}}_k'' - \sum_j (\bar{\mathbf{q}}_k'' - \mathbf{q}_{k,j}''') \cdot \nabla \alpha_k + \alpha_k \rho_k \mathbf{g} \cdot \bar{\mathbf{v}}_k + \sum_n \Gamma_{n,k} e_{n,k}^i + \sum_m m_{m,k}''' e_{m,k}^i \end{aligned} \quad (2.14)$$

where $\Gamma_k = \sum_n \Gamma_{n,k}$ and $m_k''' = \sum_m m_{m,k}'''$.

For a typical two-phase two-field model the index, k , includes: *cl* - continuous liquid phase, and *dv* - dispersed vapor phase. On the other hand, for a four-field model, the following fields can be used: continuous liquid phase (*cl*), dispersed liquid (*dl*), continuous vapor (*cv*) and dispersed vapor (*dv*).

Several additional conditions, or closure laws, are needed to close the model given by Eqs.(2.12)-(2.14). The form of individual interfacial closure laws depends on the specific physical phenomena. The range of applications (limitations) and accuracy of predictions of the multifield model strongly depend on the degree to which the closure laws, determined in

terms of ensemble-averaged state variables (i.e., component concentrations, α_k , velocities, \bar{v}_k , specific energies, \bar{e}_k and pressures, \bar{p}_k), are capable of capturing the most important (for a given situation) local mass, momentum and heat transfer phenomena. Selected issues arising from the multifield model formulation are discussed in the next section.

2.3. Governing Equations for Dispersed Two-Phase Flows

The model given by Eqs.(2.4)-(2.6) uses the Eulerian frame of reference and is based on the assumption that the individual fields can be treated as ‘equal partners’. Eqs.(2.4)-(2.6) are commonly used to model dispersed gas liquid flows. It turns out, however, that such flows do not follow the interpenetrating-media concept. It can be easily demonstrated using a two-phase model of gas/liquid flow. In particular, using the second law of dynamics for an arbitrary bubble (in general a dispersed particle) surrounded by a continuous liquid, the corresponding force balance can be written as

$$\rho_p \frac{d\mathbf{v}_p}{dt} = \rho_p V_p \mathbf{g} - \mathbf{F}_{c-p} \quad (2.15)$$

where \mathbf{F}_{c-p} is the force exerted on the bubble (or particle) by the surrounding it liquid.

Using the ensemble-averaging concept (with respect to the stationary Eulerian system of reference) to a population of dispersed particles, Eq.(2.15) yields

$$\frac{\partial(\alpha\rho_d\bar{\mathbf{v}}_d)}{\partial t} + \nabla \cdot (\alpha\rho_d\bar{\mathbf{v}}_d\bar{\mathbf{v}}_d) = p_d^i \nabla\alpha - \underline{\underline{\tau}}_d^i \cdot \nabla\alpha + \alpha\rho_d\mathbf{g} - \alpha\rho_m\mathbf{g} + \mathbf{M}_d^i + \Gamma\mathbf{v}_d^i \quad (2.16)$$

where $\rho_m = (1 - \alpha)\rho_c + \alpha\rho_d$ is the local mixture density, α is the local void fraction, and

$$\Gamma_d = -\Gamma_c = \Gamma.$$

As can be readily noticed, Eq.(2.16) does not contain either the dispersed-field pressure term, or the dispersed-field shear stress term. This is because the dispersed particles are not in contact with one another and, consequently, no forces of any kind can be transmitted directly between the particles. Thus, dispersed particles do not constitute a well-defined 'field'.

On the other hand, the momentum equation for the continuous liquid assumes the form of a complete field equation

$$\frac{\partial[(1-\alpha)\rho_c\bar{\mathbf{v}}_c]}{\partial t} + \nabla \cdot [(1-\alpha)\rho_c\bar{\mathbf{v}}_c\bar{\mathbf{v}}_c] = -(1-\alpha)\nabla p_c + (p_c - p_c^i)\nabla\alpha + (1-\alpha)\nabla \cdot \underline{\underline{\boldsymbol{\tau}}}_c - (\underline{\underline{\boldsymbol{\tau}}}_c - \underline{\underline{\boldsymbol{\tau}}}_c^i) \cdot \nabla\alpha + (1-\alpha)\rho_c\mathbf{g} + \mathbf{M}_c^i - \Gamma\mathbf{v}_c^i \quad (2.17)$$

Since the multifield model is very convenient for two-phase flow simulations and it has been implemented in several CFD codes, an important question is concerned with the use of such model for dispersed two-phase flows. A specific issue is, if and under what conditions, the pseudo-pressure and pseudo-shear stress can be defined for the dispersed component, so that Eq.(2.17) can be replaced by a complete field equation

$$\frac{\partial(\alpha\rho_d\bar{\mathbf{v}}_d)}{\partial t} + \nabla \cdot (\alpha\rho_d\bar{\mathbf{v}}_d\bar{\mathbf{v}}_d) = -\alpha\nabla p_d - (p_d - p_d^i)\nabla\alpha + \alpha\nabla \cdot \underline{\underline{\boldsymbol{\tau}}}_d + (\underline{\underline{\boldsymbol{\tau}}}_d - \underline{\underline{\boldsymbol{\tau}}}_d^i) \cdot \nabla\alpha + \alpha\rho_d\mathbf{g} + \mathbf{M}_d^i + \Gamma\mathbf{v}_d^i \quad (2.18)$$

Furthermore, the combined Eqs.(2.17) and (2.18) must yield the following Interfacial Jump Condition

$$\nabla \left[\alpha(p_d^i - p_c^i) \right] - \nabla \cdot \left[\alpha(\underline{\underline{\boldsymbol{\tau}}}_d^i - \underline{\underline{\boldsymbol{\tau}}}_c^i) \right] + \mathbf{M}_c^i + \mathbf{M}_d^i + \Gamma(\mathbf{v}_d^i - \mathbf{v}_c^i) = 0 \quad (2.19)$$

Since the only actual field pressure and shear stress are those defined for the continuous liquid, the momentum equation for this field can be written as

$$\begin{aligned} \frac{\partial[(1-\alpha)\rho_c\bar{\mathbf{v}}_c]}{\partial t} + \nabla \cdot [(1-\alpha)\rho_c\bar{\mathbf{v}}_c\bar{\mathbf{v}}_c] = & -(1-\alpha)\nabla p + (p-p_c^i)\nabla\alpha + (1-\alpha)\nabla \cdot \underline{\underline{\boldsymbol{\tau}}} \\ & -(\boldsymbol{\tau} - \underline{\underline{\boldsymbol{\tau}}}_c^i) \cdot \nabla\alpha + (1-\alpha)\rho_c\mathbf{g} + \mathbf{M}_c^i - \Gamma\mathbf{v}_c^i \end{aligned} \quad (2.20)$$

It can be shown that by assigning the pressure and shear stress of the dispersed field as equal to the corresponding terms for the continuous-field, Eq.(2.18) can be rewritten as

$$\begin{aligned} \frac{\partial(\alpha\rho_d\bar{\mathbf{v}}_d)}{\partial t} + \nabla \cdot (\alpha\rho_d\bar{\mathbf{v}}_d\bar{\mathbf{v}}_d) = & -\alpha\nabla p - (p-p_d^i)\nabla\alpha + \alpha\nabla \cdot \underline{\underline{\boldsymbol{\tau}}} + (\underline{\underline{\boldsymbol{\tau}}} - \underline{\underline{\boldsymbol{\tau}}}_d^i) \cdot \nabla\alpha \\ & + \alpha\rho_d\mathbf{g} + \mathbf{M}_d^i + \Gamma\mathbf{v}_d^i \end{aligned} \quad (2.21)$$

Thus, in order to convert the dispersed two-phase flow model into the two-field modeling framework, the following conditions must be satisfied simultaneously

$$p_d = p_c = p \quad (2.22)$$

$$\underline{\underline{\boldsymbol{\tau}}}_d = \underline{\underline{\boldsymbol{\tau}}}_c = \underline{\underline{\boldsymbol{\tau}}} \quad (2.23)$$

It should be stressed, however, that since the actual dispersed-field pressure (e.g., the pressure inside the bubbles) is not a state variable in the multifield model and, furthermore, there is no shear stress between dispersed “particles”, the definitions given by Eqs.(2.22) and (2.23) refer to the artificial, continuous-field induced, dispersed-field parameters. At the same time, both the interfacial pressure and interfacial shear stress for the dispersed field refer to the actual physical quantities. For example, in the case of bubbly flow with a continuous distribution of shear stress across bubble/liquid interface, we write

$$p_d^i - p_c^i = \sigma K \quad (2.24)$$

$$\underline{\underline{\boldsymbol{\tau}}}_d^i = \underline{\underline{\boldsymbol{\tau}}}_c^i \quad (2.25)$$

where separate closure models are required for the continuous-field interfacial pressure, p_c^i , and interfacial shear stress, $\underline{\tau}_c^i$.

To illustrate the potential implications of using an inconsistent formulation of the multifield model for dispersed two-phase flows, let us consider a one-dimensional model of fully-developed gas/liquid flow. In such case, combining the axial components of the momentum conservation equations, Eq.(2.20) and Eq.(2.21), yields

$$\left[-(\rho_c - \rho_d) g_x + (F_c^s - F_d^s) \right] \alpha (1 - \alpha) = F_{d-c}^D \quad (2.26)$$

where the liquid and gas wall shear terms satisfy

$$F_c^s = F_d^s = \frac{f^*}{2D} \rho_c u_c^2 \quad (2.27)$$

and f^* is the equivalent two-phase flow friction factor.

Since for flows in horizontal tubes and pipes, drag force is practically the only interfacial force, at equilibrium conditions we have

$$F_{d-c}^D \approx 0 \quad (2.28)$$

On the other hand, ignoring the continuous-field-induced wall shear in Eq.(2.21) (this commonly made assumption is based on the observation that for most gas/liquid flows, bubbles do not touch the wall so that the actual wall shear for the dispersed vapor component is zero), leads to

$$\Phi_{co}^2 \frac{f_{co}}{D} \frac{G^2}{2\rho_c} (1 - \alpha) = \frac{1}{8} C_D \rho_c u_r^2 A''' \quad (2.29)$$

Assuming a very small particle size, the particle-to-continuous field relative motion can be approximated by the Stokes drag model. Specifically, Eq. (2.29) yields for spherical particles of low volumetric concentrations

$$\frac{u_r}{u_{co}} = \frac{16}{9} \Phi_{co}^2 (1 - \alpha) \left(\frac{d_p}{D} \right)^2 \approx 2 \left(\frac{d_p}{D} \right)^2 \quad (2.30)$$

Let us consider a particulate flow in a microchannel, $D = 0.1 \text{ mm}$ in diameter, with the particle size, $d_p = 20 \mu\text{m}$. If the continuous field is water flowing with the average velocity, $u_{co} = 2 \text{ m/s}$, the Reynolds number is, $\text{Re}_{co} = 200$, so the previously made assumptions hold. At the same time, Eq.(2.29) yields

$$u_r \approx 0.08 u_{co} = 0.16 \text{ m/s} \quad (2.31)$$

It is obvious that this result is unphysical, since the particles are driven by the continuous fluid, so the average velocity of the dispersed field cannot exceed that of the continuous field. On the other hand, using the correct condition, i.e., assuming that $F_d^s = F_c^s$, implies that at perfect equilibrium the drag force reduces to zero, so that the velocities of both fields equalize.

Interestingly, considering turbulent flow conditions for both the continuous field and the relative motion of the dispersed field, and assuming that $f_{co} = 0.02$ and $C_D = 0.4$, yields

$$\frac{u_r}{u_{co}} \approx 0.18 \left(\frac{d_p}{D} \right)^{0.5} \quad (2.32)$$

Taking $d_p = 0.2D$ yields $\frac{u_r}{u_{co}} \approx 0.08$, whereas for $d_p = 0.1D$ we obtain, $\frac{u_r}{u_{co}} \approx 0.06$. Thus, the errors for flow in large conduits are of the same order as for the micro-channel discussed before.

When a similar analysis is performed for multi- dimensional flows based on CFD methods [Tiwari et al., 2003], the effect of model formulation on local velocity distribution can be clearly observed and examined in detail.

3. Closure Laws for Gas-Liquid Two-Phase Flows

3.1. Overview of Existing Models of Interfacial Forces for Dispersed Gas/Liquid Two-Phase Flows

The overall interfacial force in dispersed gas/liquid two-phase flows, exerted by the continuous liquid field on the dispersed gas/vapor field, is typically given as a superposition of the following terms

$$\mathbf{M}_{l-v}^i = \mathbf{F}_{l-v}^D + \mathbf{F}_{l-v}^{VM} + \mathbf{F}_{l-v}^L + \mathbf{F}_{l-v}^{TD} + \mathbf{F}_{l-v}^W \quad (3.1)$$

where the major component forces are: the drag force - \mathbf{F}_{l-v}^D , the virtual mass force - \mathbf{F}_{l-v}^{VM} , the lift force - \mathbf{F}_{l-v}^L , the turbulent dispersion force - \mathbf{F}_{l-v}^{TD} and the wall force \mathbf{F}_{l-v}^W .

The most commonly used expressions for the individual force are as follows

$$\mathbf{F}_{l-v}^D = -\frac{1}{8} C_D \rho_l |\mathbf{v}_v - \mathbf{v}_l| (\mathbf{v}_v - \mathbf{v}_l) A^m \quad (3.2)$$

$$\mathbf{F}_{l-v}^{VM} = -C_{VM} \rho_l \left(\frac{D_{v_v} \bar{\mathbf{v}}_v}{Dt} - \frac{D_{v_l} \bar{\mathbf{v}}_l}{Dt} \right) \quad (3.3)$$

$$\mathbf{F}_{l-v}^L = -C_L \rho_l \alpha (\bar{\mathbf{v}}_v - \bar{\mathbf{v}}_l) \times \bar{\mathbf{v}}_l \quad (3.4)$$

$$F_{l-v}^{TD} = -C_{TD} \rho_l k \nabla \alpha \quad (3.5)$$

$$\mathbf{F}_{l-v}^W = -C_W \rho_l \alpha \frac{|\mathbf{v}_v - \mathbf{v}_l|^2}{d_b} \mathbf{n}_w \quad (3.6)$$

where d_b is the bubble (in general, dispersed 'particle') diameter, and A^m is the interfacial area density, and k is the turbulent kinetic energy.

The values and/or expressions for the individual coefficients in Eqs.(3.2)-(3.6) have been proposed to date. Concerning the drag coefficient, Ishii and Zuber [1979] proposed the following expressions

$$C_D = \begin{cases} \frac{24}{Re_{v-l}} (1 + 0.1 Re_{v-l}^{0.75}) & \text{for } 0 < \alpha \leq 0.1 \\ \frac{2}{3} d_b \sqrt{\frac{g(\rho_l - \rho_v)}{\sigma}} \left[\frac{1 + 17.67(1 - \alpha)^{1.238}}{18.67(1 - \alpha)^{1.5}} \right]^2 & \text{for } 0.1 < \alpha \leq 0.25 \\ 9.8(1 - \alpha) & \text{for } \alpha > 0.25 \end{cases} \quad (3.7)$$

where σ is the surface tension.

The virtual mass coefficient for dilute dispersed spherical particles is, $C_{VM} = 0.5$. A generalized expression for higher void fractions has been proposed by Zuber 1964) as

$$C_{VM} = 0.5(1 + 2\alpha) \quad (3.8)$$

A theoretically derived value of the lift coefficient for a single spherical bubble in potential flow [Drew and Passman, 1998] is, $C_L = 0.5$. However, for turbulent two-phase flows, this coefficient is typically between 0.03 and 0.1. Actually, for large (> 4 mm in diameter) non-spherical bubbles, this coefficient can not only reduce all the way to zero, but even change sign [Kurul and Podowski, 1988].

Typical values of the turbulence dispersion coefficient are between $C_{TD} = 0.03$ and $C_{TD} = 0.1$.

The purpose of introducing the wall force was to account for the observed sudden decrease in bubble volumetric concentration very close to channel wall. An expression proposed by [Antal et al, 1991] is

$$C_w = \max \left[0, \left(C_{w1} + C_{w2} \frac{d_b}{y_w} \right) \right] \quad (3.9)$$

where y_w is the distance from the wall, and $C_{w1} > 0$ and $C_{w2} < 0$ are adjustable coefficients.

As can be seen the wall force disappears for the distances from the wall greater than

$$y_w \geq -\frac{C_{w2}}{C_{w1}} d_b.$$

Another expression which was used for C_w before [Antal et al., 2005] is

$$C_w = \begin{cases} C \left[1 + \left(\frac{y_w}{d_b} \right)^2 \left(2 \frac{y_w}{d_b} - 3 \right) \right] & \text{for } y < d_b \\ 0 & \text{for } y \geq d_b \end{cases} \quad (3.9a)$$

where C is a constant, a typical value of which is, $C = 0.1$.

Whereas the models of interfacial forces discussed above have been successfully used to predict phase distribution in two-phase flows over a wide range of conditions (fluids, pressures, geometries), they involve several adjustable parameters which vary from case to case. This, in turn, shows that using such models, does not allow one to fully capture the physical mechanisms governing some of the important interfacial phenomena. To reduce some of the existing modeling uncertainties and to augment the mechanistic aspects of the overall local multidimensional (CMFD) modeling framework, new models have been developed for the turbulent dispersion and wall forces. These new models are discussed in detail in Section 3.2.

3.2. New Model of Turbulent-Dispersion-Induced Force

As mentioned before, the major objective of this section is to present a new mechanistic model for the turbulent dispersion and wall forces. As it will be shown later, the proposed approach captures both effects simultaneously, while still allowing one to identify the different dominant turbulence-induced component forces in each the bulk flow region and the near-wall region. Thus, the new single mechanistic model described below replaces the combined currently used partially-heuristic models of the turbulent-dispersion and wall forces.

For the sake of clarity of the presentation, let us first consider a fully-developed single-phase flow in a vertical circular tube. The radial momentum conservation equation can be written as

$$\rho_l \frac{1}{r} \frac{\partial}{\partial r} (\rho_l r \overline{v_l'^2}) = - \frac{\partial p}{\partial r} \quad (3.10)$$

where the velocity fluctuations are related to the turbulent kinetic energy by

$$k = 0.5 \left(\overline{u_l'^2} + \overline{v_l'^2} + \overline{w_l'^2} \right) \quad (3.11)$$

Assuming isotropic turbulence, yields

$$\overline{u_l'^2} = \overline{v_l'^2} = \overline{w_l'^2} = \frac{2}{3} k \quad (3.12)$$

A typical radial distribution of turbulent kinetic energy in a cylindrical tube, predicted using a three-dimensional model is shown schematically in Figure 3.1. The curve reaches a maximum (a narrow peak) at a short distance from the wall, inside the “logarithmic wall of

the wall” region and then sharply drops to zero when approaching the laminar boundary layer (not shown in Figure 3.1).

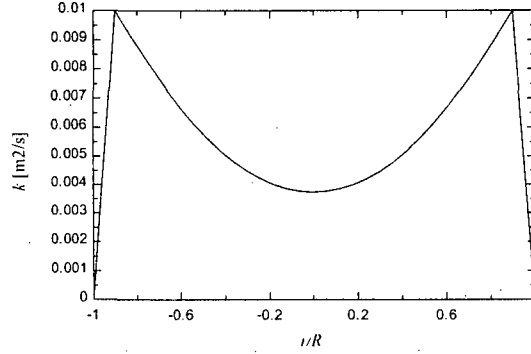


Figure 3.1. Typical radial distribution of turbulent kinetic energy in a circular tube.

Let us now consider a single small particle (or bubble) located at an arbitrary radial position inside the liquid. As can be seen, the turbulence-induced pressure gradient will result in the following force on this particle in the direction of the decreasing pressure

$$F_{p,r}^{TD} = -\frac{\partial p}{\partial r} V_p = V_p \frac{1}{r} \frac{\partial}{\partial r} (\rho_l r \overline{v_l'^2}) \quad (3.13)$$

Let us assume that the same single test-particle is injected into a dilute dispersed particulate flow. Denoting the volumetric concentration of the continuous field by, $1 - \alpha$, and since turbulence is only transmitted through this field, Eq.(3.13) becomes

$$F_{p,r}^{TD} = V_p \frac{1}{r} \frac{\partial}{\partial r} \left[(1 - \alpha) \rho_l r \overline{v_l'^2} \right] \quad (3.14)$$

Naturally, the presence of dispersed particles may affect the mean turbulent velocity fluctuation term, $\overline{v_l'^2}$.

If instead of a single particle, we consider a population of particles the concentration of which is, α , the turbulence-induced force per unit volume of the mixture becomes

$$F_r^{TD} = \alpha \frac{1}{r} \frac{\partial}{\partial r} \left[(1 - \alpha) \rho_l r \overline{v_l'^2} \right] \quad (3.15)$$

A general, three-dimensional form of Eq.(3.15) can be written as

$$\mathbf{F}_{l-v}^{TD} \approx C_{TD} \rho_l \alpha \nabla \cdot [(1 - \alpha) k] \quad (3.16)$$

where, assuming isotropic turbulence, the turbulent dispersion coefficient is, $C_{TD} = \frac{2}{3}$.

Interestingly, Eq.(3.16) can also be rewritten as

$$F_{l-v}^{TD} = -C_{TD} \rho_l \alpha k \nabla \alpha + C_{TD} \rho_l \alpha (1 - \alpha) \nabla k \quad (3.17)$$

It can be readily noticed that the first term on the RHS of Eq.(3.17) is similar to the partially-heuristic turbulent dispersion force model used before, except of the presence of the void fraction factor (α) and the fact that the coefficient, C_{TD} , is no longer an arbitrary constant, but it becomes a well-defined parameter directly related to the turbulence model. As illustrated in Figure 3.1, the first term is dominant everywhere across the flow, except for the near-wall region. In the latter region, the magnitude of the second term is much higher. Thus, the second term plays in fact the role of the wall force, and it typically prevents the bubbles in dilute dispersed flows from touching the wall.

It is also interesting to notice that the effect of turbulence in two-phase gas/liquid flows becomes noticeable for flow conditions well within the laminar range of the Reynolds numbers for the corresponding single-phase liquid [Valukina et al., 1979].

In fully-developed (adiabatic) two-phase flows, the virtual mass force becomes zero and Eq.(3.1) reduced to

$$\mathbf{M}_{l-v}^i = \mathbf{F}_{l-v}^D + \mathbf{F}_{l-v}^L + \mathbf{F}_{l-v}^{TD} \quad (3.18)$$

where the turbulent dispersion force, given by Eq. (3.16), accounts for the combined effects of turbulence in the bulk and near-wall regions.

For fully-developed flows in vertical circular tubes, the radial momentum balance typically reduces to

$$F_{l-v,r}^{TD} + F_{l-v,r}^L = 0 \quad (3.14)$$

or

$$C_{TD} \frac{1}{r} \frac{\partial}{\partial r} [(1-\alpha)\rho_l r k] - C_L \rho_l u_r \frac{\partial u_l}{\partial r} = 0 \quad (3.15)$$

where the relative velocity, $u_r = u_d - u_c$, can be evaluated from the balance of axial forces (gravity, buoyancy and drag) as

$$0.125 C_D \rho_l |u_r| u_r A'' = \alpha(1-\alpha)(\rho_l - \rho_l)g \quad (3.16)$$

For small spherical bubbles (or particles), $A'' = \frac{6\alpha}{d_b}$, and Eq.(3.16) becomes

$$0.75 C_D |u_r| u_r = (1-\alpha) \left(1 - \frac{\rho_v}{\rho_l}\right) g d_b \quad (3.17)$$

Combining Eq.(3.15) and Eq.(3.17) with the axial momentum equation of the continuous field, and with the appropriate turbulence model, the radial void fraction profile in fully-developed adiabatic dispersed gas/liquid two-phase flow can be uniquely determined. Results of calculations showing a comparison between the predicted and measured void distributions are shown in Chapter 7.

3.3. Interfacial Forces in Horizontal Gas/Liquid Two-Phase Flows

Let us consider gas liquid two-phase flow in a horizontal conduit. Since for a wide range of flow conditions, slug flows are the most common flow regimes, let us consider a simplified flow pattern schematic shown in Figure 3.2

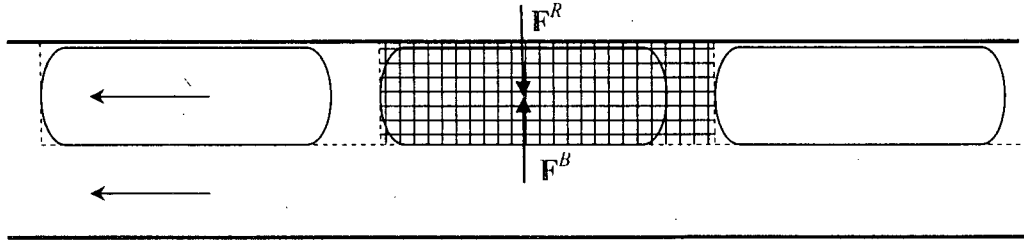


Figure 3.2. A simplified schematic of slug flow in a horizontal conduit.

As shown in Figure 3.2, the train of elongated (Taylor) bubbles can be divided into individual cells. Denoting the bubble-average volumetric gas concentration in each cell by α_b , the force balance on single bubble per unit volume of each cell can be written as

$$\sum_j \mathbf{F}_b^j = \mathbf{F}^R + \mathbf{F}_b^B + \rho_v \mathbf{g} \alpha_b \quad (3.18)$$

where \mathbf{F}_b^B is the buoyancy force given by

$$\mathbf{F}_b^B = -[(1 - \alpha_b)\rho_l + \rho_v \alpha_b] \alpha_b \mathbf{g} \quad (3.19)$$

and \mathbf{F}^R is the reaction force due to the presence of the solid walls of the conduit (if bubbles are not in direct contact with the walls, this force will be transmitted across a thin liquid film between the bubbles and the wall).

Ignoring the effect any lateral motion of the liquid with respect to the bubble and assuming ideal equilibrium (fully-developed) flow conditions, Eq.(3.18) yields

$$\mathbf{F}^R = -\alpha_b(1 - \alpha_b)(\rho_l - \rho_v)\mathbf{g} \quad (3.20)$$

Let us now revisit the local multidimensional momentum equations, Eq.(2.20) and Eq.(2.21). Since the reaction force is transmitted across the entire bubble, its effect can be uniformly distributed over the entire two-phase region. Thus, the total interfacial force becomes

$$\mathbf{M}'_{l-v} = \mathbf{F}_{l-v}^D + \mathbf{F}_{l-v}^{VM} + \mathbf{F}_{l-v}^L + \mathbf{F}_{l-v}^{TD} + \mathbf{F}_{l-v}^R \quad (3.21)$$

where \mathbf{F}_{l-v}^{TD} is given by Eq.(3.16) and \mathbf{F}_{l-v}^R is given by Eq.(3.20).

At fully-developed flow conditions in a horizontal conduit, the relative gas-to-liquid relative velocity becomes very small, and so does the lift force. Consequently, so the force balance equation in the vertical direction can be written as

$$F_{l-v,y}^{TD} + F_{l-v,y}^R \approx \alpha(1 - \alpha)(\rho_l - \rho_v)g \quad (3.22)$$

As can be seen in Figure 3.2, the reaction force is limited to the conduit section occupied by the bubbles, and becomes zero elsewhere. In order to account for this fact, as well as to express this force in terms of local rather than bubble-average void fraction, the following expression has been proposed

$$\mathbf{F}^R = C_R(\rho_l - \rho_v)\alpha(1 - \alpha)\frac{\mathbf{g}}{|\mathbf{g}|} \quad (3.23)$$

where the coefficient, C_R , is defined as

$$C_R = \begin{cases} g(1 - \varepsilon) & \text{if } y > y_c \\ 0 & \text{if } y \leq y_c \end{cases} \quad (3.24)$$

In Eq.(3.24), the parameter, y_c , depend on the size of elongated bubbles and corresponds to the vertical position of the lower boundary. The adjustable constant, ϵ , is used to assess the effect of modeling uncertainties on the accuracy of predictions in general, and the impact of nonuniform distribution of void fraction in the upper region of the conduit due to the shape variations of the elongated bubbles and the presence of small dispersed bubbles. This issue clearly deserves more work in the future.

4. Two-Phase Flow Turbulence

4.1. k - ε Model of Turbulence for Single-Phase Flows

Several momentum exchange models have been developed to date for flow-induced turbulence. One of the most commonly used and extensively validated models is the k - ε model. For single-phase flows, the k - ε model is given by two conservation equations, one for the turbulent kinetic energy, and the other for turbulent energy dissipation rate. For constant density fluids, these equations can be written as

Turbulent kinetic energy

$$\frac{\partial k}{\partial t} + \nabla \cdot (\mathbf{v}k) = \nabla \cdot \left(\frac{\mathbf{v}'}{\sigma_k} \nabla k \right) + P - \varepsilon \quad (4.1)$$

Dissipation of turbulent kinetic energy

$$\frac{\partial \varepsilon}{\partial t} + \nabla \cdot (\mathbf{v}\varepsilon) = \nabla \cdot \left(\frac{\mathbf{v}'}{\sigma_\varepsilon} \nabla \varepsilon \right) + C_1 \frac{P\varepsilon}{k} - C_2 \frac{\varepsilon^2}{k} \quad (4.2)$$

where $\sigma_k = 1.0$, $\sigma_\varepsilon = 1.3$, $C_1 = 1.44$, $C_2 = 1.92$, and P is defined as,

$$P = \mu_{eff} \nabla U (\nabla U + \nabla U^T).$$

The turbulent kinematic viscosity, \mathbf{v}' , is given by

$$\mathbf{v}' = C_\mu \frac{k^2}{\varepsilon} \quad (4.3)$$

4.2. k - ε Model of Turbulence for Two-Phase Flows

The k - ε model can be extended to two-phase flows by assuming that the total Reynolds stress for the continuous liquid is given by

$$\underline{\underline{\tau}}_c^{\text{Re}} = \underline{\underline{\tau}}_{SI}^{\text{Re}} + \underline{\underline{\tau}}_{BI}^{\text{Re}} \quad (4.4)$$

where $\underline{\underline{\tau}}_{SI}^{\text{Re}}$ is the shear-induced Reynolds stress and $\underline{\underline{\tau}}_{BI}^{\text{Re}}$ is the bubble-induced Reynolds stress.

Eq.(4.4) yields the following expression for the total combined molecular and turbulence-induced viscosity of the continuous field

$$\underline{\underline{v}}_c^{\text{tot}} = \underline{\underline{v}}_c^m + \underline{\underline{v}}_c^{\text{SI}} + \underline{\underline{v}}_c^{\text{BI}} \quad (4.5)$$

where $\underline{\underline{v}}_c^m$ is the molecular kinematic viscosity of the continuous field, $\underline{\underline{v}}_c^{\text{SI}}$ is the shear-induced kinematic turbulent viscosity, and $\underline{\underline{v}}_c^{\text{BI}}$ is the bubble-induced kinematic viscosity.

The shear-induced kinematic viscosity is modeled with a modified turbulence model as

$$\underline{\underline{v}}_c^{\text{SI}} = C_\mu \frac{k_c^2}{\varepsilon_c} \quad (4.6)$$

where the turbulent kinetic energy, k_c , and turbulent energy dissipation, ε_c , of the continuous field are given by the modified k - ε model:

Turbulent kinetic energy of continuous field

$$\left[\frac{\partial(\alpha_c k_c)}{\partial t} + \nabla \cdot (\alpha_c \underline{\underline{v}}_c k_c) \right] = \nabla \cdot \left(\alpha_c \frac{\underline{\underline{v}}_c'}{\sigma_k} \nabla k_c \right) + \alpha_c (P - \varepsilon_c) \quad (4.7)$$

Dissipation of turbulent kinetic energy of continuous field

$$\left[\frac{\partial(\alpha_c \varepsilon_c)}{\partial t} + \nabla \cdot (\alpha_c \underline{\underline{v}}_c \varepsilon_c) \right] = \nabla \cdot \left(\alpha_c \frac{\underline{\underline{v}}_c'}{\sigma_\varepsilon} \nabla \varepsilon_c \right) + \alpha_c \left(C_1 \frac{P \varepsilon_c}{k} - C_2 \frac{\varepsilon_c^2}{k_c} \right) \quad (4.8)$$

where α_c is the volumetric concentration of the continuous field.

The bubble-induced dynamic viscosity is modeled using the following expression [Sato & Sekoguchi, 1975].

$$\nu_c^{BI} = 0.5C_{\mu b}d_b\alpha_d|\mathbf{v}_d - \mathbf{v}_c| \quad (4.9)$$

where $C_{\mu b} = 1.2$.

5. Multiphase Flow Modeling in the NPHASE Code

5.1. Overview of NPHASE

The NPHASE code [Antal et al, 2000; Tiwari et al, 2003] is currently under development to better model multiphase physics and improve numerical robustness of a computational multiphase fluid dynamics (CMFD) flow solver. The NPHASE program is a segregated, nominally pressure based code. Individual transport equations are solved for momentum, energy and turbulence quantities for each field. Mixture and field continuity equations are solved in an uncoupled fashion, using frozen coefficient linearizations. The code is fully unstructured and can utilize second-order accurate convection and diffusion discretization.

A key feature of NPHASE is that from the outset the software design has focused on the development of a reliable solver for multiphase flows. Also, the various interactions between the individual fields have been incorporated as an inherent part of the solution algorithm. Thus, the user has available various mathematical formulations of the interfacial models. The user can supply information for the problem with both an input file (i.e., "nphase.dat" file) and/or may choose to add models via user routines. The user also has access to all the variables and geometric data stored within the code. That is, no data or variables are hidden from the user.

A unique aspect of the code is the initial focus for the development of NPHASE was to improve the robustness and convergence characteristics of a CMFD flow solver. As the development of the NPHASE code continued, an additional aim of the code was to implement flow regime specific mechanistic models for arbitrary geometries. That is, the mechanistic models use only local flow field information and no global parameters (e.g., hydraulic diameter). With only local information, a grid can be used to model pipes and

elbows to other more complex components (i.e., reactor fuel bundles). The implementation of flow regime specific models is considered the next important step toward a more accurate numerical prediction. The flow regimes considered important for reactor safety analysis are the bubbly, churn-turbulent, slug and annular flow regimes. The final step in development of a full range CFMD model will be the implementation of flow regime transition. This can be accomplished in the two-fluid framework with the use of separate fields for each phase. For example, the gas phase can be divided into a field for bubbly flow, a separate field for churn-turbulent (i.e., large bubbles) and even a third field for continuous vapor in the annular flow regime. The key to flow regime transition will be the ability to define the rate of mass transfer from one field to another field. Future work can develop and implement these types of mass transfer models. During this reporting period solver work continues to improve the numerical robustness and convergence characteristics for mechanistic models to simulate the bubbly, churn-turbulent and slug flow regimes.

5.2. Solver Description

The technology used by the NPHASE code is an ensemble averaged multifield model of two-phase flows [Antal et al., 2000]. In this technology, separate equations for the conservation of mass, momentum and energy for each fluid/field are developed as the framework. The governing equations are then ensemble averaged which allows the NPHASE code to predict a time-average hydraulic performance rather than time accurately track thousands or millions of bubbles in typical two phase flows.

However, in the averaging process the local interactions between the phases must be modeled by the analyst and introduced via interfacial force closure models. In NPHASE, the

interfacial forces are divided into drag and non-drag models. A key to making this technology work (i.e., validate the code at test conditions and scale the results to prototypical cases) is to include the important interfacial forces with models using appropriate functional forms. A significant amount of multifield models have been developed at RPI over the last twenty years and will allow us to predict the hydraulic performance in bubbly, churn-turbulent, slug and annular flow conditions.

Key features of NPHASE code include the following:

- Use of unstructured grids with arbitrary element types
- Capability to model an arbitrary number of fields (fluid components and/or phases)
- Built-in mechanistic modeling, integrated with numerics
- Improved robustness and numerical convergence
- Free surface modeling

The use of unstructured meshes has several advantages over multiblock structured approaches, including: rapid grid generation, ability to generate quality meshes for complex geometries, economy of elements and more forthcoming adaptive refinement. Furthermore, hybrid unstructured topologies allow prism or hexahedron elements to be used near solid boundaries for high quality meshes in boundary layer regions, while accommodating transition to pyramids and tetrahedra in the core flow. For reactor safety applications, the ability to accurately model the internal complex geometries is essential to qualify and apply CFD methods. An unstructured mesh generator is also needed as part of the analysis method.

Front-end software provides interfacing with multiblock structured meshes and, more generally, with unstructured meshes through the FIELDVIEW [1999] unstructured data format. Grid generators that have been used to date in NPHASE simulations have included

Gridpro [1998] for multiblock structured grids and Gridgen [1999] to build hybrid meshes and specify boundary conditions.

5.3. Generic Form of Interfacial Forces in NPHASE

To develop and validate a mechanistically based CFD code for problems of interest to the NRC will involve a three-step approach. A schematic diagram of the steps is shown in Figure 5.1. With the present level of model development, the majority of the effort will focus on demonstrating the ability of NPHASE to predict fundamental data. The fundamental data comparisons will include local volume fraction, phasic velocities and temperature profiles. A strong suite of basic phenomena is needed to demonstrate the ability of NPHASE to model flows of interest to the NRC.

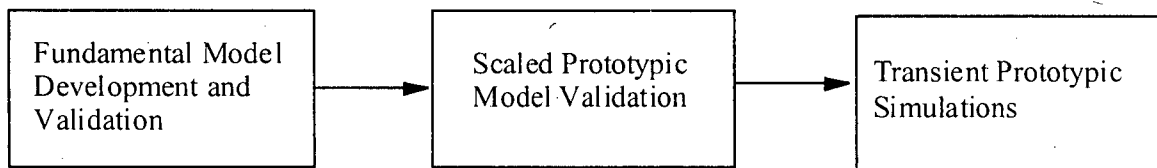


Figure 5.1. Schematic of the approach to NPHASE development.

The level of technology for mechanistic model development of two-phase flows varies greatly for different flow regimes and geometries. For example, the first flow regime that the ensemble-averaged two-phase model was applied to is the bubble flow regime. Therefore, this flow regime is more validated and qualified than the other flow regimes. Table 5.1 presents the authors' view of model development for the flow regimes of interest to the NRC. The legend of the table uses a simple scale of, H for highly developed models, M for moderately developed models, and L for limited development of models. As seen in the

table, the idealized bubble flow regime is the most highly developed for mechanistic models. In fact, this is the only flow regime where first principle predictions can be made that do not require any experimental data. Other flow regimes use mechanistic models but typically require experimental data to evaluate model coefficients or other parameters.

Table 5.1 Status of Model Development

H : Highly Developed
M : Moderately Developed
L : Limited Development

		Flow Regime			
		Bubbly flow	Churn-turbulent flow	Slug Flow	Annular Flow
Model	Drag Force	H	M	M	M
	Lift Force	H	M	M	M
	Wall Force	H	M	M	L
	Turbulence Dispersion Force	H	M	M	M
	Virtual Mass Force	H	L	L	L

The accuracy and reliability of CFD predictions strongly depend on the quality of closure models for local two-phase flow mass, momentum and energy transfer phenomena. Typically, commercial CFD codes use simplified closure laws, actually applicable only to dispersed bubbly/ particle flows, where the interfacial interactions are limited to the drag and, possibly, virtual mass forces. In addition, limited internal access to commercial codes by the user makes it difficult to take a full advantage of the new models and installing new mechanistic models in a robust manner can be very difficult. It is anticipated that this issue will be readily resolved by using the NPHASE code, where such models can be fully coupled

with the numerical solver. In fact, we propose that several generic closure laws (defined by specific mathematical operators and formulae) be implemented into the solution algorithm of NPHASE, thus allowing future additions to, and updates in, the closure laws for the bubbly, slug and annular flow regimes, as well as extensions of the range of the modeled flow regimes. Examples of the generic mechanistic models identified to date are shown in Tables 5.2, 5.3 and 5.4. Table 5.2 presents the generic momentum mechanistic models, Table 5.3 shows a typical form of the generic mass transfer mechanistic models, and Table 5.4 identifies the generic energy mechanistic models.

A key effort here will be to implement these generic mechanistic models with the underlying numerical treatment. A tighter coupling between the numerics and models is key to improve the robustness and convergence characteristics of an advanced multiphase CFD code. In the model development work, the main emphasis will be placed on the modeling of bubbly, slug and annular flows, and on the implementation of the resultant models in the NPHASE code. In addition to the implementation of closure laws for the three major flow regimes mentioned above, a concept of modeling flow regime transition will be developed. Since the phenomena governing flow regime transitions are very complex, no complete detailed theoretical models have been developed to date. The aim of this work will be to combine the experience acquired during the development of models for various flow regimes with the evolution of interfacial area density concept, to predict transition between the bubbly and slug flow regimes, and, subsequently, slug and annular flows, in terms of local flow

Table 5.2. Generic Interfacial Momentum Transfer Models

Interfacial Term	Generic Model <i>d</i> =dispersed field <i>c</i> =continuous field
Drag Force	$A_i''' \rho_c \underline{u}_d - \underline{u}_c (\underline{u}_d - \underline{u}_c)$
Lift Force	$\alpha_d \rho_c (\underline{u}_c - \underline{u}_d) \times (\nabla \times \underline{u}_c)$
Virtual Mass Force	$\alpha_d \rho_c \left(\frac{D_i \underline{u}_d}{Dt} - \frac{D_i \underline{u}_c}{Dt} \right)$
Wall Force	$F(y/R_d) \frac{\alpha_d \rho_c (\underline{u}_d - \underline{u}_c)^2}{R_d}$
Dispersion Force due to Gradient of Volume Fraction	$\rho_c k \nabla \alpha_d$
Dispersion Force due to Gradient of Volume Fraction	$\rho_c (\underline{u}_c - \underline{u}_d) (\underline{u}_c - \underline{u}_d) \cdot \nabla \alpha_d$
Dispersion Force due to Gradient of Volume Fraction	$\rho_c (\underline{u}_d - \underline{u}_c)^2 \nabla \alpha_d$
Dispersion Force due to Gradient of Relative Velocity	$\rho_c \alpha_d \nabla [\underline{u}_d - \underline{u}_c ^2]$
Dispersion Force due to Gradient of Relative Velocity	$\rho_c \alpha_d \nabla [(\underline{u}_c - \underline{u}_d)(\underline{u}_c - \underline{u}_d)]$

To date, several of these generic forms for the mechanistic closure models have been implemented and tested within the NPHASE code. For the momentum interfacial exchange the models are divided into drag and non-drag terms. This was done to allow the numerical method within the code to assume that the drag model has the form

$$M_d^{DRAG} = C(\underline{u}_d - \underline{u}_c) \quad (5.1)$$

Table 5.3. Generic Interfacial Mass Transfer Models

Interfacial Term	Generic Model <i>d</i> = dispersed field <i>c</i> = continuous field
Vapor (field 1) - Vapor (field2) Coalescence Rate	$\rho_v \alpha_1 \alpha_2$
Condensation Rate	$\frac{A_i''' q_i''}{h_{fg}}$
Boiling Rate	$\frac{A_i''' q_e''}{h_{fg}}$
Entrainment Rate	$f(\delta_{film}, u_c , u_d , \rho_c, \rho_d)$
Deposition Rate	$f(u_d , \rho_c, \rho_d)$

Table 5.4. Generic Interfacial Energy Transfer Models

Interfacial Term	Generic Model <i>d</i> = dispersed field <i>c</i> = continuous field
Interfacial Heat Transfer Rate	$q_i'' = H_i(T_{sat} - T_i)$
Evaporative Heat Transfer Rate	$q_e'' = \frac{\pi}{6} d_d^3 \rho_d f n'' h_{fg}$
Single Phase Heat Transfer Rate	$q_{1\phi}'' = H_{1\phi}(T_{wall} - T_c)$

Within the code, this term is treated implicitly with the point coefficient loaded with the phasic velocity contribution. The remaining phase is decoupled by a partial elimination algorithm (PEA) and the result is loaded into the phasic point coefficient. With this treatment the predicted velocity for the next iteration is closer to the final value. If an explicit treatment was used, then the predicted velocity would be based on the other phase velocity remaining unchanged. Experience has shown that this lack of coupling can lead to numerical oscillations and prevent the code from converging to a stable solution.

The non-drag models are treated in a more explicit manner. The present user input for these terms allows for any number of non-drag terms, coupling between any number of phases (or fields). This allows the user to model a two-phase flow with two or more fields. The advantage of more fields is the user can prescribe different interfacial physics to more accurately represent the flow of interest. For example, a churn-turbulent flow is modeled with at least three fields: a field for the continuous liquid phase (*l*), a separate field for the small bubbles (*sb*) and finally a field for the large bubbles (*lb*). With this model formulation, the user can prescribe a drag and non-drag model for small bubbles different from the large bubbles. This ability has been found to be the key to improving the accuracy of predictions of churn-turbulent flow test data.

5.4. Two-phase Turbulence Modeling in NPHASE

The turbulence model within the NPHASE code for multiphase flow analysis uses the so-called Reynolds stress approach. A detailed description of the model is given in Chapter 4. In particular, the total Reynolds stress for the continuous liquid is given by Eq.(4.4). The

shear induced Reynolds stress is evaluated using the $k-\varepsilon$ model, given by Eqs.(4.1), (4.2) and (4.3). The bubble-induced shear stress model is base on Eq.(4.9).

5.5. Interfacial Area Transport Equation in NPHASE

Many of the interfacial mass, momentum and energy models depend strongly on the amount of interface available for the transfer of the respective quantity. There accurate prediction of the interfacial area is needed to accurately predict two-phase flows for reactor safety applications. To more accurately predict the interfacial area available for interfacial process, a transport equation has been implemented into the NPHASE code. The interfacial area transport equation can be written as

$$\frac{\partial a_i}{\partial t} + \nabla \cdot (\mathbf{v}_i a_i) = \frac{1}{3\Psi} \left(\frac{\alpha_i}{a_i} \right) \sum S_i + \left(\frac{2a_i}{3\alpha_i} \right) \left[\frac{\partial \alpha_i}{\partial t} + \nabla \cdot (\mathbf{v}_i \alpha_i) \right] \quad (5.2)$$

where a_i is the interfacial area density, \mathbf{v}_i is the velocity for the interfacial area density and α_i is the volume fraction for the interfacial area density. The term, S_i , represents the sources and sinks which can increase or decrease the interfacial area density.

This form of the interfacial area density can not be directly used in the NPHASE code since several of the variables are not calculated, such as, the velocity and volume fraction for the interfacial area density. Therefore, a more convenient form has been derived, which uses the available information. First, the interfacial area density variable was redefined as

$$A_i = \frac{\alpha_i}{a_i \rho_d} \quad (5.3)$$

Since the interfacial velocity, \mathbf{v}_i , is not calculated in NPHASE an alternative velocity is needed. The interfacial velocity is expected to be closer to the dispersed phase velocity, it was used as the transport velocity. In order to retain accuracy, the difference between the dispersed phase velocity and the interfacial velocity is retained as a “correction” term which can be modeled, if desired. Finally, the dispersed phase continuity equation was used to simplify the interfacial area density transport equation.

$$\frac{\partial(\rho_d \alpha_d)}{\partial t} + \nabla \cdot (\rho_d \alpha_d \mathbf{v}_i) = \Gamma \quad (5.4)$$

Substituting and rearranging gives the form of the interfacial area transport equation implemented into the NPHASE code as

$$\frac{\partial(\rho_d \alpha_d A_i)}{\partial t} + \nabla \cdot (\rho_d \alpha_d \mathbf{v}_i A_i) = \frac{2}{3\Psi \rho_d A_i} \sum S_i + \frac{2}{3} A_i \Gamma + \frac{2}{3} \alpha_d A_i \frac{D_{v_d} \rho_d}{Dt} + \Delta C \quad (5.5)$$

where ΔC is the “correction” term due to choice of the dispersed velocity as the transport velocity. This correction term can be defined as

$$\Delta C = \frac{\partial[(\rho_d \alpha_d - \rho_i \alpha_i) A_i]}{\partial t} + \nabla \cdot [(\rho_d \alpha_d \mathbf{v}_d - \rho_i \alpha_i \mathbf{v}_i) A_i] - \frac{3}{2} A_i \left[\frac{\partial(\rho_d \alpha_d - \rho_i \alpha_i)}{\partial t} + \nabla \cdot (\rho_d \alpha_d \mathbf{v}_d - \rho_i \alpha_i \mathbf{v}_i) \right] + \frac{2}{3} A_i \left(\alpha_d \frac{D_{v_d} \rho_d}{Dt} - \alpha_i \frac{D_{v_i} \rho_i}{Dt} \right) \quad (5.6)$$

Although this term can be defined as above, it must be modeled using available variable within the NPHASE code. As a first approximation, the user can simply neglect this term and assume the interface velocity equals the gas velocity.

6. Modeling of Moving Gas/Liquid Interfaces

6.1. Problem Overview

The understanding of physical phenomena governing the shape of the gas/liquid interfaces is important for various multiphase flow and heat transfer applications. Specific applications to nuclear reactor thermal-hydraulics are concerned with the evolution of the shape of bubbles, including large deformable bubbles flowing with the liquid, small bubbles attached to solid surfaces during nucleation, as well as bubble/surface interactions in complex geometries, etc. Additional problems, making the overall task even more complicated, are associated with the effect of material properties that may be significantly altered by the addition of minute amounts of impurities, such as surfactants or nanoparticles. The present paper is concerned with the development of an innovative method of modeling time-dependent shape of gas/liquid interfaces. The proposed approach combines a modified level-set method with an advanced CFD code, NPHASE. The coupled numerical solver can be used to simulate the evolution of gas/liquid interfaces in two-phase flows for a variety of geometries and flow conditions.

As it was discussed in Chapter 2, multiphase flow modeling concepts can be grouped into three basic areas with respect to the type of approach that is needed for particular engineering problem. The most simplistic approach is the mixture model, where the multicomponent flow is treated as a single equivalent fluid. A more general, and by far the most popular, engineering concept is to use a multifield model where each flow identity (e.g., continuous liquid, dispersed droplets, small bubbles, large bubbles, and continuous vapor) can be defined as a separate field. The interactions between the individual fields are expressed by introducing closure relationships which should be based on first-principle

physics. In practice, there is still a lot of “model tuning” done in this area, that significantly limits those models. One way of building the constitutive relations for multifield models, beside theory and experiment, is to use the results of virtual experiments (or detailed numerical simulations). In particular, such approach proves useful for providing information on interface evolution. Increased computational power throughout recent years made direct numerical simulations (DNS) of multiphase flow possible, although to a certain extent only.

The present work is concerned with the modeling of large bubbles in confined channels for various geometrical configurations and shapes. Among several future applications of the results, their use in the development of mechanistic constitutive relations for the multifield models of distorted bubble flow regimes (such as churn-turbulent or slug flows, that occur in nuclear reactor systems) is of a primary interest.

The issues discussed in this Chapter include: a description of the novel aspects of the proposed level-set-concept based method, an overview of the NPHASE code modeling framework, and a description of the coupling method between these two elements of the overall model. Particular attention is given to the consistency and completeness of model formulation, and to the impact of the proposed numerical approach on the accuracy of predictions. The accuracy is measured in terms of both the calculated shape of the interfaces and the gas and liquid velocity fields around the interfaces and in the entire computational domain. The results of model testing and validation include: a U-tube manometer simulation, the effect of parasitic currents on the combined Level-Set/NPHASE predictions, bubbles of different sizes and varying bubble-to-pipe diameter ratios, the flow of Taylor bubbles along inclined pipes, and the effect of gas and liquid properties.

6.2. Large Deformable Bubbles - Experiment, Theory, Computations

Typical large deformable bubble configurations include long Taylor bubbles and cap bubbles, rising in vertical or inclined pipes/channels. Most theoretical considerations and analytical approximations have been concerned with vertical channels. In particular, it has been shown experimentally by Zukoski [1966] that for bubble Reynolds numbers greater than 200, the rise velocity of a large bubble in a tube no longer changes. In practice, it means that the viscosity effect is important only for highly viscous fluids. It has also been shown [Nickens & Yannitell, 1987] that for low and moderate viscosity liquids, the solution for bubble rise velocity can be still determined using the potential theory. The effect of increasing surface tension reduces bubble rise velocity [Zukoski, 1966], except for small surface tension where the velocity is nearly constant for a given tube diameter. For the Eotvos number, $Eo = \rho_l g D / \sigma > 70$, the effect of surface tension becomes insignificant [Nickens & Yannitell, 1987]. For air water systems, this value of Eotvos number corresponds to a tube diameter of about 2.25 cm. The corresponding expression for the rise velocity is, $U_s = 0.352\sqrt{gD}$, when the effect of surface tension is neglected, and $U_s = 0.346\sqrt{gD}$ if this effect is included.

A study on the effect of dimensionality and bubble geometry on the velocity of plane cap or Taylor bubbles [Collins, 1965] has shown that using two dimensional models yields qualitatively correct results in which the predictions are usually underestimated (by up to 9%) compared to the experimental measurements. Since in reality there are no two-dimensional bubbles, the experimental results [Maneri & Zuber, 1974] can only provide an approximation to the analytical models [Couet & Strumolo, 1987]. On the other hand,

numerical simulations seem to be a good tool for testing some of the theoretical results, both for vertical and inclined channels. Such tests are also convenient, since they are fast and computationally efficient.

Under certain conditions (mainly: low viscosity, low surface tension and weak wall effect) toroidal bubbles can also be observed. Interesting numerical simulations, combined with experimental data, are presented in [Chen et al., 1999], including a discussion of flow dependence on major non-dimensional parameters (such as the Reynolds and Bond numbers, density and viscosity ratios), and on the wall effect.

As compared to the vertical channel case, the bubble rise velocity in inclined channels is more influenced by fluid physical properties [Zukoski, 1966; Maneri & Zuber, 1974]. For large gas bubbles in inclined channels, an important difference is that as the Eotvos number increases, the Froude number does not approach its limiting value (as it was the case for a vertical configuration), but instead continues to increase. The effect of viscosity is similar for both inclined and vertical configurations, but special attention must be given to highly viscous liquids in the near-wall region.

Another interesting feature of a large bubble flow in an inclined channel is that the bubble rise velocity reaches a maximum for a certain inclination angle. This fact was confirmed experimentally by many researchers.

For a large class of liquids, viscosity has a minor effect on Taylor bubble shape and rise velocity. This suggests that the viscous term in the Navier-Stokes equation mainly plays a stabilizing role for a numerical algorithm. Also, for the same reason, the full slip condition on the channel wall seems to be a reasonable assumption, as confirmed by comparing the

numerical results of Rudman [1998] against the experimental data reported by Maneri & Zuber [1974].

Since for highly viscous liquids very few analytical results exist, numerical simulations have mainly been used to investigate this problem. For example, DeBisschop et al. [2002] performed two-dimensional calculations for a bubble in inclined channel. Their simulations were constrained to very low Reynolds numbers, corresponding to the Stokes approximation. Another limitation was that the model assumed that the bubble stayed away from the wall.

Among several advantages of numerical simulations, they can provide important information about transient flows, where analytical methods are highly limited and experiments have to be done with extreme caution.

6.3. Interface Tracking Methods

Several interface tracking methods based on the Eulerian frame of reference have been proposed to date [Lekhal et al., 2002], including the volume of fluid method, front tracking method, level set method, and phase field methods. Each method has its own advantages and disadvantages. In general, the difficulty in applying those methods to realistic physical situations is associated with the numerical representation of jump conditions at the interface (e.g., due to steep gradients of density at the interface region, and local effects of surface tension, both in the bulk flow as well as in the vicinity of a solid surface). Not less important is the treatment of flow topological changes (bubble breakup or merging) which is the drawback of many methods, especially when dealing with three-dimensional flows. Another requirement is associated with mass (or volume for incompressible flow) conservation.

In addition, most existing interface-tracking algorithms, including those using the level-set method, are based on the finite difference formulation of the governing equations, implemented using structured computational grids. This, in turn, significantly limits their applications to solve problems of practical importance. On the other hand, this paper is directed towards a general numerical formulation which can be used for unstructured grids and complex conduit geometries.

6.4. Level Set Method

The level set method is attractive from the perspective of implementing it into CFD codes for several reasons. The basic idea [Sussman et al., 1994] introduces a transport (advection) equation for the scalar level set function (based on the incompressible flow and no phase change assumptions)

$$\phi_t + \nabla \cdot (\underline{u}\phi) = 0 \quad (6.1)$$

The convention is that the zero level set corresponds to the interface location, and the negative and positive values are assigned to the gas and liquid regions, respectively. Also, the level-set function is designed in such way that the absolute value of its gradient is equal to one. Eq.(6.1) is coupled with the momentum and continuity equations. Next, the jump condition on the interface is introduced as a momentum source term in the form of body force [Brackbill et al., 1992]. This allows one to treat the flow as a single fluid formulation with variable (following the level set function) physical properties:

$$\rho(\phi) = \rho_l H(\phi) + [1 - H(\phi)]\rho_g \quad (6.2)$$

$$\mu(\phi) = \mu_l H(\phi) + [1 - H(\phi)]\mu_g \quad (6.3)$$

where H is a smoothed (for numerical purpose) Heaviside function

$$H(\phi) = \begin{cases} 1 & \text{if } \phi > \varepsilon \\ 0 & \text{if } \phi < -\varepsilon \\ \frac{1}{2} \left(1 + \frac{\phi}{\varepsilon} + \frac{1}{\pi} \sin \frac{\pi\phi}{\varepsilon} \right) & \text{if } |\phi| \leq \varepsilon \end{cases} \quad (6.4)$$

A very important feature of the level set method is that no additional algorithms are required to localize the interface during computations. Also, the curvature of the interface can be evaluated from

$$\kappa(\phi) = \nabla \cdot \left(\frac{\nabla\phi}{|\nabla\phi|} \right) \quad (6.5)$$

The resulting continuity and momentum equations for incompressible, adiabatic flow are:

$$\nabla \cdot \underline{u} = 0 \quad (6.6)$$

$$\underline{u}_i + \nabla \cdot (\underline{u}\underline{u}) = \underline{g} + \frac{1}{\rho(\phi)} \{-\nabla p + \nabla[\mu(\phi)(\nabla\underline{u} + \nabla\underline{u}^T)] - \sigma\kappa(\phi)\delta(\phi)\nabla\phi\} \quad (6.7)$$

where $\delta(\phi) = \frac{dH}{d\phi}$.

Eqs.(6.6) and (6.7) should be solved together with the level set advection equation, Eq.(6.1).

An important feature of the level set function concept is that it should serve as a measure of the (normal) distance to the interface. Unfortunately, this feature is gradually lost during iterative computations (although this effect is usually very small for a single time step). In other words, the transition region (2ε) across the interface gets distorted due to flow

nonuniformity. To eliminate this unwanted effect, a reinitialization procedure is normally applied. The requirement that the level set function be a signed (positive within one fluid, and negative within the other) distance function to the interface can be expressed as

$$|\nabla\phi| = 1 \quad (6.8)$$

The above equation is known as the Eikonal equation, and various approaches have been used to implement it. The approach used in the present work replaces Eq.(6.8) by a partial differential equation

$$\frac{\partial\phi}{\partial\tau} = S(\phi_o)(1 - |\nabla\phi|) \quad (6.9)$$

with the initial condition

$$\phi(\underline{x}, 0) = \phi_o \quad (6.10)$$

where S is the sign function and τ is an artificial time. As can be seen, a steady-state solution of Eq.(6.9) implies Eq.(6.8). What is also important, Eq.(6.9) does not allow, at least theoretically, the zero level to move, since $S(0) = 0$. Unfortunately, the above is not necessarily true when solving Eq.(6.9) numerically (see Section 6.5).

Eq.(6.9) can be also rewritten in the following form

$$\frac{\partial\phi}{\partial\tau} + \underline{w}\nabla\phi = S(\phi_o) \quad (6.11)$$

where

$$\underline{w} = S(\phi_o) \frac{\nabla\phi}{|\nabla\phi|} \quad (6.12)$$

As can be seen, Eq.(6.11) is a nonlinear hyperbolic-type equation with the characteristics given by w . This term represents a unit normal vector always pointing outward from the zero level ($\phi=0$). Hence, using Eq.(6.11), the level set function is always reinitialized first near the zero level. As a result, only a few iterations are needed to satisfy Eq.(6.8) in this transition region.

6.5. Novel Approach to Mass/Volume Conservation for Level Set Method

In this section, a novel approach to mass conservation for multiphase flow simulations using the level set method is described. The new concept combines the local mass conservation (within one grid cell) with the global mass conservation (in the entire flow domain), giving quite accurate results.

The advantage of the level set method is that it allows one to accurately compute the curvature of the interface and to account for topological changes (such as bubble merging or breakup). The major drawbacks of the original method are: a gradual change of the interface transition region thickness around the interface, and a violation of mass balance throughout the simulation.

Level set reinitialization is normally used as means to prevent (or mitigate) the deformation of the transition region. However, the associated numerical process normally contributes to mass imbalance. In addition, the discretization errors of the numerical solution of the combined fluid- flow/level-set-advection equations may further increase the global fluid mass imbalance. In the present model, a two-step correction procedure is used, as discussed below.

Let us first consider the approach to minimize the reinitialization-induced errors in local mass conservation [Sussman et al., 1999]]. Denoting the level set function after the k -th reinitialization iteration by d^k , the following condition should be satisfied

$$\int_{\Omega_{ij}} H(d^k) d\Omega_{ij} = \int_{\Omega_{ij}} H(d^0) d\Omega_{ij} \quad (6.13)$$

where Ω_{ij} is the cell volume and H is the smoothed Heaviside function. The fact that Eq.(6.13) assures mass conservation can be readily deduced by expressing the mass contained in a grid cell as

$$M_{ij} = \int_{\Omega_{ij}} \rho(\phi) d\Omega_{ij} = \rho_g \int_{\Omega_{ij}} d\Omega_{ij} + (\rho_l - \rho_g) \int_{\Omega_{ij}} H(\phi) d\Omega_{ij} \quad (6.14)$$

It is also important to realize that Eq.(6.13) should only be applied to those grid cells that contain the zero level. To prove it, let us consider a simple example of 1-D level set function (such as in the case of predicting the liquid level in a tank, with the zero level set corresponding to the gas/ liquid interface). This is shown in Figure 6.1. Furthermore, let us assume that the smoothed Heaviside function, and thus the fluid density, in the transition region (that is assumed to extend over three nodes) are linear functions of the level set. This assumption can be readily relaxed without losing the generality of the proof, since any anti-symmetric level set function could be considered instead. It follows from Figure 6.1 that after the reinitialization in cell-2, the mass will stay the same, since the zero level is at the same x location for both the initial and final level sets. On the contrary, the mass in cell-1 will increase and in cell-3 will decrease. This is why the correction for the reinitialization scheme, arising from the constraint given by Eq.(6.13), should be used only in the cells containing the zero level.

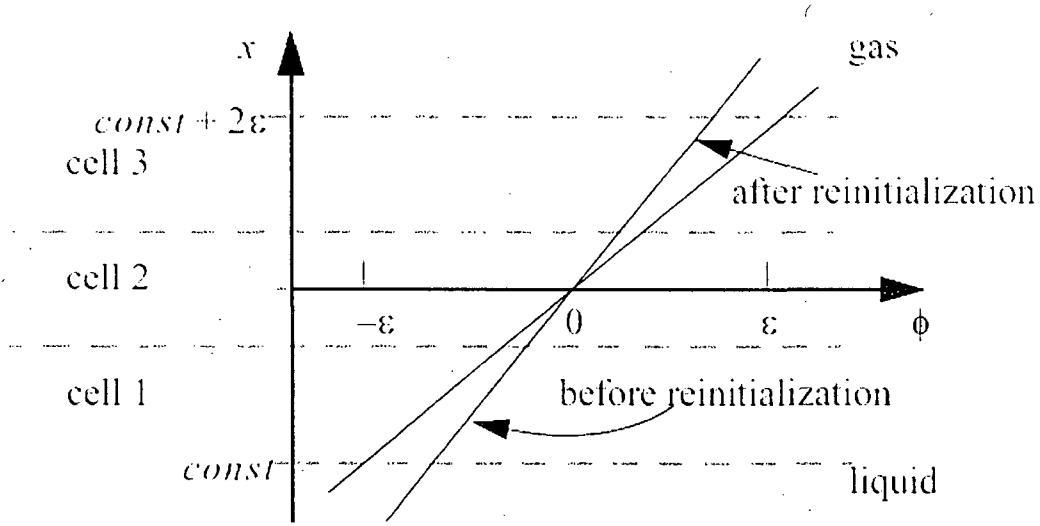


Figure 6.1. An illustration of Level Set reinitialization and mass conservation.

Let us now discuss the algorithm used to preserve local mass (volume) balance.

Rewriting Eq.(6.13) and approximating the integrand, yields

$$\begin{aligned}
 0 &= \int_{\Omega_{ij}} H(d^k) d\Omega_{ij} - \int_{\Omega_{ij}} H(d^0) d\Omega_{ij} \approx (\tau^k - \tau^0) \int_{\Omega_{ij}} \frac{dH}{d\tau}(d^0) d\Omega_{ij} \\
 &\approx \int_{\Omega_{ij}} H'(d^0)(d^k - d^0) d\Omega_{ij}
 \end{aligned} \tag{6.15}$$

where

$$H'(d) = \begin{cases} 0 & \text{if } |d| > \epsilon \\ \frac{1}{2\epsilon} \left(1 + \cos \frac{\pi d}{\epsilon} \right) & \text{if } |d| \leq \epsilon \end{cases} \tag{6.16}$$

Let \tilde{d}^k be the level set function after the k -th reinitialization iteration, but before mass correction. Thus, we write

$$d^k = \tilde{d}^k + \lambda(\tau^k - \tau^0) H'(d^0) \tag{6.17}$$

where λ is assumed to be constant in a grid cell, that can be evaluated by substituting Eq.(6.17) into (6.15)

$$\lambda = \frac{\int_{\Omega_{ij}} H'(d^0) \frac{(\tilde{d}^k - d^0)}{(\tau^k - \tau^0)} d\Omega_{ij}}{\int_{\Omega_{ij}} [H'(d^0)]^2 d\Omega_{ij}} \quad (6.18)$$

The procedure for mass correction given by Eqs.(6.17) and (6.18) has the major advantage of being local. It is performed separately in each grid cell containing the zero level, and has the strongest impact in those cells on the interface which are significantly affected by the reinitialization scheme. At the same time, this purely local nature of the method causes a new problem, since there is no coupling between the cells and, thus, it is difficult to maintain the overall mass balance. Because of that, a separate algorithm for global mass conservation is needed. A combination of the two correction methods is what should be finally used in level set simulations.

To describe the global mass conservation method, let us assume a single gas bubble rising in a liquid. Denoting the entire flow domain by Q , the total mass of fluid in the system (that should not change throughout the simulation) is

$$M = \int_{\emptyset} \rho(\phi) dQ \quad (6.19)$$

After a single time step in the numerical solution, the calculated total mass of the fluid may change due to the combined advection and reinitialization errors (the latter is usually much bigger). The idea behind the global mass conservation is to adjust the level set function by adding a correction factor to it

$$d^k = \tilde{d}^k + c^k \quad (6.20)$$

such that the updated level set function satisfies the overall mass balance. As a result, the bubble either shrinks or expands uniformly over its interface, however this correction is very small. The coefficient, c^k , is constant over the entire computational domain, so that it preserves the important property of the level set as a distance function. Specifically

$$|\nabla d^k| = |\nabla(\tilde{d}^k + c^k)| = |\nabla \tilde{d}^k| = 1 \quad (6.21)$$

The appropriate value of the constant c^k can be always found in a straightforward manner, and the additional computation is performed very fast (e.g., via simple iterations using a bisection method).

6.6. NPHASE/Level-Set Coupling

As it was already discussed in Chapter 5, NPHASE is a pressure-based finite volume CFD computer code. The initial focus for the development of NPHASE was to improve the robustness and convergence characteristics of a computational multiphase fluid dynamics (CMFD) flow solver. Whereas the NPHASE code has several unique features to handle complex multiple field simulations, the level set method utilizes a single fluid (i.e., one field) model.

For single-phase flows, the algorithm follows an established segregated pressure based methodology. The governing equations for mass and momentum are integrated over each cell (i.e., each control volume in the grid) in the domain. The primitive variables tracked are the pressure, components of velocity, enthalpy and turbulent kinetic energy and turbulence

dissipation rate. The in inviscid flux is accumulated by sweeping through internal and boundary faces as

$$\int_V \nabla \cdot (\rho \underline{u} \psi) dV = \oint_{faces} \rho \underline{u} \psi \cdot d\underline{A} = \sum_{faces} \rho \underline{u} \psi \cdot \underline{A} = \sum_{faces} C \psi \quad (6.22)$$

Since the primitive variables are co-located at the cell center, a method to control numerical pressure oscillations is needed. Artificial dissipation is added for this purpose, to damp the numerical pressure oscillations via a Rhie-Chow [1983] facial velocity interpolation or other similar methods. The discretized equations are cast using lagged coefficient linearization as

$$A_p \psi_p = \sum_{j-neighbors} A_j \psi_j + S \quad (6.23)$$

where A_p and A_j are the lagged coefficients, ψ is the primitive variable and S is a source term. Continuity is forced through a pressure correction equation, based on the SIMPLEC algorithm [VanDoormal and Rainthby, 1984]. At each iteration, the discretized momentum equations are solved approximately using a Jacobi point iterative solver. A more exact solution of the pressure correction equation is the next step in the algorithm. A preconditioned algebraic multigrid (AMG) linear solver is used to solve the pressure correction equation. Both the pressure and velocity primitive variables are then updated to conserve mass. And finally, the enthalpy and turbulence scalars are solved, if needed. The process is repeated until a converged solution is obtained. For transient flows, usually a second order backward time integration is used.

To date, the majority of work done towards the development of the level set method has been based on the finite difference discretization of the governing equations. This is

inconvenient for a potential user for two basic reasons. First, such a formulation cannot be applied to flows in complicated geometries where the use of unstructured grids is necessary. Secondly, the straightforward implementation of the method into the existing (not finite difference based) codes is practically impossible, because it requires the numerical schemes to be reformulated.

The coupling of the finite volume based NPHASE code with the level set method involves the following steps (where all equations are solved in a dimensional form):

(A) Implementation of the incompressibility requirement.

A general form of the continuity equation is used in the NPHASE code, given by

$$\frac{\partial \rho}{\partial t} + \nabla \cdot (\rho \underline{u}) = 0 \quad (6.24)$$

Eq.(6.24) can be rewritten as

$$\frac{D_u \rho}{Dt} + \rho \nabla \cdot \underline{u} = 0 \quad (6.25)$$

The incompressibility condition is

$$\frac{D_u \rho}{Dt} = \frac{\partial \rho}{\partial t} + \underline{u} \nabla \cdot \rho = 0 \quad (6.26)$$

Note that Eq.(6.26) does not imply a constant fluid density; it only requires that any density change propagates with the flow.

Substituting Eq.(6.26) into Eq.(6.25) yields

$$\nabla \cdot \underline{u} = 0 \quad (6.27)$$

which is the divergence-free velocity condition.

(B) Formulation of the momentum equation across the interfacial region.

The original momentum equation used by NPHASE code is

$$\frac{\partial}{\partial t}(\rho \underline{u}) + \nabla \cdot (\rho \underline{u} \underline{u}) = -\nabla p + \nabla[\mu(\nabla \underline{u} + \nabla \underline{u}^T)] + \rho \underline{g} + \underline{S} \quad (6.28)$$

where \underline{S} corresponds to a general (user defined) source term.

When Eq.(6.28) is used across the gas/liquid interface, the source term becomes (see Eq.(6.7))

$$\underline{S} = -\sigma \kappa(\phi) \delta(\phi) \nabla \phi \quad (6.29)$$

Combining Eq.(6.28) with the continuity equation, Eq.(6.24), yields a nonconservative form of the momentum equation

$$\rho(\underline{u}_t + \underline{u} \cdot \nabla \underline{u}) = -\nabla p + \nabla[\mu(\nabla \underline{u} + \nabla \underline{u}^T)] + \rho \underline{g} + \underline{S} \quad (6.30)$$

Dividing Eq.(6.30) by the density and using Eq.(6.27), we obtain

$$\underline{u}_t + \nabla \cdot (\underline{u} \underline{u}) = \underline{g} + \frac{1}{\rho} \{-\nabla p + \nabla[\mu(\nabla \underline{u} + \nabla \underline{u}^T)] - \sigma \kappa(\phi) \delta(\phi) \nabla \phi\} \quad (6.31)$$

Eq.(6.31) can be rewritten as

$$\underline{u}_t + \nabla \cdot (\underline{u} \underline{u}) = \underline{g} + \{-\nabla p + \nabla[\mu(\nabla \underline{u} + \nabla \underline{u}^T)] + \tilde{\underline{S}}\} \quad (6.32)$$

where the modified source term is

$$\begin{aligned} \tilde{\underline{S}} = & \left(1 - \frac{1}{\rho(\phi)}\right) \nabla p + \left\{ \frac{1}{\rho(\phi)} \nabla[\mu(\phi)(\nabla \underline{u} + \nabla \underline{u}^T)] - \nabla[v(\phi)(\nabla \underline{u} + \nabla \underline{u}^T)] \right\} \\ & - \sigma \frac{\kappa(\phi)}{\mu(\phi)} \delta(\phi) \nabla \phi \end{aligned} \quad (6.33)$$

Since both $\rho(\phi)$ and $\mu(\phi)$ are defined in Eqs.(6.2) and (6.3), respectively, as prescribed functions satisfying the continuity condition between the corresponding properties of the liquid and gas phases across the interface, the kinematic viscosity, $\nu(\phi)$, can also be defined in a similar manner in terms of the phasic viscosities and the level set function. A natural choice is, $\nu(\phi) = \frac{\mu(\phi)}{\rho(\phi)}$, although other definitions satisfying proper boundary conditions can also be used.

Since across the interfacial region, $|\phi| \leq \varepsilon$, the surface tension force plays a dominant role, it can be readily shown that the viscous effects are negligible in this region, i.e.

$$\left| \frac{1}{\rho(\phi)} \nabla[\mu(\phi)(\nabla \underline{u} + \nabla \underline{u}^T)] - \nabla[\nu(\phi)(\nabla \underline{u} + \nabla \underline{u}^T)] \right| \ll \sigma \left| \frac{\kappa(\phi)}{\mu(\phi)} \delta(\phi) \nabla \phi \right| \quad (6.34)$$

Actually, it can also be shown that, for a given velocity field across the interface, $\nu(\phi)$ can be formulated in such a way that the left hand side of Eq.(6.34) becomes equal to zero. Thus, the source term in Eq.(6.32) simplifies to

$$\underline{\tilde{S}} \approx \left(1 - \frac{1}{\rho(\phi)} \right) \nabla p - \sigma \frac{\kappa(\phi)}{\mu(\phi)} \delta(\phi) \nabla \phi \quad (6.35)$$

Eq.(6.32) is convenient for numerical purposes, since it represents a conservative form of the momentum equation (with the density equal to unity) and, thus, is consistent with the solution algorithm of the NPHASE code.

After adding the source term due to surface tension, and explicitly writing density and viscosity as functions of the level set function, as given by Eqs.(6.2) and (6.3), Eq.(6.32)

becomes Eq.(6.7) with the curvature, $\kappa(\phi)$, given by Eq.(6.5), and $\delta(\phi) = \frac{dH}{d\phi}$.

- (C) The level-set advection equation is added in the conservative form, based on the incompressibility assumption.
- (D) Reinitialization techniques are employed to preserve constant interface thickness and mass (or volume) conservation.

The numerical scheme for the level set method is based on a finite volume formulation, as shown in Figure 6.2. The discrete values for all flow variables (velocity, pressure, level set function) are evaluated at cell centers (e.g., point “C” or “E”).

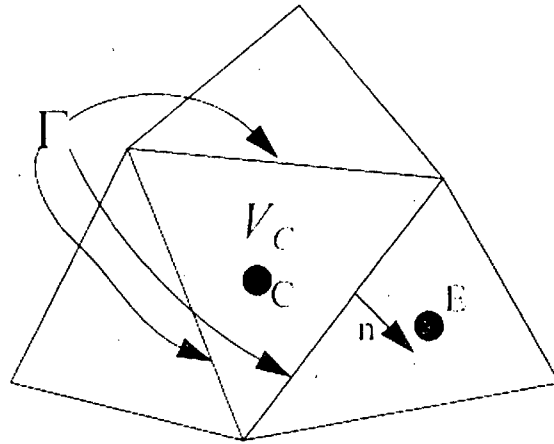


Figure 6.2. Finite Volume Method formulation for the Level Set Function

The level set function is updated each time step with a semi-explicit scheme: the velocity is taken from the current time step and the level set function from the previous one (usually, explicit schemes are used when dealing with hyperbolic partial differential equations, like the advection equation for instance). In general, a scheme approximating Eq.(6.1) in the finite volume method can be expressed (after integrating Eq.(6.1) over the cell volume) as

$$\phi_C^{n+1} = \phi_C^n - \Delta t G \tag{6.36}$$

where

$$\phi_C = \frac{1}{V_C} \int_{V_C} \phi dV_C \quad (6.37)$$

$$G = \frac{1}{V_C} \int_{V_C} \nabla \cdot (\underline{u}\phi) dV_C = \frac{1}{V_C} \int_{\Gamma} \underline{n} \cdot (\underline{u}\phi) d\Gamma \approx \frac{1}{V_C} \sum_{faces} (\underline{n} \cdot \underline{u}\phi A)_{faces} \quad (6.38)$$

One of the major difficulties in the numerical formulation is associated with evaluating the fluxes (see Eq.(6.38)) through cells boundaries (faces). A straightforward method is to use an upwind scheme to evaluate the facial flux. Also, the convergence of the entire algorithm (together with the continuity and momentum equations) must be assured.

For example, let us consider the face between nodes 'C' and 'E' in Figure 6.2. To evaluate Eq.(6.38), the velocity on this face is interpolated between the two nodal velocities (this is why the cells should not be too skewed), and the first order upwind scheme is used for the level set function

$$\phi_{face} = \begin{cases} \phi_C & \text{if } \underline{nu} > 0 \\ \phi_E & \text{if } \underline{nu} < 0 \end{cases} \quad (6.39)$$

In summary, the following algorithm is applied in the coupled level set/NPHASE method:

- (a) Initial conditions for velocity, pressure, level set function are prescribed.
- (b) Material properties (level set density, viscosity) for the momentum equation are evaluated based on the current nodal values of the level set function.
- (c) The NPHASE solver is applied to determine the values of pressure and velocity at the new time step.

- (d) Based on the initial (old, in subsequent time steps) values of the level set function and the updated (step (c)) velocity field, the level set function is updated according to Eq.(6.36).
- (e) Reinitialization of the level set function is performed.
- (f) Iterations within one time step (steps (b) to (e)) are repeated until convergence is reached.
- (g) The initial (old) values of the level set function are overwritten by the new values calculated in (d); they can also be saved for post-processing.
- (i) Steps (b) to (g) are repeated for a desired number of time steps.

6.7. Motion of Large Deformable Bubble in Contact with Solid Surfaces

6.7.1. Problem Formulation

Gas/liquid two-phase flow systems frequently encounter situations in which the gas phase flows in the form of large bubbles surrounded by the liquid phase. In the case of inclined or horizontal conduits, the bubbles may either be separated from the conduit's upper wall by a thin liquid film or they can be in direct contact with the wall. Since large bubbles are typically highly deformable, their shape and position depend on the properties of both the liquid and gas components, as well as on the flow conditions and conduit geometry. The underlying physics becomes even more complex if the bubbles touch the wall, forming a gas/liquid/solid triple line at the interface between the three materials [Vafaei and Podowski, 2005].

The present Section is concerned with the development of an innovative approach to model time-dependent shape of gas/liquid interfaces in the presence of solid walls. The

proposed approach combines a modified level-set method with the NPHASE code. The coupled numerical solver can be used to simulate the evolution of gas/liquid interfaces in two-phase flows for a variety of geometries and flow conditions. The issues discussed in this paper include: the influence of gas/liquid/solid interfacial properties on contact angle, the physical aspects of gas/liquid/solid triple line evolution, and the new modeling concept aimed at capturing the triple line motion for large bubbles flowing along (and underneath) horizontal and/or inclined surfaces, including the apparent singularity due to the no-slip condition being applied everywhere except the triple line itself. A description is given of the novel aspects of the proposed Level-Set-concept based method, and of the coupled Level-Set/NPHASE solver. In particular, details are presented of the proposed computational approach based on the concept of local artificial force used to control the advancing contact angle.

A typical situation relevant to the current model formulation is concerned with a gas bubble formed underneath (and in direct contact with) a horizontal solid surface. We assume that at a given time instant the initially-horizontal surface is quickly rotated to assume a fixed inclination angle with the horizontal direction. If the inclination angle is sufficiently large, the bubble will start sliding along the surface, while its shape will undergo a gradual transition to a new equilibrium form. The objective of this work is to predict the process described above, including the evaluation of the bubble shape and velocity evolutions from the start to the final equilibrium flow condition.

6.7.2. First-Principle Approach to Model Contact Angle and Triple Line for Stationary Bubbles

A schematic of stationary bubble formed underneath a flat horizontal surface is shown in Figure 6.3.

As long as the bubble remains stationary, its shape depends on the physical properties of both the gas and the surrounding it liquid, as well as on the liquid/gas/solid interfacial properties (interfacial tensions, wettability, etc.).

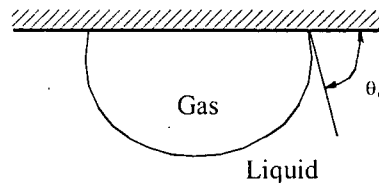


Figure 6.3. Typical geometry of a stationary gas bubble underneath a smooth flat horizontal surface.

Because of its importance for various practical applications and industrial processes, in particular - boiling and condensation, the physics of confined liquid (droplets) or gas (bubbles) volumes has been the subject of extensive investigations. A very important issue is concerned with the geometry of gas/liquid/solid triple line in general, and the contact angle in particular. Typically, the macroscopic contact angle for stationary gas-bubbles/liquid-droplets is either assumed as a fixed value based on experiments, or (for static situations) determined from the Young equation

$$\sigma_{lg} \cos \theta_o = \sigma_{sg} - \sigma_{sl} \quad (6.40)$$

where σ_{lg} , σ_{sg} and σ_{sl} , respectively, are the liquid/gas, solid/gas, and solid-liquid surface tensions. Unfortunately, treating the surface tension terms as physical constants implies that

the contact angle of a droplet or a bubble is size independent, which contradicts the existing experimental evidence.

It turns out that the size-dependent contact angle between the liquid/gas interface and solid walls at static (motionless) conditions can be evaluated from a consistent first-principle model that has been recently proposed by Vafaei & Podowski [2005]. Specifically, realizing that the gas/liquid surface tension force and the gravity force are independent of each other, and the effect of the latter diminishes with decreasing droplet size, comparing the normal interfacial forces on an axisymmetric droplet or bubble of any given size, one at full gravity, the other at zero gravity, the following expression can be derived

$$r_d \sin \theta_o = r_{d,s} \sin \theta_s \quad (6.41)$$

where $r_{d,s}$ and r_d , respectively, are the radii of the contact line for the spherical (at $g = 0$) and actual (at full g) droplet or bubble, and θ_s and θ_o are the corresponding contact angles.

Since for smooth surfaces, θ_s is uniquely determined by the gas/liquid/solid material properties, combining Eq.(6.40) with the Laplace-Young equation

$$K(z) = K_o + \frac{\rho g}{\sigma_{lg}} z \quad (6.42)$$

where z is the distance from droplet apex, $K(z)$ is the local curvature, and K_o is the curvature at the apex, allows one to determine the geometry of arbitrary-shape bubbles (or droplets) for given material properties and bubble/ droplet volume, for both axisymmetric (on horizontal surfaces) and arbitrary shapes (on inclined surfaces).

A typical comparison between the theoretically predicted and measured contact angle is shown in Figure 6.4.

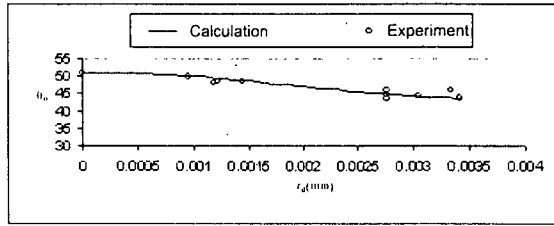


Figure 6.4. Comparison between the predicted and measured contact angle [Vafaei and Podowski, 2005].

Because in the case of moving bubbles in inclined conduits, the geometry of the triple line is governed by the combined effects of gravity, shear and capillary forces, the method used for static configurations must be combined with the fluid flow analysis on both sides of the gas/liquid interface. The present approach to the evaluation of flow field both inside and outside the bubbles is based on combining a modified level-set method with the finite volume solver, both implemented in the NPHASE code.

6.7.3 External Force Concept for Numerical Control of Advancing Contact Angle of Moving Bubble

Let us consider a rigid section of that gas/liquid interface, inclined at a given angle to the wall, shown in Figure 6.5. We assume that the rigid interface moves with a velocity, u_{rb} , against the flow.

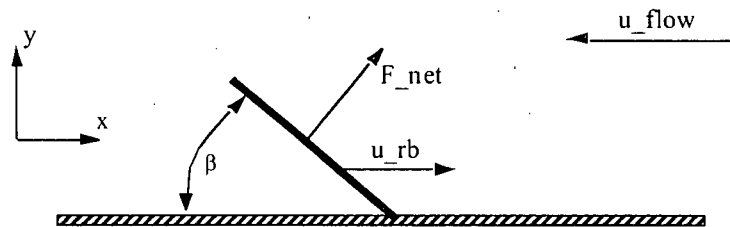


Figure 6.5. Force applied near the wall and perpendicular to the rigid section of gas/liquid interface.

The kinematic condition that the flow must be parallel to the interface is replaced by applying the local force (a Dirac-Delta-type function) in the near wall rigid interface region. The position of the rigid section is tracked by the level set function. Obviously, the force is added into the momentum equation. In general, we don't know the magnitude of this force a priori. Our task is to calculate this force, having given the rigid section's inclination angle and external flow conditions.

The external force is evaluated iteratively until the convergence criteria for the equations of motion are met. The force has the following form

$$\vec{F}_{net} = \sum_{i=1}^N \vec{F}_{cell-i} \quad (6.43)$$

where \vec{F}_{cell-i} is the force applied on cell-i in the direction normal to the interface, and N is the total number of cells on both sides of the interface.

Each component force is calculated iteratively as

$$\vec{F}_{cell-i} = \sum_k \vec{F}_{cell-i}^k \quad (6.44)$$

where \vec{F}_{cell-i}^k are the force increments corresponding to the individual iterations being a part of the convergence process of the NPHASE-code-based calculations.

The calculations continue until the convergence criteria for the equations of motion are met. Specifically, at each NPHASE iteration the force increments are defined as follows:

$$F_{cell-i,x}^k = -C_i^k (u_i^k - u_{rb} - v_i^k \cot \beta) \sin \beta \quad (6.45)$$

$$F_{cell-i,x}^k = C_i^k (u_i^k - u_{rb} - v_i^k \cot \beta) \cos \beta \quad (6.46)$$

where u_i^k is the fluid velocity along the solid surface in cell-i, v_i^k is the corresponding velocity in the direction normal to the surface, β is the prescribed (calculated separately) contact angle, and C_i^k is a proportionality coefficient.

A fundamental feature of this force is that it is perpendicular to the prescribed orientation of the interface (defined via the contact angle). This is because each force increment is perpendicular, regardless of its magnitude. During the iterations, expressions in the parenthesis in Eqs.(6.45) and (6.46) converge to zero. Hence, the force increments eventually become very small and the total force reaches a steady value. It is important to mention that the current formulation of the external force assures stability of the overall solution.

7. Testing and Application of NPHASE-based Multifield Model of Gas/Liquid Flows

7.1. Two-Phase Flow in Vertical Pipes

The new model of interfacial forces (in particular, the generalized turbulent-dispersion force) introduced in Chapter 3 has been used to predict the radial void distributions for two cases.

First, the experimental conditions of Wang et al. [1987] were used as a reference, corresponding to the superficial velocities of the liquid and gas phases, 0.71 m/s and 0.1 m/s, respectively. Since the objective of the present analysis was to test the interfacial force balance and its effect of the void profile, the liquid velocity distribution and average turbulent velocity fluctuations were taken directly from the experimental data. Figure 7.1 presents the measured radial velocity profile (dots) and the corresponding continuous curve fit. Since details of neither the near-wall velocity distribution nor turbulence can normally be accurately measured, a simplified distribution (a standard approximation used in numerical CFD simulations) was used in this region.

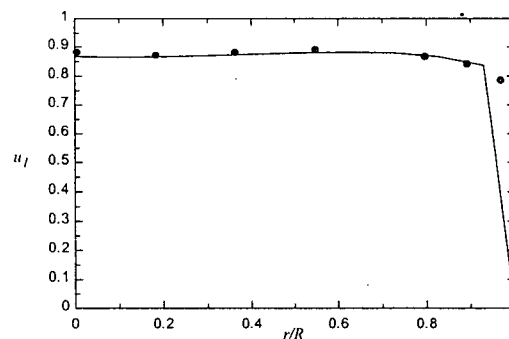


Figure 7.1. The radial liquid velocity profile measured by Wang et al. [1987], used in the validation of the present model of interfacial forces.

The radial void distribution was evaluated based on the combined Eq.(29) and Eq.(31). As can be seen, the only adjustable parameter in the model is the lift coefficient. The theoretical value derived for a single bubble in potential flow [Drew and Passman, 1998] is $C_L = 0.5$. However, for turbulent two-phase flows, this coefficient is typically between 0.03 and 0.1. Actually for large (> 4 mm in diameter) non-spherical bubbles, this coefficient can not only get reduced all the way to zero, but even change sign [Kurul and Podowski, 1988]. It is important to notice that the results of predictions using the present model actually depend on the ratio, C_L/C_{TD} , where the turbulent dispersion coefficient for isotropic turbulence is, $C_{TD} = 2/3$, and it may assume slightly lower values if the axial velocity fluctuations exceed those in the lateral directions (but will typically be higher than, $C_{TD} = 0.5$).

Another parameter affecting the results of predictions is the bubble diameter. In order to test its effect, different values have been used, between 1 mm and 2 mm.

The results obtained for isotropic turbulence and for $C_L = 0.04$ are shown in Figure 3. The dots represent the experimental data and the three curves correspond to different C_L/C_{TD} ratios and different bubble diameters.

The base case (solid line in Figure 3) refers to $C_{TD} = 2/3$, $C_L = 0.04$, and $d_b = 1$ mm. As can be seen, the predictions are in a good agreement with the experimental data. The differences noticed for different assumed values of C_L/C_{TD} and d_b confirm the importance of improving our understanding of (and the ability to model) the physical phenomena governing turbulence, lift force and average bubble diameter (or diameter distribution).

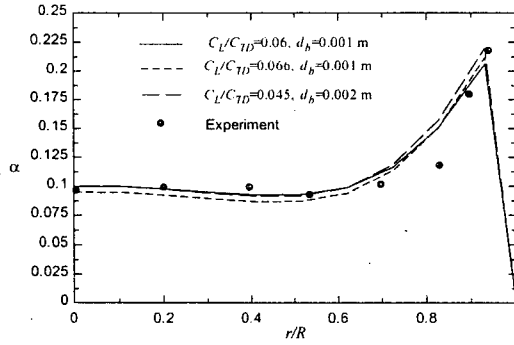


Figure 7.2. A comparison between the predicted and measured void fraction in gas/liquid two-phase flow [Wang et al. 1987].

The same model as used in the previous comparison was applied to predict the experimental data of Serizawa et al. [1975]. The results are shown in Figure 7.3. The base-case calculations were performed using exactly the same coefficients as before. In addition, the sensitivity of predictions to the variations of these parameters was tested. Again, a good agreement was obtained between the predictions and the data, although both the flow conditions and gas fraction were considerably different from those used in the previous case.

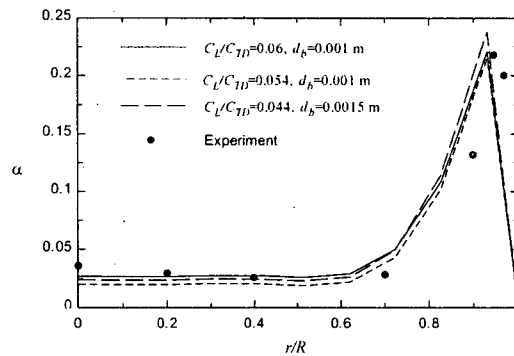


Figure 7.3. A comparison between the predicted and measured void fraction in gas/liquid two-phase flow and the measurements of Serizawa et al. [1975].

7.2. Multidimensional Analysis of Horizontal Gas/Liquid two-Phase Flow

In the past, the complexity of various possible gas/liquid flow patterns has limited the scope and range of situations that could be analyzed using full three-dimensional models. In fact, most computer simulations of multidimensional gas/liquid two-phase flows performed to date have been concerned with vertical tubes or conduits. The reason for that was that in vertical flows gravity mainly affects the axial gas-to-liquid relative velocity, but does not induce any lateral asymmetry in either velocity or phase distribution. On the other hand, in the case of horizontal (or inclined) flows, the acceleration of gravity not only causes a significant flow asymmetry, but also imposes an extra vertical force across the main flow direction, which is typically much stronger than other interfacial forces such as the lift force, for instance. Needless to say, the level of difficulty increases further for two-phase flows in conduits of complex geometries and spatial orientations, where a variety of flow patterns have been observed, each characterized by different interfacial phenomena of mass, momentum and energy transfer.

This Section is concerned with the analysis of two-phase flow in horizontal tubes. Two pipe geometries have been considered: first, a long straight pipe, and then, a similar pipe but with 90° elbow in the mid-section along the flow. In the latter case, the geometry and flow conditions were similar to those used in the air/water experiments performed by Kim et al. [2005].

The combined theoretical and computational approach is based on a complete three-dimensional multifield model which has been implemented in the NPHASE code. Details of the present model are given in Chapters 2 and 3. The proposed model has been tested parametrically for both physical and numerical consistency. Then, the same model has been

used to simulate selected experimental runs reported in [Kin et al, 2005]. The results of comparisons between the predictions and experimental data are shown in Subsection 7.2.5.

7.2.1. Overview of Experimental Facility and Data

A schematic diagram of the test facility documented in [Kim et al., 2005] is shown in Figure 7.4. The experimental test section was made of Pyrex glass tubes 50.3 mm in inner diameter. The measurement ports were made of clear acrylic. In the test section, a 90° elbow was installed at $L/D=197$. The elbow had a radius of curvature of 76.2 mm with an L/D ratio of approximately 6.

For the purpose of measurements, four local ports were installed along the test section, denoted as P1 through P4 in Fig. 7.4. Yet another port (P0) was located right after the two-phase mixing chamber, but it was used only for the local pressure measurements. The next port, P1, was located at $L/D=197$ (9.91 meters from P0), just before the start of the elbow, whereas the ports, P2, P3 and P4, were located at the nondimensional distances, $L/D=225$, 250 and 329 from the mixing chamber, or 1.39m, 2.69m and 6.65m downstream of the start of the elbow, respectively. The measurements of void fraction and velocity were taken at P1, P3 and P4.

Local two-phase flow parameters were measured using double-sensor and four-sensor conductivity probes. In order to capture the asymmetry of distribution of major flow parameters across the horizontal two-phase flow, the measurements were taken along the entire vertical diameter of the tube.

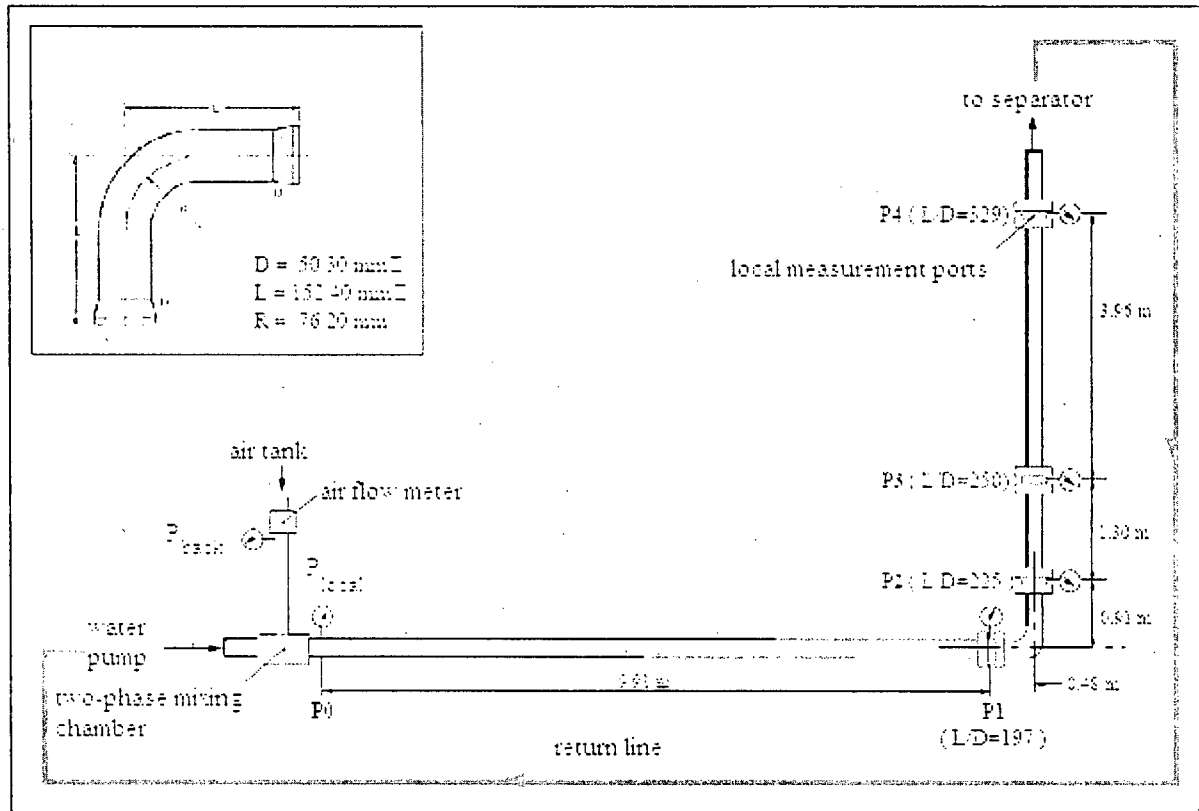


Figure 7.4. A schematic diagram [Kim et al., 2005] of the 50.3 mm ID horizontal two-phase flow test facility with a 90° elbow junction (top view, not to scale).

In total, 15 different j_f & j_g combinations were investigated, all corresponding to slug flow conditions. Sample plots are presented on Figure 7.5. As it can be seen, there is almost no gas in the lower half of the pipe. It is interesting to notice that the void fraction in the upper half first increases dramatically, then stays almost constant and finally increases further near the top of the pipe wall.

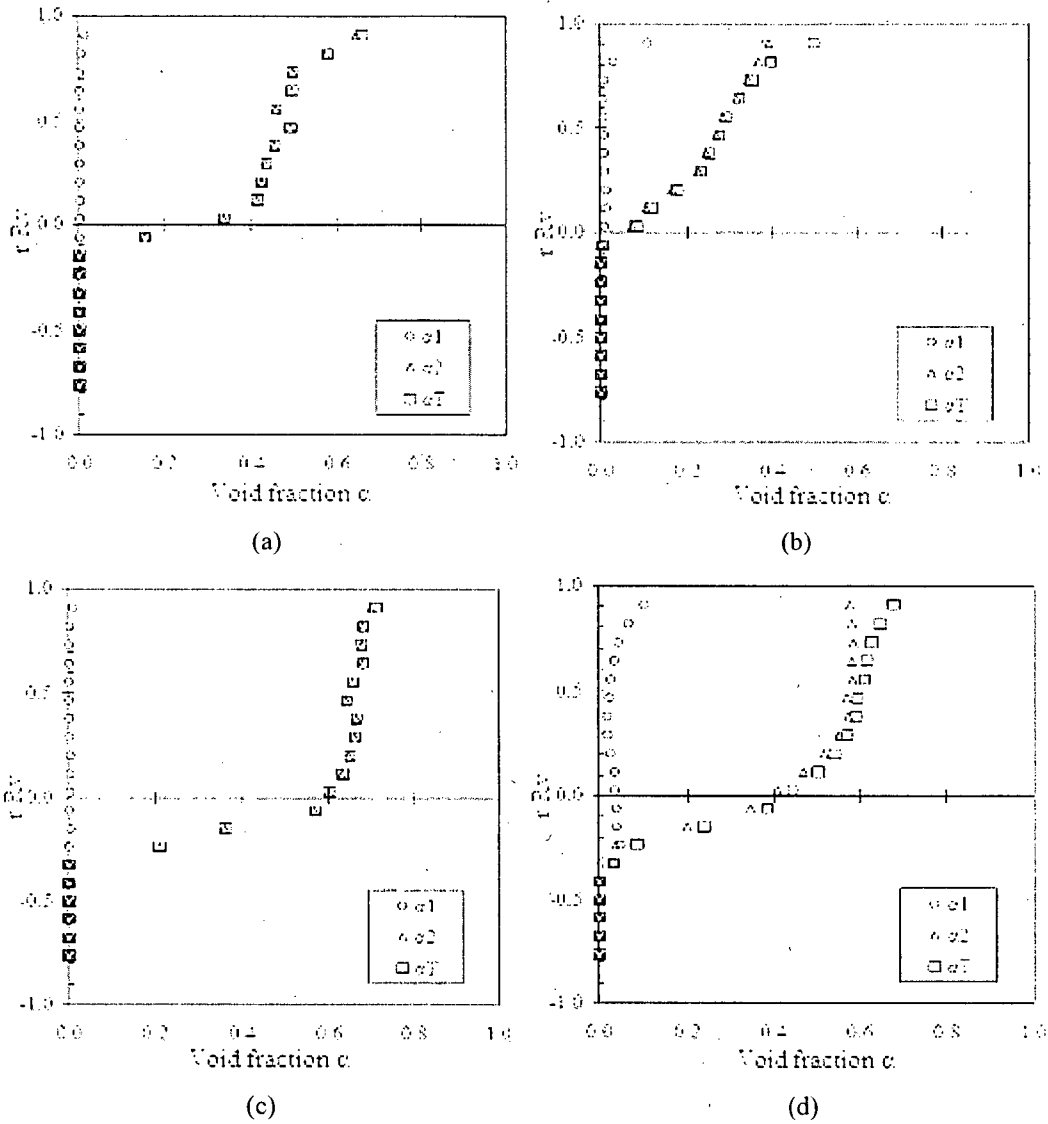


Figure 7.5. Typical profiles of local void fraction acquired along the vertical diameter of the tube with 90 ° elbow [Kim et al., 2005], corresponding to the inlet conditions:

- (a) $j_{g,atm} = 0.287$ m/s, $j_f = 0.559$ m/s; (b) $j_{g,atm} = 0.293$ m/s, $j_f = 1.648$ m/s;
(c) $j_{g,atm} = 0.587$ m/s, $j_f = 0.560$ m/s; (d) $j_{g,atm} = 1.218$ m/s, $j_f = 1.652$ m/s.

The results acquired from the experiments were the local flow rates, local pressure, and two-phase parameters, such as void fraction and bubble velocity. The area-averaged superficial velocity, evaluated as the sum of the products of local void fraction and gas

velocity, was compared against the local superficial velocity measured by a flow meter. As mentioned before, the present measurements were at Port 1, Port 3 and Port 4, and no data was taken at Port 2.

The evolution of void fraction along the experimental section is presented in Fig. 7.6. The experimental data shown in this figure include those at Port 1 (before the elbow), Port 3 and Port 4 (downstream after elbow). They correspond to Run 1, and to the superficial velocities of liquid and gas of 0.56 m/s and 0.27 m/s, respectively. It can be seen that all three curves follow a similar trend and cover the same range of values, although some difference in the void fraction profiles can also be observed. In particular, the highest average void fraction is acquired at Port 3, which is located 2.69 m after the start of the elbow; the minimum is at Port 1.

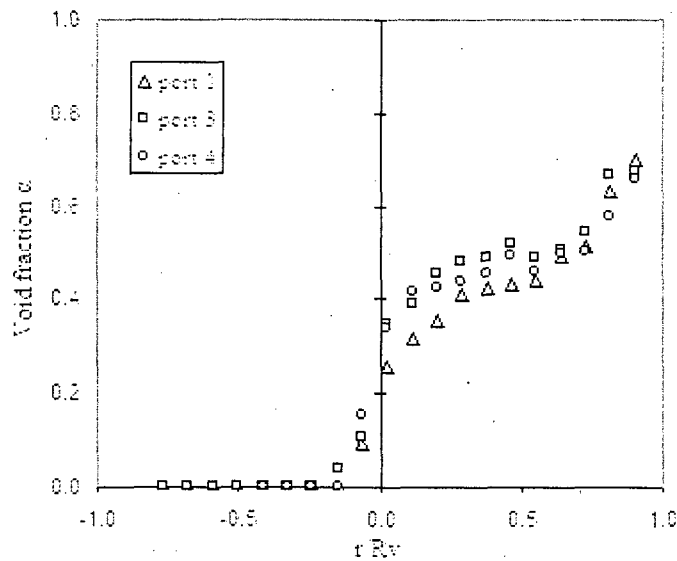


Figure 7.6. Typical lateral profiles of local void fraction acquired at different measurement ports of the tube with 90° elbow [Kim et al., 2005], corresponding to the following inlet conditions: $j_{g,atm} = 0.287$ m/s, $j_f = 0.559$ m/s.

To compare the numerical solution obtained using the NPHASE code with the experimental data, several inlet conditions have been chosen. These conditions are summarized in Table 7.1.

Table 7.1. Summary of test conditions used in the NPHASE simulations

Test number	j_f	$j_{g,atm}$	$j_{loc\ port\ 0}$	$G_{g,loc}$	β
1	0.56	0.287	0.2639	0.3439	0.3203
2	1.65	0.293	0.256	0.3566	0.1343
3	0.56	0.587	0.5384	0.7058	0.4902
4	1.65	1.218	1.0336	1.4822	0.3852

In Table 7.1, $j_{g,atm}$ is the gas superficial velocity equivalent to the atmospheric pressure condition, j_f is the average of the liquid superficial velocities acquired at four measurement ports for each run, $j_{loc\ port\ 0}$ is the gas superficial velocity acquired by the flowmeter at Port 0, $G_{g,loc}$ is the mass flux calculated at Port 0 as a product of $j_{loc\ port\ 0}$ and the gas density, β is the volumetric flow fraction at Port 0.

The experimental data used as a reference in the NPHASE-based numerical solutions have been taken at Port 3 and at Port 4. Since the distance between the elbow and Port 4 was sufficiently long, the conditions there corresponded to a nearly fully developed flow, except for a small change in the fluid properties with decreasing pressure.

The individual terms for the runs listed in Table 7.1 are given in detail in Table 7.2. They are defined as follows: $j_{g,loc}$ is the gas superficial velocity measured by flow meter, $\langle j_g \rangle$ is the calculated area averaged superficial velocity found using the average values of two-phase parameters, $G_{g,loc}$ is the mass flux calculated as a product of $j_{g,loc}$ and the gas density, $\langle G_g \rangle$ is the mass flux calculated as a product of $\langle j_g \rangle$ and the gas density, β_{loc} is volumetric flow fraction corresponding to the local measurement, and $\langle \beta \rangle$ is the volumetric flow fraction corresponding to area-averaged values.

Table 7.2. Summary of the data for air-water slug flow through a horizontal tube of 50.3 mm inner diameter with a 90° elbow

Test #	Gas superficial velocity		Local pressure	Local air density	Gas mass flux		Void fraction	Volumetric flow fraction	
	$j_{g,loc}$	$\langle j_g \rangle$	p (psig)	ρ_{loc}	$G_{g,loc}$	$\langle G_g \rangle$	$\langle \alpha \rangle$	β_{loc}	$\langle \beta \rangle$
Port 3									
1	0.2701	0.2596	1.0	1.286	0.3473	0.3338	0.2530	0.3246	0.3160
2	0.2689	0.3077	1.0	1.286	0.3458	0.3957	0.1150	0.1403	0.1573
3	0.5509	0.4545	1.0	1.286	0.7085	0.5845	0.4430	0.4959	0.4480
4	1.0946	1.0921	1.4	1.319	1.4438	1.4405	0.3380	0.3988	0.3983
Port 4									
1	0.2697	0.2276	1.0	1.286	0.3468	0.2927	0.2440	0.3243	0.2882
2	0.2704	0.3321	1.3	1.311	0.3545	0.4354	0.1230	0.1410	0.1677
3	0.5513	0.4182	1.0	1.286	0.7090	0.5378	0.4220	0.4961	0.4275
4	1.0991	1.0844	1.5	1.327	1.4585	1.4390	0.3470	0.3998	0.3966

In view of measurement errors, the superficial gas velocity at given measurement port obtained by the flow-meter was compared with that obtained by the area-averaged two-phase flow parameters at the same port. It can be seen from Table 7.2 that there are significant differences between the flow conditions obtained by using each method. For example, the maximum error between the local measured and calculated superficial velocities was nearly 20%. Another important observation is concerned with some discrepancies in the measurements of the volumetric flow rates at Port 3 and Port 4. Whereas, for ideal adiabatic flows (at constant pressure) the volumetric flow rates of both phases should be constant along the flow, the actual air expansion due to the frictional pressure drop caused a slight increase in the gas volumetric flow rate (and superficial velocity). As can be seen in Table 2, the measurements for Cases 1, 3 and 4 show just the opposite trend. Needless to say, such experimental errors will have to be accounted for when using the present data for model validation.

7.2.2. Model Validation

The testing and validation of the present model have been performed for three different geometries: flow between parallel plates, flow along a straight cylindrical tube and flow in a tube with a tube with 90° elbow similar to that used in the experiments of Kim et al. [2005].

Case 1. Flow between parallel plates, the inlet conditions correspond to Run 1 of Kim et al. [2005] experiments.

The geometry used in this case is shown in Fig.7.7. The length of plates was 10 m, the distance between the plates was 0.0503 m, and was the same as the diameter of the pipe used in the experiments.

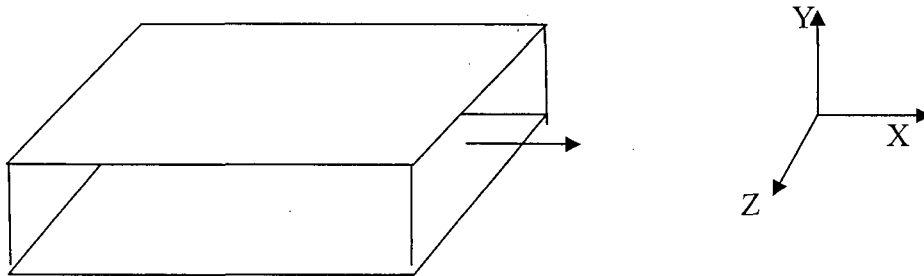


Figure 7.7. An illustration of the numerical grid used in the NPHASE-based simulations of gas/liquid flow

Typical results of NPHASE simulations are shown in Figures 7.8 through 7.10. They illustrate the local distributions of several parameters near the exit of the conduit, where flow conditions were nearly fully-developed.

The void fraction and liquid and gas velocity profiles along the lateral direction in the case of 10% of gravity are shown in Figure 7.8. The calculations have been performed for

the superficial velocities of liquid and gas of 0.56 m/s and 0.27 m/s, respectively. It can be seen that gravity has a strong effect on the void fraction distribution across the channel (between the plates). As can be seen, the relative velocity is practically zero in the current case, which confirms the fully-developed flow conditions.

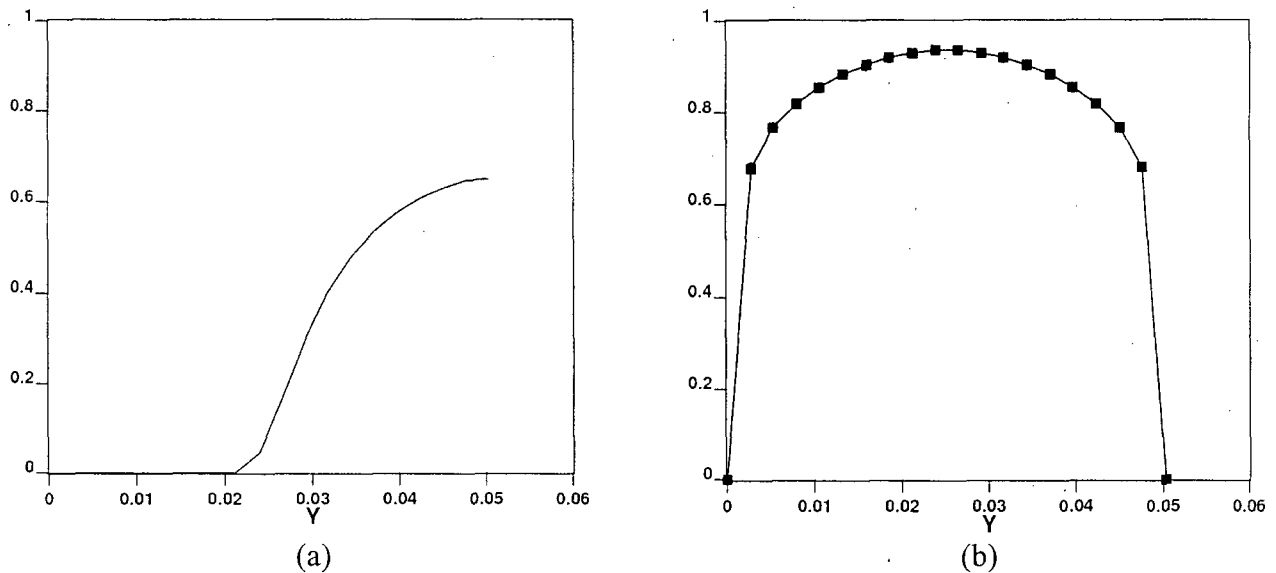


Figure 7.8. Lateral vertical profiles of: (a) void fraction, (b) liquid and gas axial velocities, in two-phase flow between long horizontal plates at 10% gravity.

Similar results for the case of 100% gravity are shown in Figure 7.9. Again, the flow is clearly fully-developed, and the effect of gravity is mainly reflected in a much higher void fraction near the top plate.

Figure 7.10 presents the calculated profiles of turbulent kinetic energy and turbulent energy (ϵ_c) dissipation for the liquid phase at fully-developed flow conditions. The calculations show that both profiles only slightly depart from axial symmetry. Such a trend can be deduced from the analysis of Eq.(2.20) and Eq.(4.7) and Eq.(4.8). Specifically, for

fully-developed flow between parallel plates, the governing equations reduce to a one-dimensional form. If, furthermore, the term, $\frac{d(\alpha_c v_c')}{dy} \frac{d\psi}{dy}$ ($\psi = k_c, \epsilon_c$), is small compared to the other terms on the right hand sides of Eq.(4.7) (with (where $\psi = k_c$) and Eq.(4.8) (with $\psi = \epsilon_c$), the local phase concentration ($\alpha_c = 1 - \alpha$) becomes a multiplication factor in all three equations and effectively has no effect on the distributions of: axial velocity, turbulent kinetic energy and turbulent energy dissipation. Thus, for such flow conditions, the most dramatic impact of gravity is on the lateral void fraction.

As it is shown in the next section, the near-symmetry disappears for flows in horizontal circular tubes.

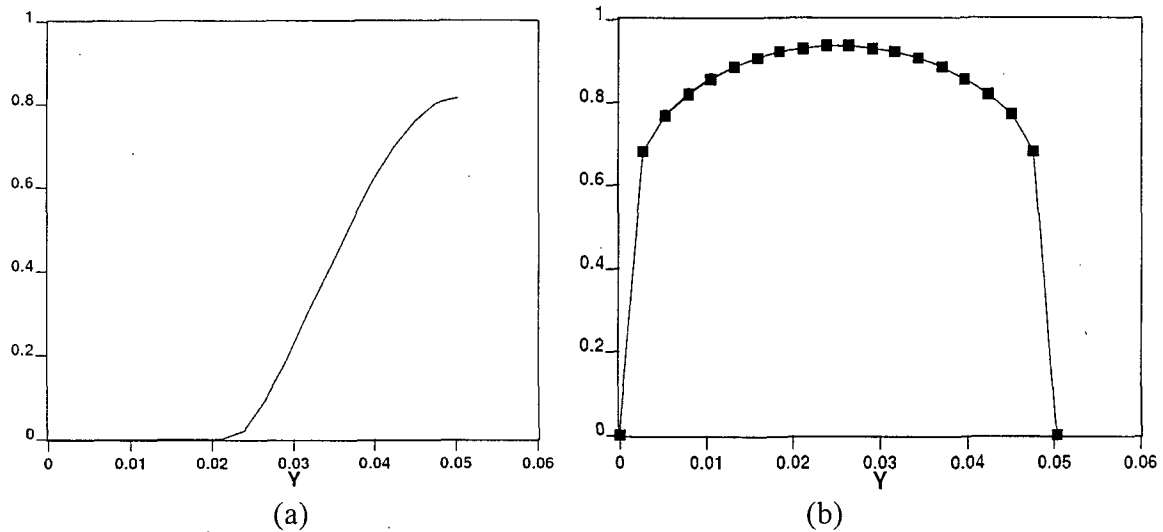


Figure 7.9. Lateral vertical profiles of: (a) void fraction, (b) liquid and gas axial velocities, in two-phase flow between long horizontal plates at 100% gravity.

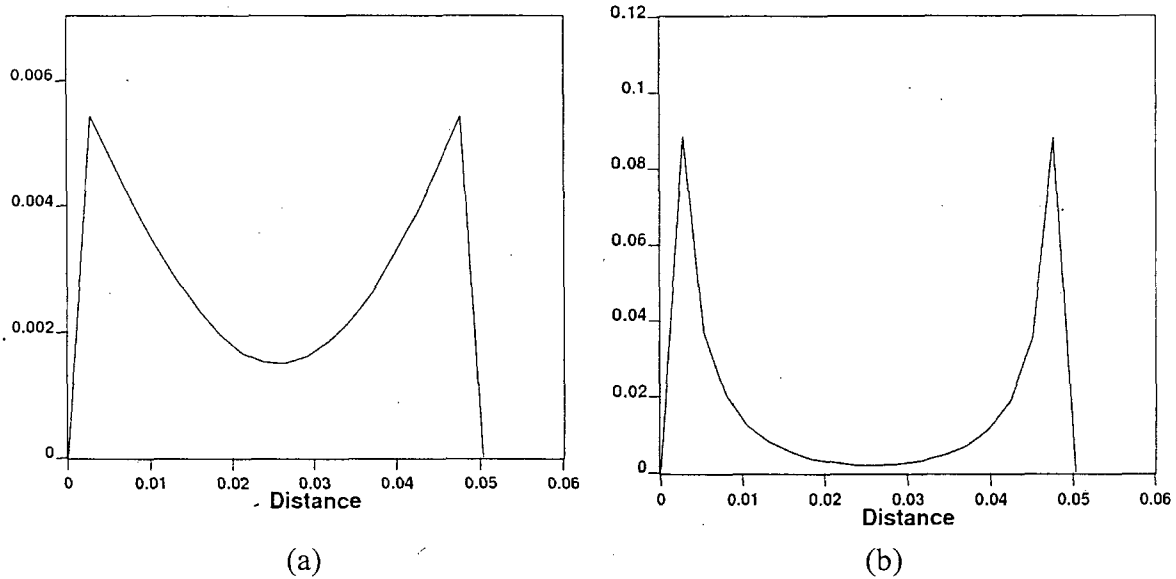


Figure 7.10. Lateral vertical profiles of: (a) turbulent kinetic energy, (b) turbulent energy dissipation rate, for flow between long horizontal parallel plates at 100% gravity.

Case 2. Flow in a straight horizontal tube, the inlet conditions correspond to Run 1 of Kim et al. [2005] experiments.

The purpose of this series of simulations was to examine the effect of the cross-sectional shape of the conduit on the velocity and phase distributions in horizontal two-phase flows, and to test the ability of the NPHASE-implemented model to predict flow conditions in circular pipes. Specifically, a 5 m long, 0.0503 m in diameter circular tube was used in the calculations. These pipe dimensions are similar to those used in the experiments of Kim et al. [2005]. The corresponding computational grid is shown in Figure 7.11.

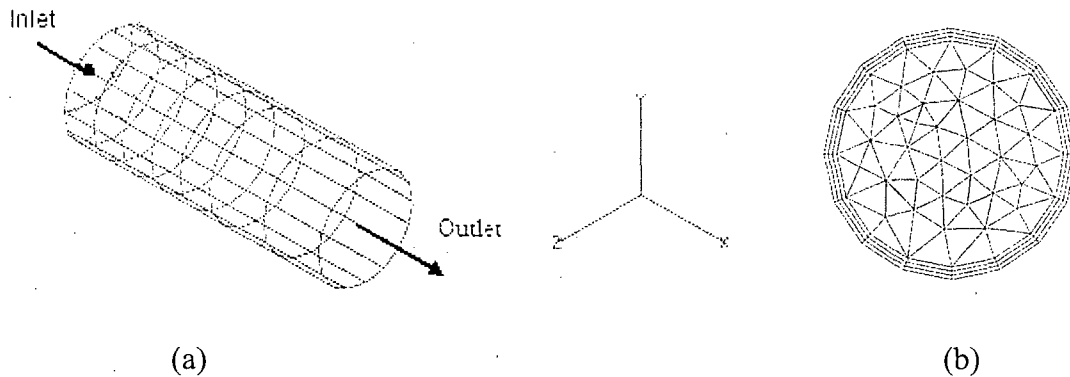


Figure 7.11. An illustration of the three-dimensional numerical grid used in the NPHASE-based simulations of gas/liquid flow: (a) axial nodalization, (b) mixed structured and unstructured grid across the flow area in the pipe.

It is important to notice that the present unstructured grid, combined with pseudo-structured discretization pattern near the pipe wall, allows one to fully capture three-dimensional effects of gravity on flow parameters across the pipe.

The results of NPHASE calculations are shown in Figures 7.12 – 7.13. These results refer to the axial position near the exit of the pipe where nearly-fully-developed flow conditions occur ($L/D \approx 100$). The results have been obtained for the case of full gravity.

The void fraction and velocity profiles along the vertical diameter of the pipe are shown in Figure 7.12. The calculations have been performed for the superficial velocities of liquid and gas of 0.56 m/s and 0.27 m/s, respectively. It can be seen that gravity has a strong effect on the void fraction distribution across the channel (between the plates). As can be seen, the relative velocity is practically zero in the current case, which confirms the fully-developed flow conditions.

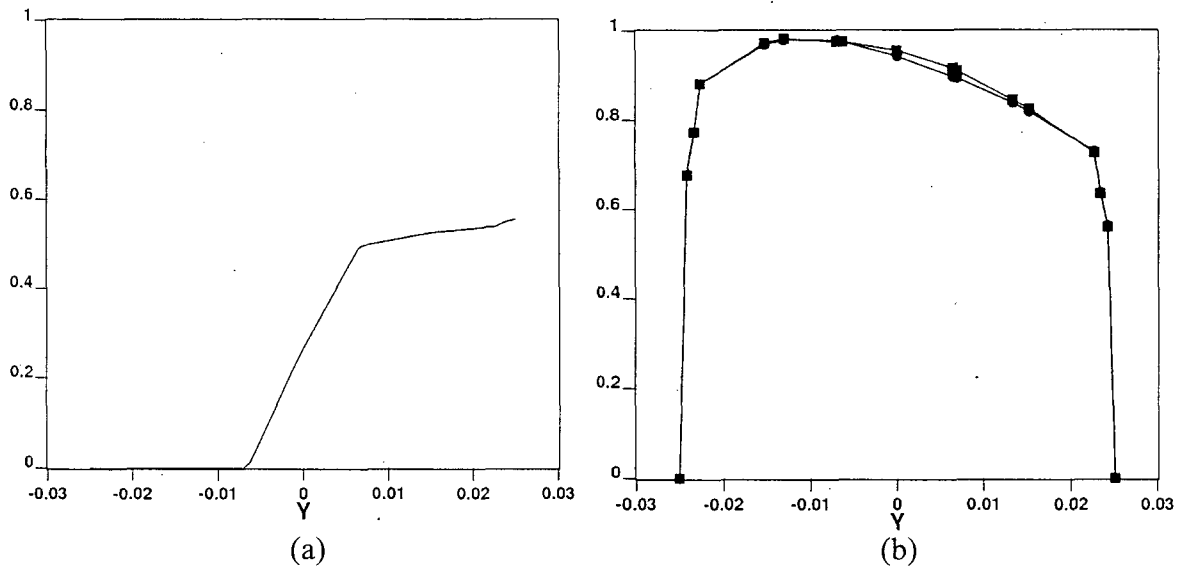


Figure 7.12. Lateral profiles along the vertical diameter of: (a) void fraction, (b) liquid and gas axial velocities, for two-phase flow near the exit of a long straight horizontal tube.

The calculations have been performed for the superficial velocities of liquid and gas of 0.56 m/s and 0.27 m/s, respectively. It can be seen that gravity has a strong effect on both void fraction and velocity distributions along the vertical diameter of the tube. In particular, the velocity profiles are bottom-peaked, when void fraction is higher at the upper half of the tube. Both results correspond to an axial location near the exit of the tube, where near-fully-developed flow conditions occur.

Figure 7.13 presents the radial distributions of turbulent kinetic energy and turbulent energy dissipation rate along the vertical diameter of the tube. The axial location is the same as in Figure 7.12. It can be seen that, due to the effect of gravity, both parameters experience significant asymmetries around the centerline of the horizontal tube.

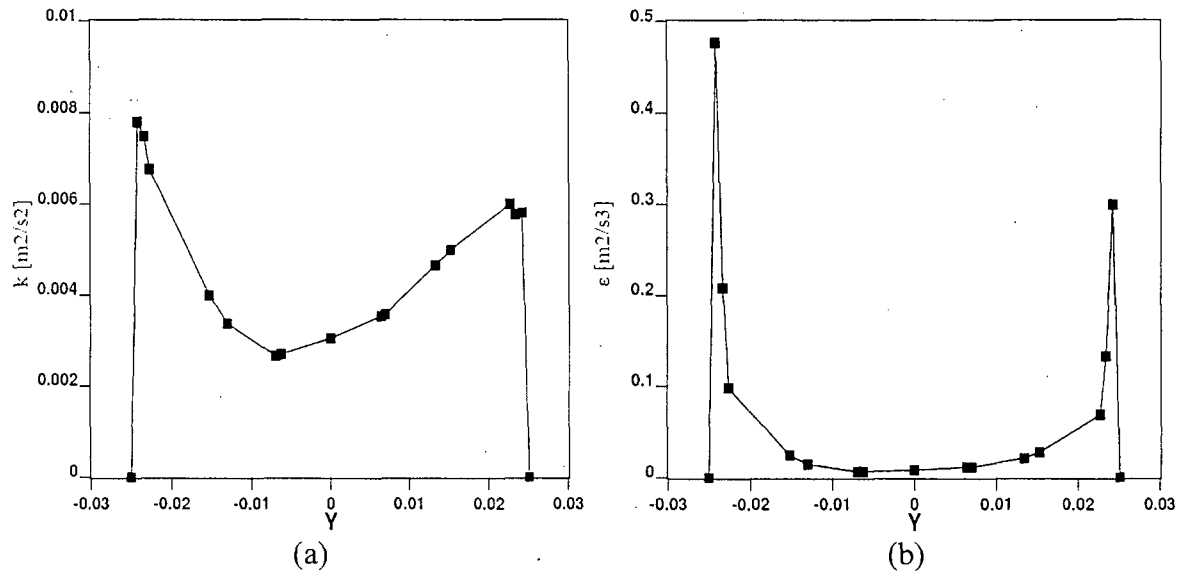


Figure 7.13. Lateral profiles along the vertical diameter of: (a) turbulent kinetic energy, (b) turbulent energy dissipation rate, for two-phase flow near the exit of a long straight horizontal tube

Case 3. Flow in a horizontal tube with 90° elbow, using the experimental conditions of Kim et al. [2005] experiments.

The purpose of the present simulations was to directly validate the proposed model against the experimental data of Kim et al. [2005]. Two experimental runs were used in the NPHASE simulations: Run#1 and Run # 2 in Table 7.1. The computational grid used for both runs is shown in Fig. 7.14.

Fig. 7.14(a) shows the axial nodalization of the pipe with elbow, whereas Fig. 7.14(b) presents the unstructured grid used across the pipe. The lateral nodalization pattern was the same as used before for the straight pipe case (Case-2). As it was already mentioned before, the pseudo-structured (regular) portion of the grid near the pipe wall helps to properly capture the wall effect on local velocity and phase distributions there.

According to the system of coordinates shown in Fig. 7.14, the main flow direction gradually changes from that along z at the inlet to that along x at the outlet, whereas y always defines the vertical coordinate across the flow. Consequently, the gravity vector becomes $\mathbf{g} = \{g_x, g_y, g_z\}$, where $g_x = g_z = 0$, $g_y = -g$.

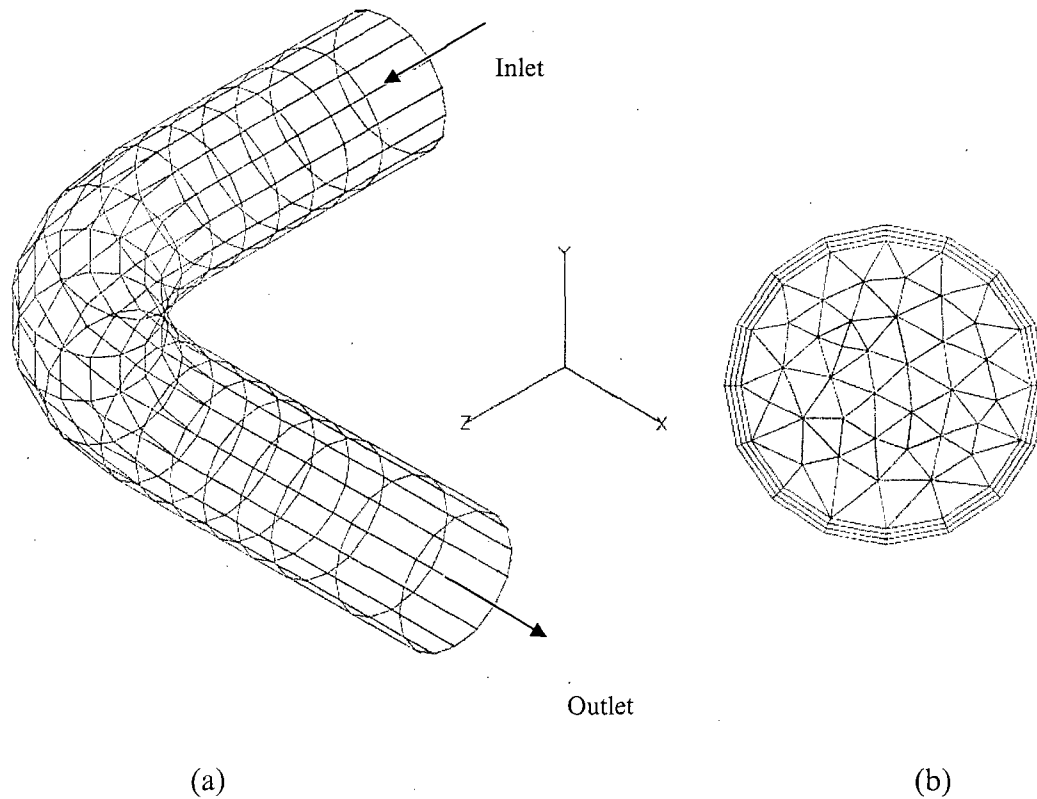


Figure 7.14. An illustration of the three-dimensional numerical grid used in the NPHASE-based simulations of gas/liquid flow in a horizontal tube with 90° elbow: (a) the axial mesh, (b) the cross-sectional mesh.

Figure 7.15 shows the pressure distribution along the pipe with 90° elbow for two experimental conditions corresponding to Run 1 and Run 2. The change in pressure has been considered separately along the inner and outer edges of the elbow. It is interesting to notice

that the pressure at the outer edge of the elbow is higher than at the inner edge. This is due to the formation of secondary flows inside the elbow. In Figure 7.15 (b), the pressure along the centerline of a straight horizontal tube is also shown. The axial pressure gradient along the straight sections of the pipe with elbow is practically the same as that for a straight tube. The differences in the calculated values of pressure are due to the different length of each pipe, and the assumed same pressure of reference at the outlet.

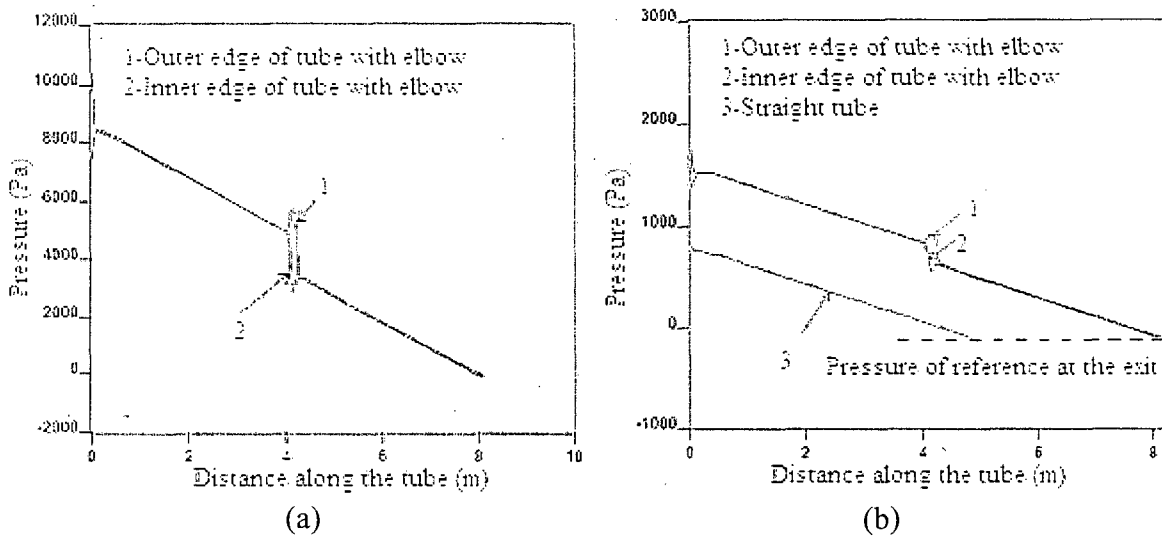


Figure 7.15. Pressure distribution along the centerline of a straight horizontal tube and along the outer and inner edges of a horizontal tube with 90° elbow for the experimental conditions of Kim et al. [2005]: (a) Run 1, (b) Run 2.

Figures 7.16 - 7.19 show parametric effects of selected modeling assumptions on the void fraction distribution along the vertical diameter, corresponding to Port 4 in Run 1 of the experiment. The results of NPHASE predictions have been compared against the experimental data. Figure 7.16 illustrates the effect of turbulent dispersion force coefficient on the void distribution along the central vertical axis of the pipe (from the bottom to the top of the pipe). The value, $C_{TD} = 0.33$, corresponds to isotropic turbulence distribution. As can

be seen, reducing this coefficient to, $C_{TD} = 0.3$, which effectively means increasing the effect of the axial component of turbulent kinetic, $(\overline{w_t'^2})$, makes almost no difference in the calculated void profile. Thus, it can be clearly seen that gravity plays a dominant role in the void distribution.

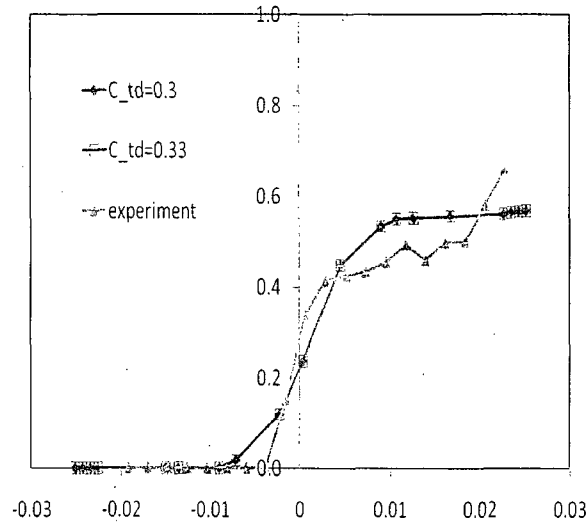


Figure 7.16. The effect of turbulent dispersion coefficient on void fraction distribution across the vertical diameter in a horizontal tube with 90° elbow at Port 4 for Run 1 of the experiments by Kim et al., [2005].

Figure 7.17 presents the parametric effect of drag force coefficient on the void distribution along the vertical axis of the horizontal tube with elbow. The Figure shows the results obtained downstream from the elbow at the location corresponding to Port 4 in Run 1 of the experiment. As can be seen, increasing the drag coefficient by a factor of 2.5, from 0.4 to 1, has a very small impact on the predictions. This is because in horizontal flows, the axial liquid and gas velocities are similar in magnitude, and the relative velocity is not very sensitive to changes in the drag coefficient.

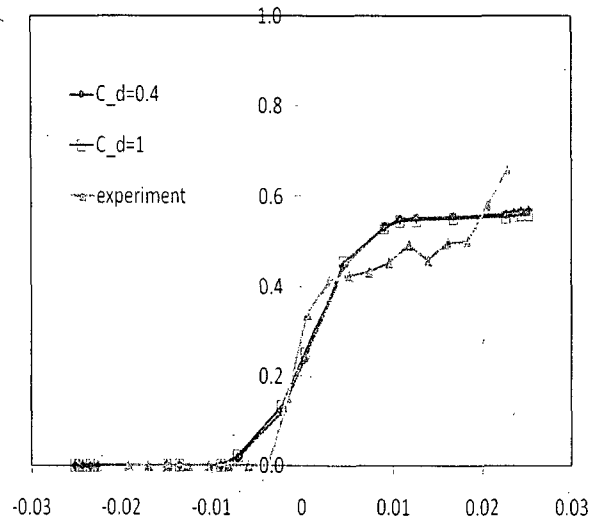


Figure 7.17. The effect of drag force coefficient on void fraction distribution in a horizontal tube with 90° elbow at Port 4 in Run 1 of the experiments reported by Kim et al. [2005].

Figure 7.18 presents the parametric effect of reaction force coefficient on void distribution along the vertical axis of the tube with elbow at the location corresponding to Port 4 in Run 1 of the experiment. The considered values of the coefficient C_R are 9.3, 9.5, 9.7, where $C_R = 9.5$ was used as a reference value in the remaining calculations shown in this chapter.

As it was mentioned in previous chapters that the wall force is transmitted across the near-wall bubbles, and for large bubbles the range of this force may extend over some distance from the upper wall. Figure 7.19 shows the effect of the critical boundary of the region where wall force is not zero. As expected, the void fraction profile starts to increase farther from tube bottom, and becomes steeper, with increasing y_c . This, in turn, causes an increase in the void fraction neat the top of the pipe.

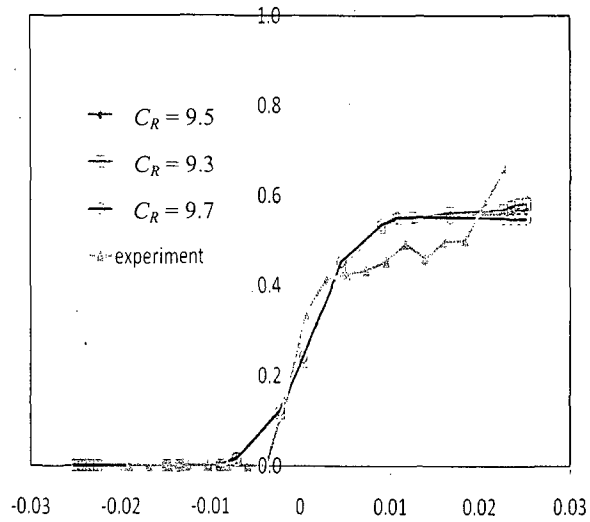


Figure 7.18. The effect of the coefficient, C_R , on void fraction distribution in a horizontal tube with 90° elbow, corresponding to Port 4 in Run 1 of the experiment reported by Kim et al. [2005].

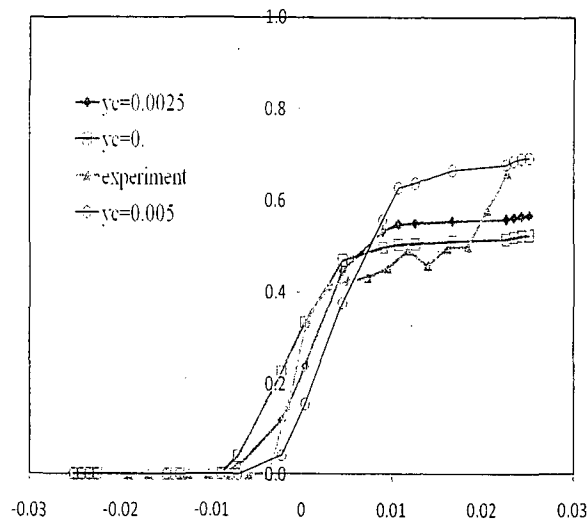


Figure 7.19. The effect of critical boundary, y_c , on void fraction distribution in a horizontal tube with 90° elbow, corresponding to Port 4 in Run 1 of the experiment reported by Kim et al. [2005].

It can be seen in Figure 7.19, changing the value of this coefficient by as much as 20% of the radius of the tube does not have a dramatic effect on the void distribution, and the results of all three parametric runs lie within the range of uncertainties of the measurements. The actual value of y_c depends on bubble size, especially the size of large elongated bubbles, which was not measured in the experiment. On the other hand, the theoretical predictions of bubble size would require a separate model development, beyond the current multifield modeling framework.

The results illustrating the effect of the elbow on phase distribution at the end of the pipe are shown in Figure 7.20. As can be seen, the void profiles for the cases without and with the elbow are very similar. These results confirm that the exit conditions in the experiments were nearly fully-developed, as expected. At the same time, they show the consistency and numerical accuracy of the NPHASE solver.

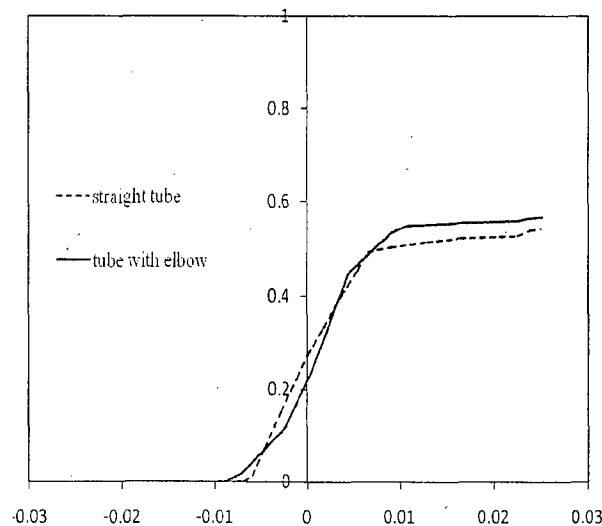


Figure 7.20. The NPHASE-predicted radial void fraction profiles at the exit of a straight horizontal tube and a similar tube with a 90° elbow.

Figure 7.21 shows the gas and liquid velocity profiles along the vertical diameter of a horizontal tube with elbow. These distributions refer to the downstream section of the tube, namely to Port 4 of Run 1 of the experiment. As can be seen, gravity has a strong effect on velocity distributions along the vertical diameter of the tube; in particular the velocity profiles are bottom-peaked.

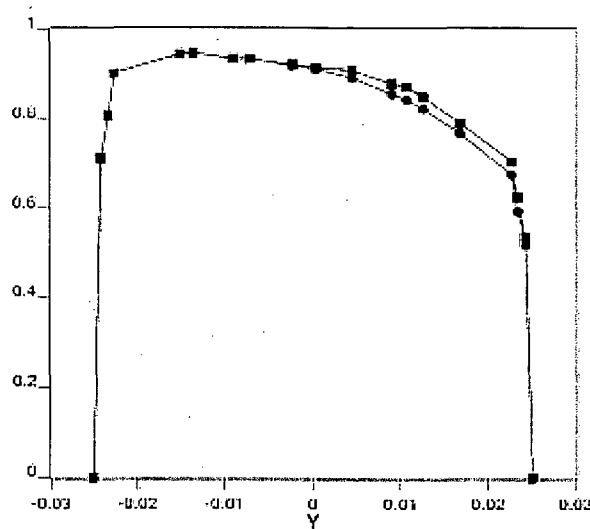


Figure 7.21. The NPHASE-predicted radial liquid and gas velocity profiles in a horizontal tube with 90° elbow, corresponding to Port 4 in Run 1 of the experiments reported by Kim et al. [2005].

The radial void fraction and gas velocity profiles at several cross sections along the 90° elbow of the horizontal tube for Run 1 of the experiments are shown on Figure 7.22. These results correspond to the superficial liquid and gas velocities are 0.56 m/s and 0.27 m/s, respectively.

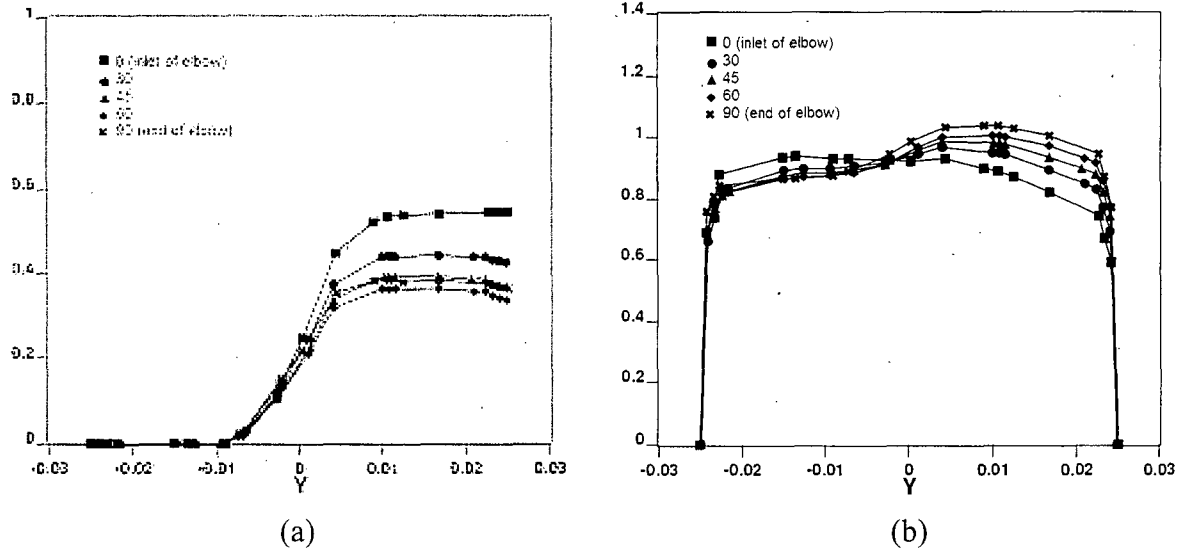


Figure 7.22. The NPHASE predicted profiles of: (a) radial void fraction, (b) gas velocity, at several sections along the 90° elbow of a horizontal tube for Run 1 of the experiments reported by Kim et al. [2005].

The results shown in Figure 7.22 clearly demonstrate the effect of the elbow on local void and velocity distributions as a function of the angular position along the elbow. As it can be seen, the lateral profile of the axial velocity undergoes a gradual transition from nearly-fully developed to top-peaked at the 90° angle. Downstream of the elbow, the velocity profile gradually changes again, and eventually approaches the bottom-peaked shape shown in Figure 7.21. The local void fraction in the upper part of the tube (along the central vertical axis) decreases while going through the elbow, since bubbles tend to move to the inner edge of tube in the elbow. This is shown in Fig.7.23, where the radial void fraction and gas velocity profiles along the horizontal diameter are plotted at several cross sections along the elbow (in this Figure, the zero value of the distance corresponds to the inner edge of the elbow).

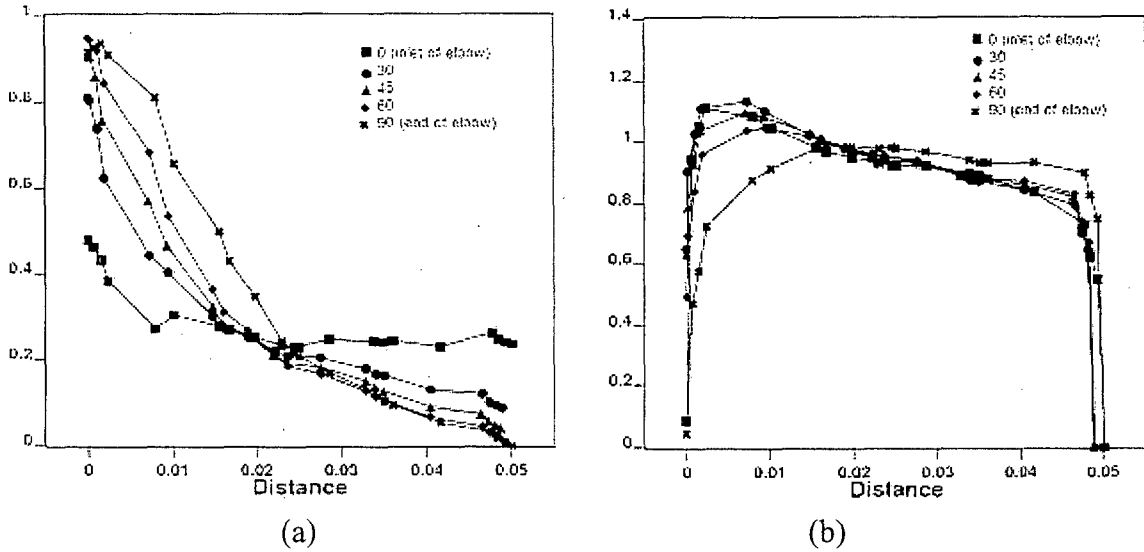


Figure 7.23. Distributions along the horizontal diameter of: (a) radial void fraction, (b) gas velocity [m/s], at several angular sections along the 90° elbow of a horizontal tube for Run 1 of the Kim et al. [2005] experiments.

Figure 7.24 presents the turbulent kinetic energy and turbulent energy dissipation rate along the vertical diameter at Port 4 of the horizontal tube with 90° elbow. The asymmetry of both profiles due to the effect of gravity can be clearly seen there.

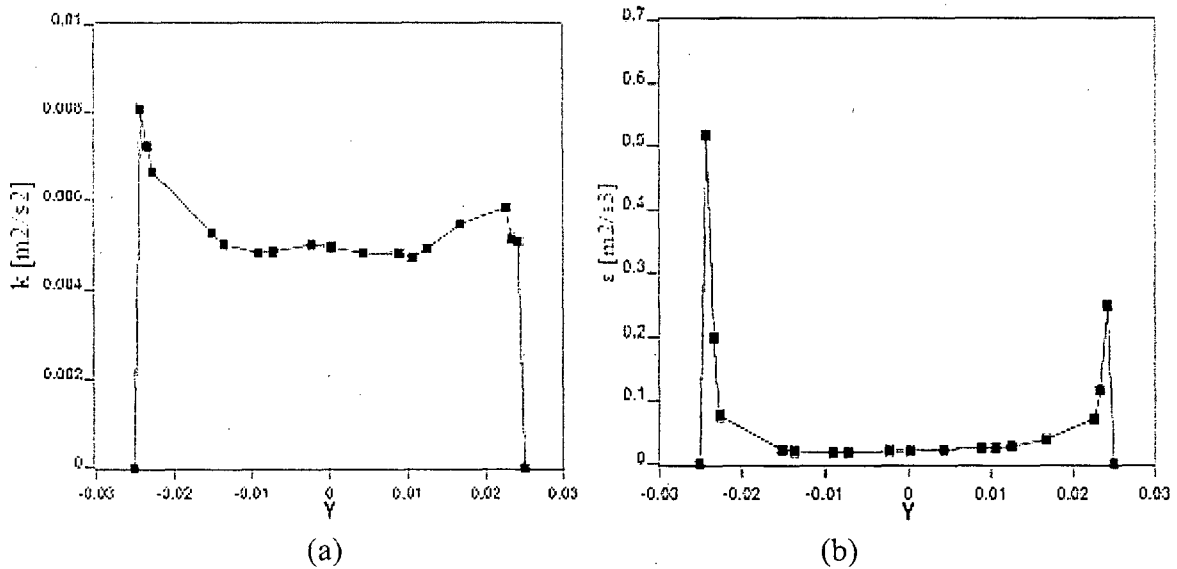


Figure 7.24. Lateral distributions of: (a) turbulent kinetic energy, (b) turbulent energy dissipation, along the vertical diameter, for the conditions shown in Figure 7.21.

The secondary velocity vectors at different cross-sections along the 90° elbow are presented in Figure 7.25. The superficial liquid and gas velocities are 0.56 m/s and 0.27 m/s, respectively, and they correspond to the experimental Run 1. As can be seen, the secondary flows undergo a gradual transition from nearly fully-developed to top-peaked. Downstream of the elbow, the secondary velocity vectors gradually change again and eventually approach the nearly-fully developed conditions, as shown in Figure 7.25(f). The asymmetry of all velocity profiles is due to the combined effects of curvature and gravity.

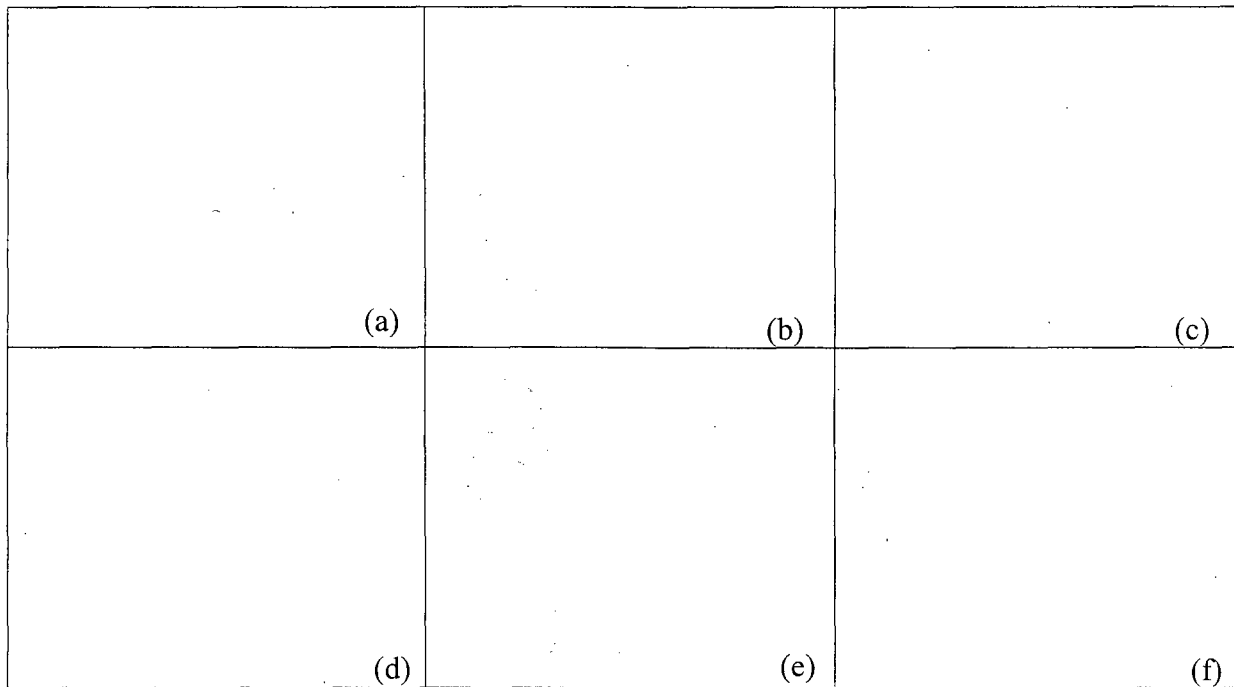


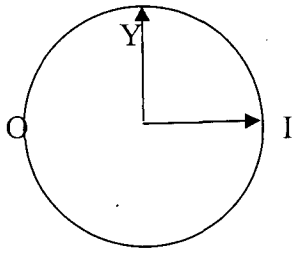
Figure 7.25. The flow field at various angular positions along the 90° elbow. The secondary velocity vectors are shown at: (a) 0° , (b) 30° , (c) 45° , (d) 60° , (e) 90° sections of the elbow, (f) near the exit of the tube at nearly fully developed flow. The calculations were performed for Run 1 of the Kim et al. [2005] experiments.

The cross-sectional view of the flow inside the elbow is presented on Fig.7.26. The color contours shown there represent the void fraction distribution inside the elbow. A gradual transition of the void fraction distribution across the tube can be clearly observed. In particular, as the heavy liquid water tends to move closer to the outer edge of the tube due to the effect of centrifugal force, air bubbles moves closer to the inner side. At fully developed conditions near the end of the tube the symmetry of void distribution along horizontal diameter is practically fully recovered.

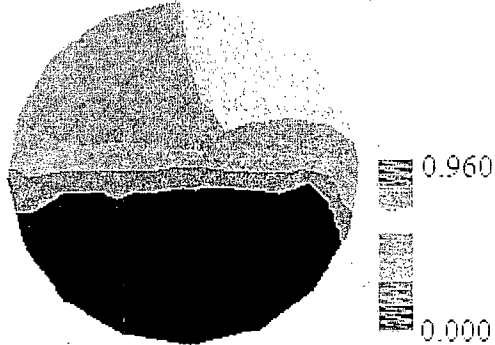
The results in Figure 7.27 show a comparison between the two-phase flow characteristics at the half-radius distance from the centerline and the results obtained at the centerline. The plots of both void fraction and gas velocity are along the vertical diameter at the location corresponding to Port 4 in Run 1 of the experiments.

Figures 7.28 through 7.36 show the results of NPHASE simulations for Run-2 in Table 7.1. The calculations have been performed for the superficial velocities of liquid and gas of 1.65 m/s and 0.27 m/s, respectively. The results of predictions have been compared against the corresponding experimental data.

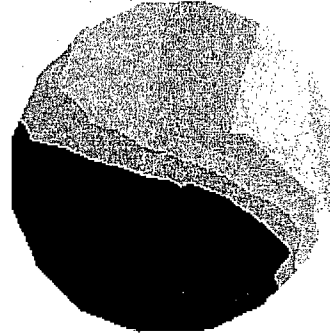
Figures 7.28 through 7.31 present the parametrical effects of selected modeling assumptions on the void fraction distribution along the vertical diameter at the axial location downstream from the elbow, where nearly-fully-developed conditions exist. These results correspond to initial conditions of Run 2 in the experiments reported by Kim et al. [2005]. The results of NPHASE predictions have been compared against the experimental data.



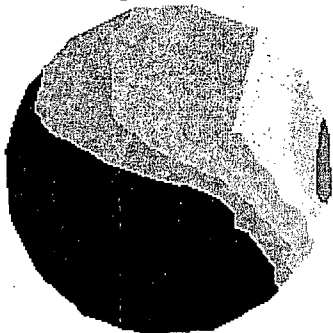
At the inlet of elbow - 0° angle



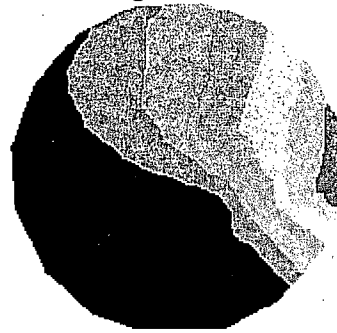
At 30° angle of elbow:



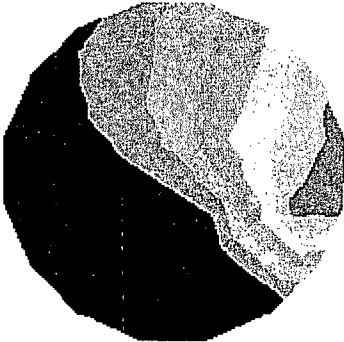
At 45° angle of elbow:



At 60° angle of elbow:



At the exit of elbow - 90° angle:



At nearly fully-developed region:

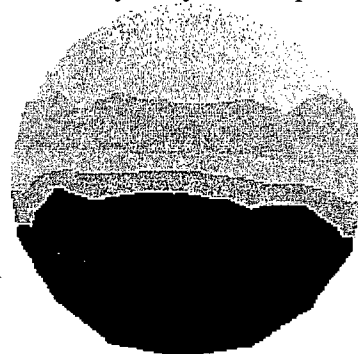


Figure 7.26. Color contours of void fraction at various angular locations along the 90° elbow, and at tube exit, for Run 1 of the Kim et al. [2005] experiments.

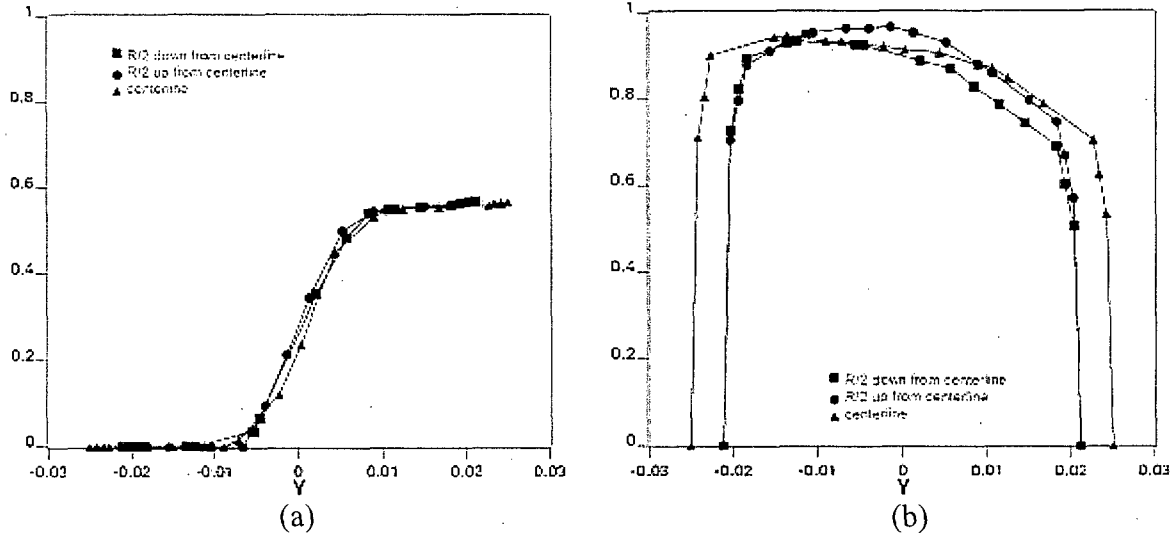


Figure 7.27. The radial void fraction and gas velocity profiles at $\frac{1}{2}$ radius from the symmetry line in a horizontal tube with 90° elbow, corresponding to Port 4 in Run 1

The different void fraction distributions between the results for Run 2 and Run 1 are mainly due to different inlet conditions. For example, the gas-to mixture superficial velocity ratio was 13% for Run 2, compared to 24% for Run 1. Consequently, the effect of smaller dispersed bubbles on a gradual increase in the void fraction near the top of the tube can be seen in Figure 7.28. Since there was no information about the bubble sizes observed in the experiments, this effect was only partially captured by the present model.

Figure 7.28 also shows the effect of turbulent dispersion force coefficient on void distribution along the vertical diameter of the tube (from the bottom to the top). As before, a change in the value of this coefficient can be interpreted as a measure of degree of departure from turbulence isotropy. It can be seen that the void fraction profile is not very sensitive to the changes in the turbulent dispersion force coefficient, and that gravity still plays a dominant role in the void distribution.

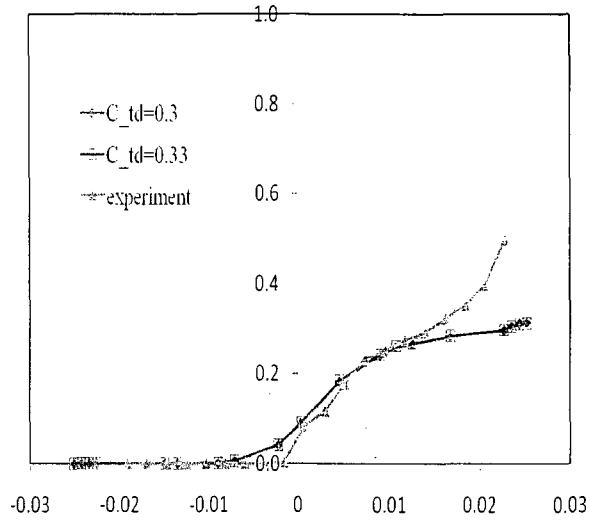


Figure 7.28. The effect of turbulent dispersion coefficient on void fraction distribution in a horizontal tube with 90° elbow, at Port 4 for Run 2 of the experiments by Kim et al. [2005].

Figure 7.29 presents the effect of drag coefficient on void distribution along the vertical axis of the tube with elbow. The values of the coefficient, C_D , are the same as those shown in Figure 7.17 for Run 1. Again, the observed changes in the void fraction are very small.

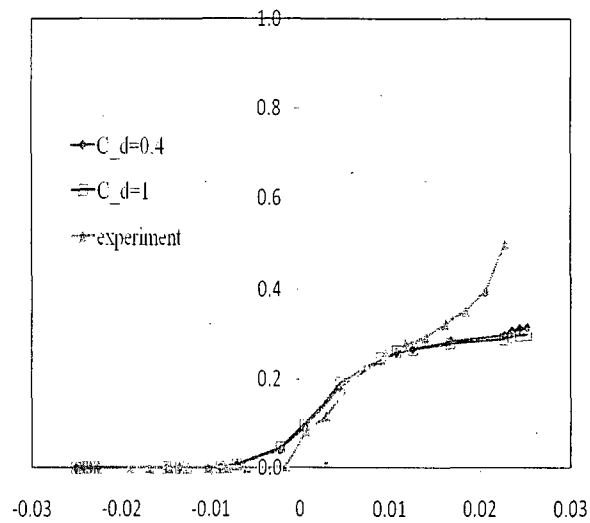


Figure 7.29. The effect of drag coefficient on void fraction distribution in a horizontal tube with 90° elbow, at Port 4 in Run 2 of the experiments by Kim et al. [2005].

Figures 7.30 and 7.31 present parametric effects on void distribution of the reaction force coefficient and critical boundary, respectively, for Run 2. The range of changes and the observed trends are similar as those for Run 1 (see Figures 7.18 and 7.19).

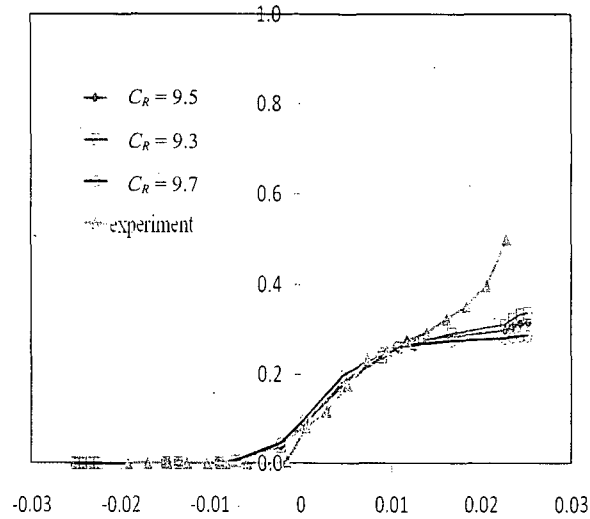


Figure 7.30. The effect of the reaction force coefficient, C_R , on void fraction distribution in a horizontal tube with 90° elbow at Port 4 in Run 2 [Kim et al., 2005].

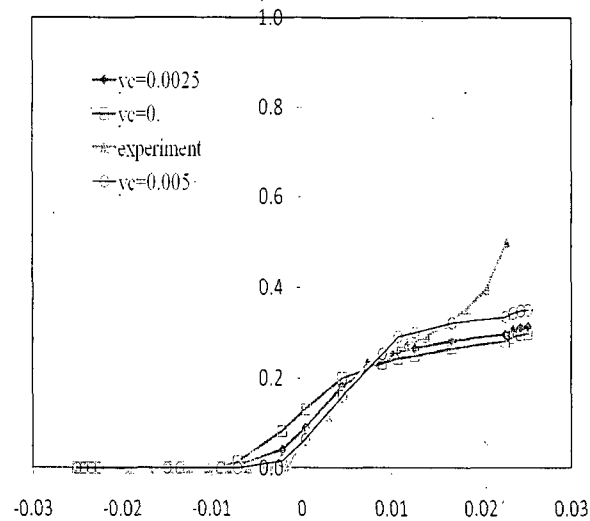


Figure 7.31. The effect of critical boundary, y_c , on void fraction distribution in a horizontal tube with 90° elbow at Port 4 in Run 2 [Kim et al., 2005].

Figure 7.32 shows the gas and liquid velocity profiles along the vertical diameter. The distributions refer to the downstream section of the tube, namely to Port 4 of Run 2 of the experiment. The gravity has an effect on velocity distributions along the vertical diameter of the tube, but in the current case the velocity profile is more symmetrical than for Run 1 (see Figure 7.21). The reason for this that in the current case the liquid velocity is much higher than in the previous case, and the gas-to-total volumetric flow rate ratio is relatively small, $j_{v,av} / (j_{v,av} + j_{l,av}) = 0.13$.

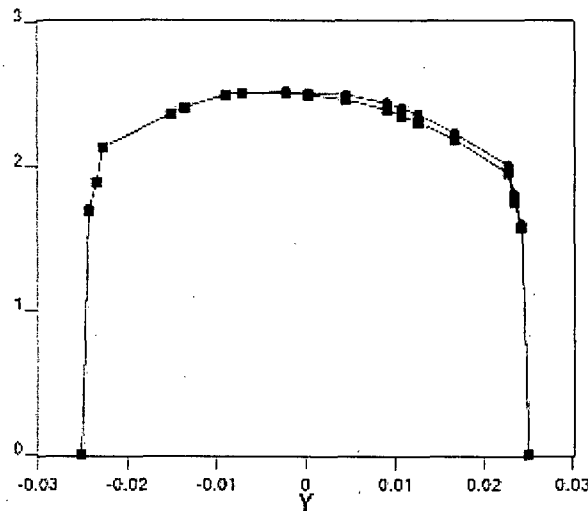


Figure 7.32. The NPHASE-predicted radial liquid and gas velocity profiles in a horizontal tube with 90° elbow, corresponding to Port 4 in Run 2 of the experiments reported by Kim et al. [2005].

Figure 7.33 illustrates the lateral changes in the turbulent kinetic energy and turbulent energy dissipation rate along the vertical diameter at Port 4 for Run 2 of the experiments. Again, both plots experience a certain degree of gravity-driven asymmetry; however this effect is smaller than for Run 1 (see Figure 7.24).

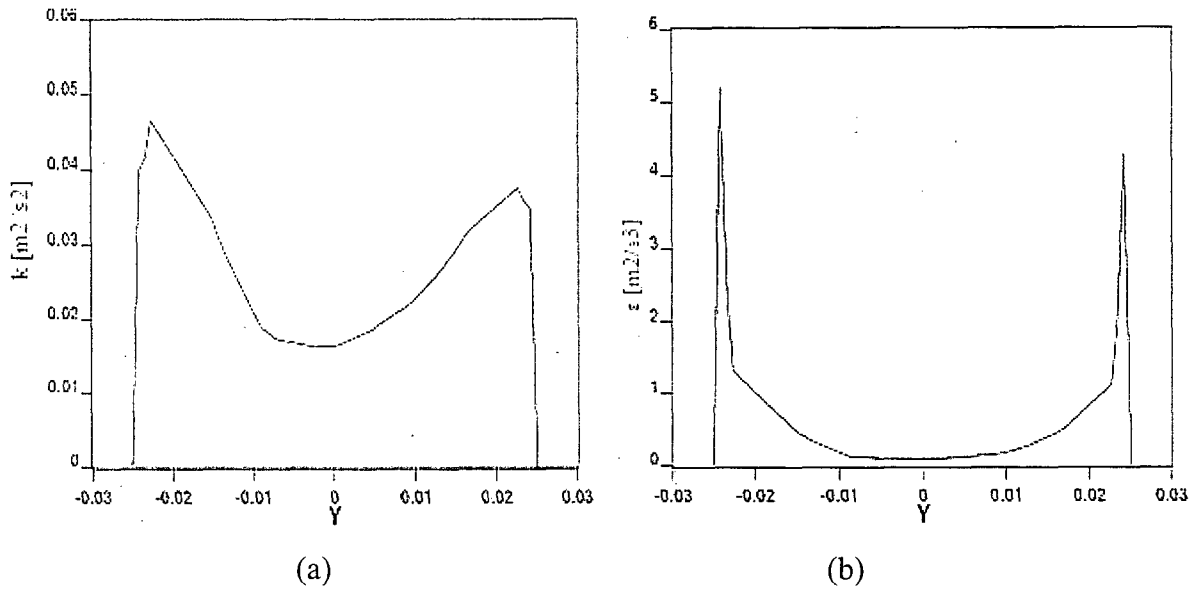


Figure 7.33. Lateral distributions of: (a) turbulent kinetic energy, (b) turbulent energy dissipation, along the vertical diameter, for the conditions shown in Figure 7.32.

The radial void fraction and gas velocity profiles at several cross-sections along the 90° elbow in a horizontal tube for Run 2 of the experiments are shown on Figure 7.34. Here, the effect of elbow on void and velocity distributions can be clearly seen. Specifically, the axial velocity profile undergoes a gradual transition from nearly-fully developed to top-peaked at the 90° angle. Downstream of the elbow, the velocity profile gradually changes again, and it eventually approaches the nearly fully developed profile near the tube exit. The local void fraction above the centerline significantly decreases while going through the elbow. The reason for this is that gas bubbles move toward the inner edge of the elbow, as shown on Fig.7.35.

Figure 7.35 illustrates the corresponding radial void fraction and gas velocity profiles along the horizontal diameter at several cross-sections along the elbow. In this Figure, the zero location corresponds to the inner edge of the elbow.

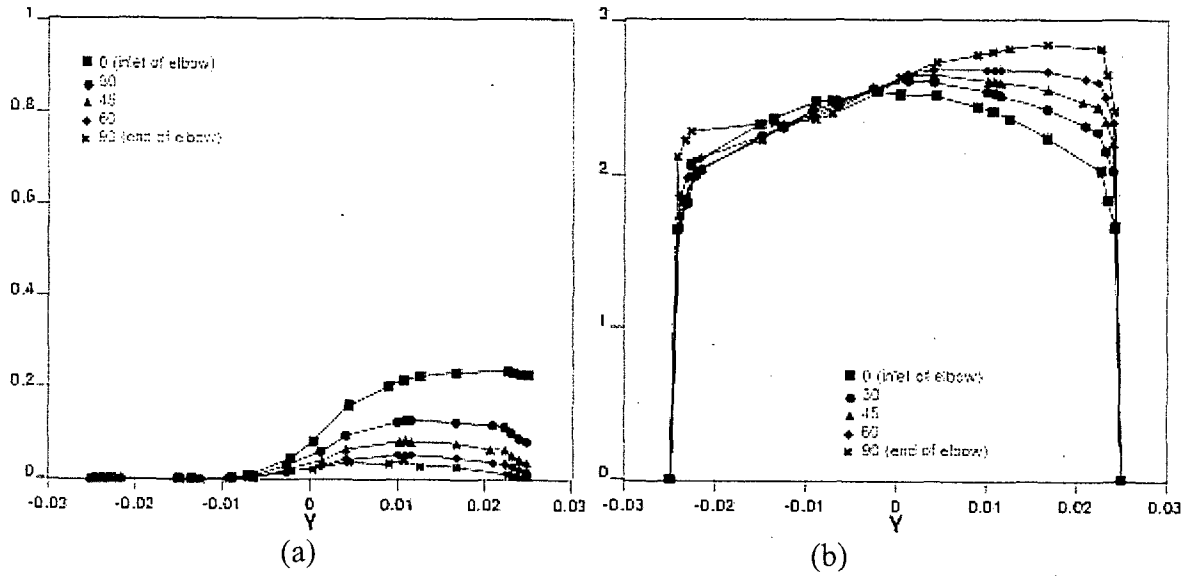


Figure 7.34. Lateral profiles of: (a) void fraction, (b) gas velocity, along the vertical diameter at several sections the 90° elbow of a horizontal tube for Run 2 of the experiments reported by Kim et al. [2005].

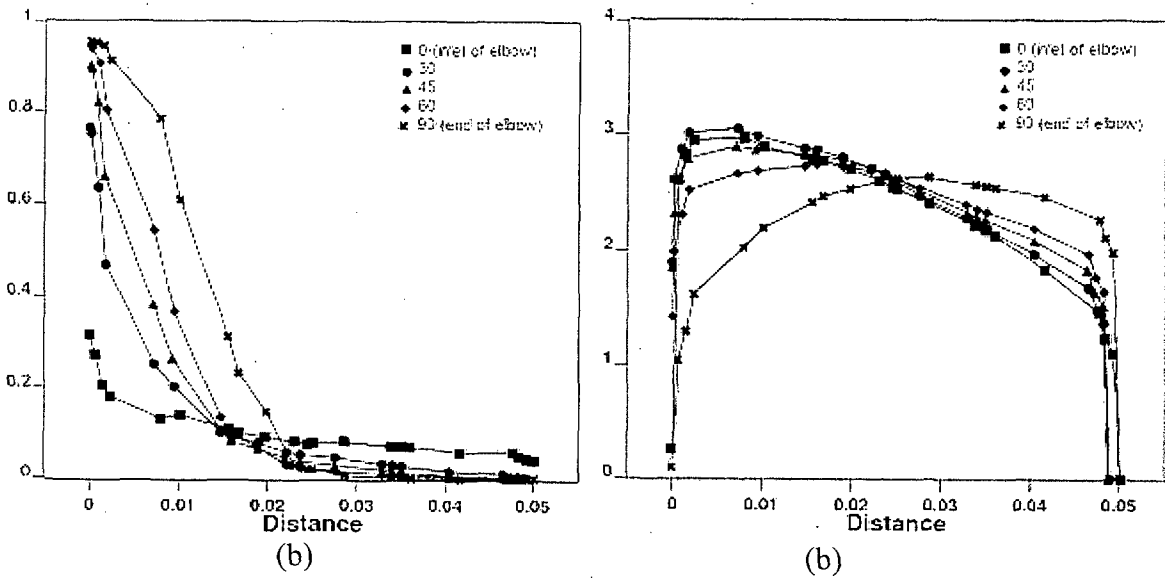


Figure 7.35. Lateral profiles of: (a) void fraction, (b) gas velocity, along the horizontal diameter at several sections along the 90° elbow of a horizontal tube for Run 2 of the experiments reported by Kim et al. [2005].

It is interesting to notice that since the flow velocity in Run 1 was relatively small (Figure 7.22, $j_f=0.56$ m/s) the void fraction at the location corresponding to the exit from the elbow started to return to fully developed conditions. On the other hand, due to a higher velocity in Run 2 ($j_f=1.65$ m/s), the effect of the elbow can still be seen in Figure 7.35.

Finally, the results on Figure 7.36 show a comparison between selected two-phase flow parameters at half-radius from the centerline and the results obtained at the centerline. This Figure presents the vertical profiles of void fraction and gas velocity at the location corresponding to Port 4 in Run 2 of the experiments.

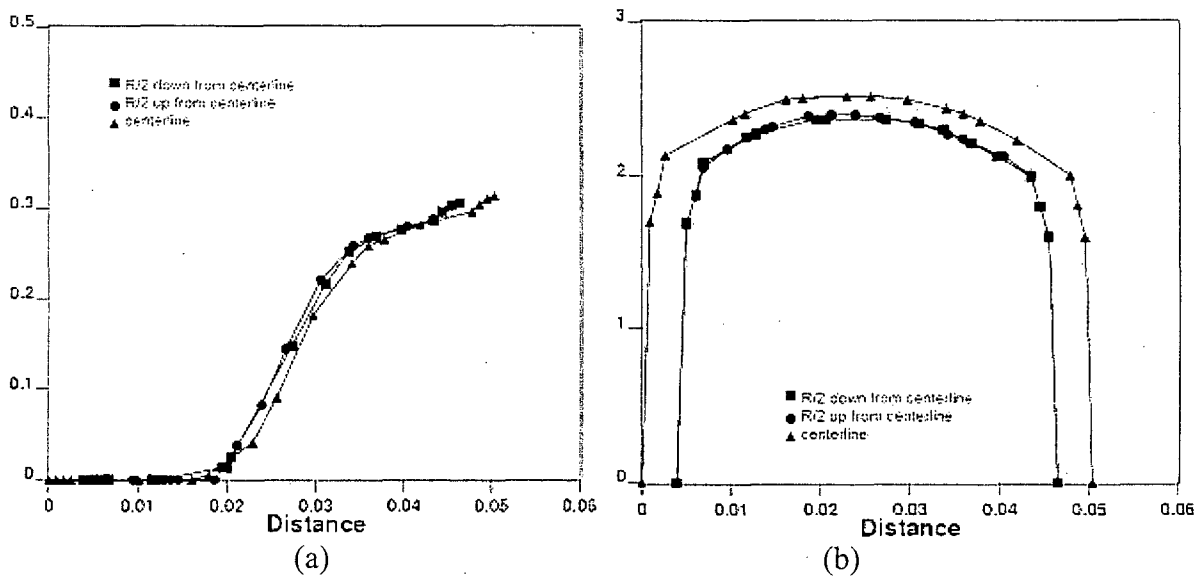


Figure 7.36. Vertical profiles of: (a) void fraction, (b) gas velocity, at half-radius from the centerline and at the centerline, along the vertical diameter at an axial location corresponding to Port 4 in Run 2 of the experiments by Kim et al., [2005].

7.3 Shape Evolution of Large Deformable Bubbles

The proposed interface tracking method based on a coupled Level-Set/Finite-Volume computational algorithm has been implemented in the NPHASE code and extensively tested and validated. The issues of particular interest included: the influence of fluids physical properties (density viscosity, surface tension), the effects of channel orientation and of bubble/channel size, and flows in complicated geometries (where the use of unstructured grids is required). Selected results of predictions are shown below.

7.3.1. Oscillating U-tube Manometer

The U-tube manometer is a very useful, both theoretically and practically, case to test several basis features of the level set method. A physical formulation of the problem is presented on Figure 7.37. For testing purposes, although the problem could be treated as one dimensional, a two dimensional grid was constructed. The straightforward advantage of the test is that there is analytical solution to this transient problem.

Two major issues were examined: density ratio and interface resolution on the grid. From the analytical view point, the manometer can be treated as a one dimensional problem, with x being the coordinate along the manometer. Then, for a constant manometer cross section area, no friction on the walls and using the incompressibility assumption (the velocity v is the same in each cross section), the general, position dependent momentum equation is

$$\rho \frac{\partial v}{\partial t} = -\frac{\partial p}{\partial x} + \rho g_x \quad (7.1)$$

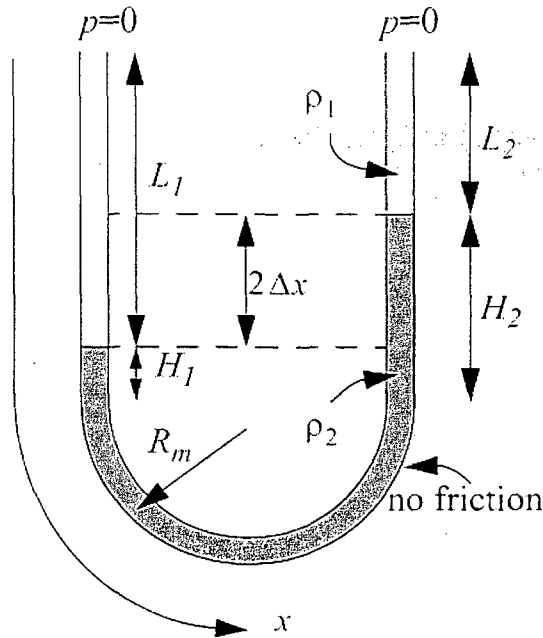


Figure 7.37. Oscillating U-tube manometer.

Integrating Eq.(7.1) over the manometer length, with the same, constant, values of the pressure at both boundaries, gives

$$M_{tot}'' \frac{d^2(\Delta x)}{dt^2} = -2g(\rho_2 - \rho_1)\Delta x \quad (7.2)$$

where M_{tot}'' is the total mass per unit cross-section area of the manometer (that remains unchanged during the transient, since the same amount of fluid enters the manometer through one pressure boundary as the amount that leaves through the other boundary).

The solution of Eq.(7.2) can be expressed as

$$\Delta x(t) = -A \cos(2\pi ft) \quad (7.3)$$

where A is the amplitude and f is the frequency of oscillations.

From geometrical considerations, the following expression can be readily derived

$$f = \frac{1}{2\pi} \left[\frac{2g \left(1 - \frac{\rho_1}{\rho_2} \right)}{\pi R_m + H_1 + H_2 + \frac{\rho_1}{\rho_2} (L_1 + L_2)} \right]^{0.5} \quad (7.4)$$

The solution for the velocity is

$$v(t) = \frac{d[\Delta x(t)]}{dt} = 2\pi f A \sin(2\pi f t) \quad (7.5)$$

The numerical simulations based on the present coupled level-set/NPHASE model have been performed using a regular 2-D grid with several nodes across the manometer. The level set function (actually, there are two functions, because there are two separate interfaces) was defined as a linear function of position along the vertical section of the manometer.

A comparison between the results of numerical simulations and the analytical solution given by Eq.(7.5) is shown in Figure 7.38 for the liquid-to-gas quality ratio of 1000. To capture the correct amplitude of self sustained oscillations (since there is no friction at the wall), the time step used in the calculations had to be sufficiently small.

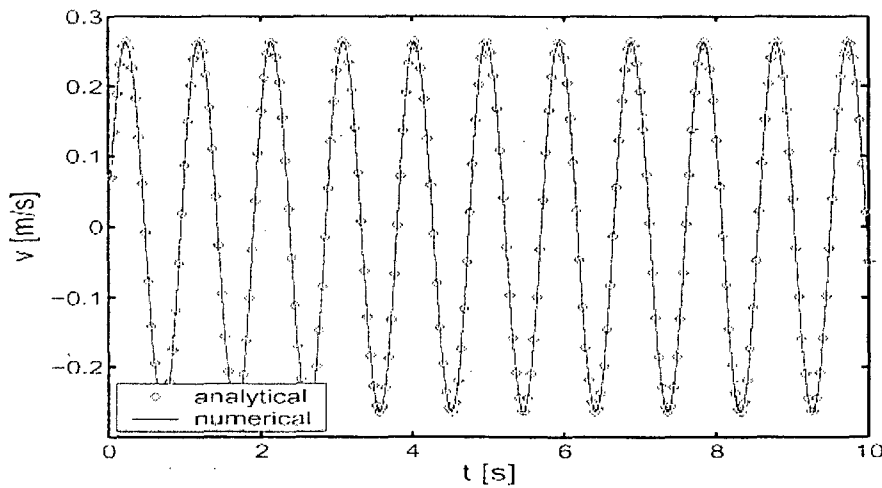


Figure 7.38. Velocity oscillations.

Figure 7.39 presents the simulations aimed at testing the effect of the magnitude of oscillations on the predicted temporal response. Two cases for two different initial amplitudes were compared against each other. It was done in such a way that for both cases the total length, $L_1 + L_2$ (see Figure 7.38), was the same. Eq.(7.5) implies that the frequencies of oscillations should also be the same if only the density ratio remains unchanged. The results of simulations shown in Figure 5 confirm the theoretical predictions very well.

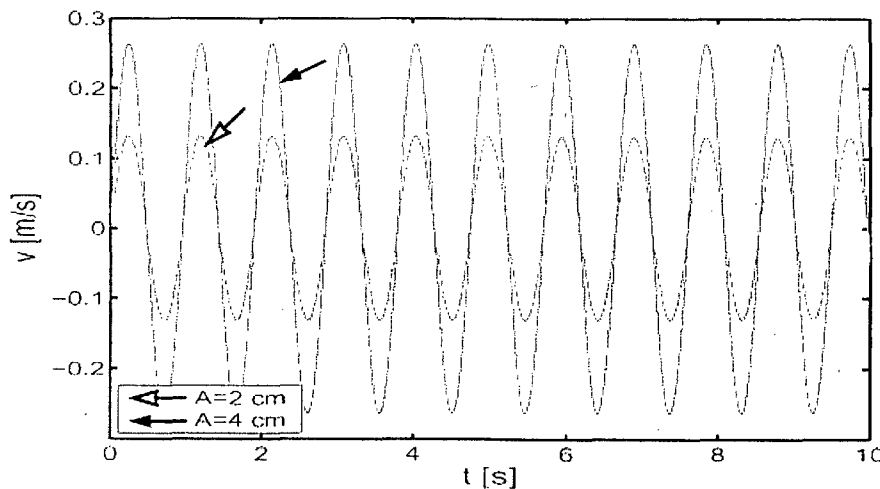


Figure 7.39. Amplitude test.

Figure 7.40 illustrates the effect of fluid densities, one simulating the liquid, the other - the surrounding gas (at atmospheric pressure). This result shows that, indeed, for the same initial amplitude and the same density ratio, the solutions are identical.

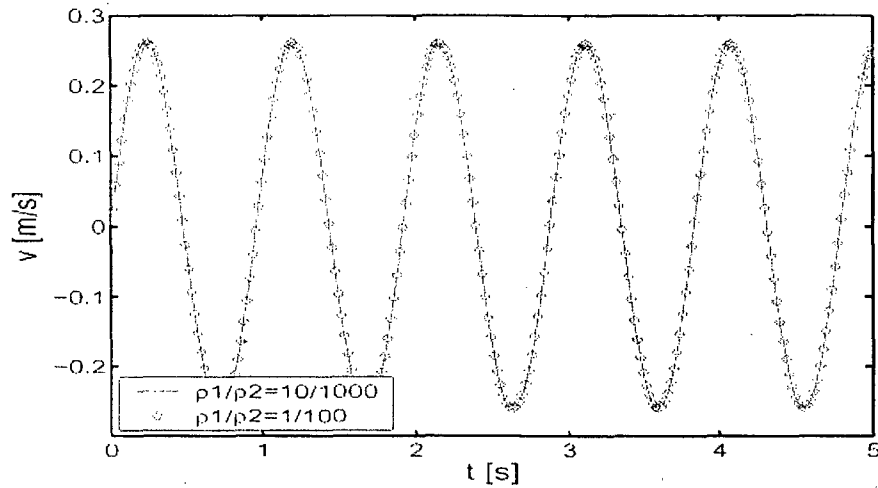


Figure 7.40. Density ratio test.

The last test is also important for another reason. Since all the equations solved are in a dimensional form, what matters is not only the density ratio but also the absolute difference between the two densities.

The effect of varying density ratio has also been tested, showing that the method is stable even for $\frac{\rho_1}{\rho_2} = 10^{-5}$.

An important issue that may create an instability across the interface was also tested. The result shown in Figure 7.41 indicates that the instability occurs most likely at the interface region and propagates more easily into the gas region. In particular, it has been noticed that this effect is negligible when the interface region is smoothed over at least four nodes. Moreover, the magnitude of this instability appears independent of the number of nodes per unit length of the manometer used in the simulations.

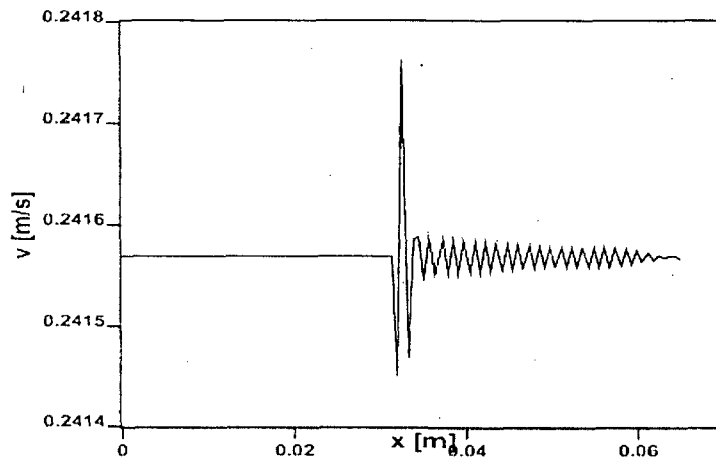


Figure 7.41. Velocity instability across the interface.

7.3.2. Free Interface in Inclined and Vertical Channels

In this test, two situations were compared, in which a stagnant liquid was partially filling either a vertical or an inclined tank. As shown in Figure 7.42, significant numerically-induced parasitic velocities appeared in the case of inclined tank, whereas the vertical case was only slightly affected by such numerically-generated (wall boundary related) flow patterns.

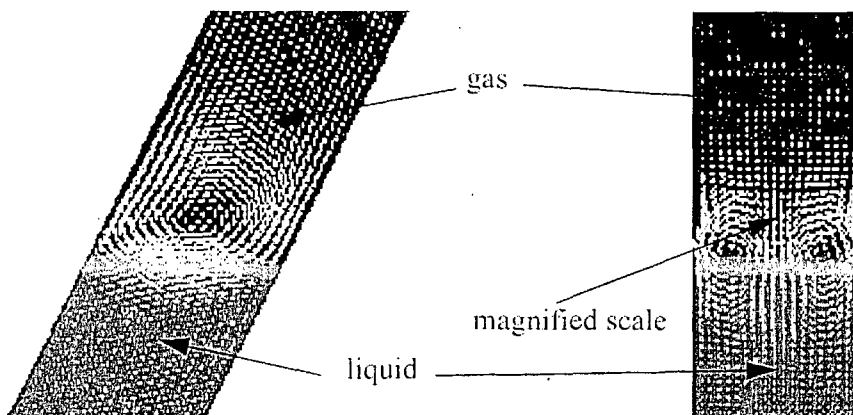


Figure 7.42. Parasitic currents - order of magnitude: inclined, $O(10^{-2})$; vertical, $O(10^{-7})$.

For the inclined channel, the effect of parasitic velocities is due to the interface vs. gravity force orientation. Since, in general, the grid for this case is not aligned with the interface (as it is for the vertical case), the unwanted currents arise due to numerical discretization. For both cases, the finer the grid (or higher order numerical approximation) the smaller the effect of parasitic currents. Furthermore, this effect all but diminishes for flow situations, as illustrated in Figure 7.43.

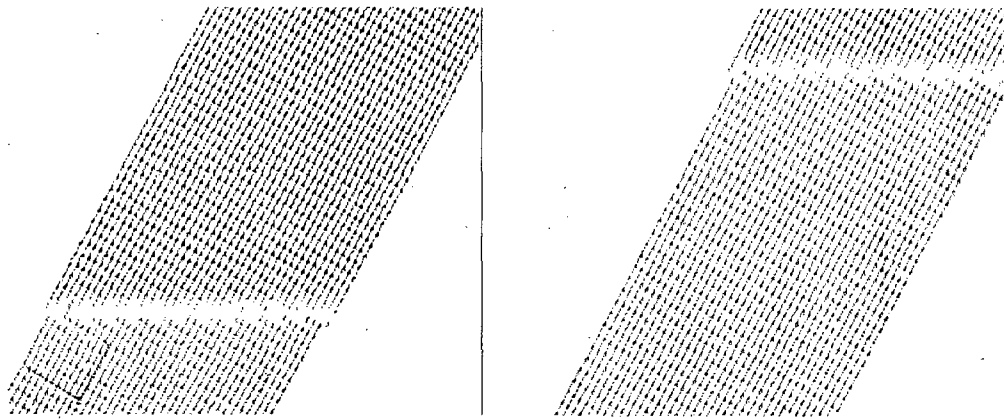


Figure 7.43. Liquid rise in inclined channel - uniform velocity field.

7.3.3. Gas Bubble at Zero Gravity

As described before, the surface tension effect is introduced as a body force into the momentum equation. Thus, setting gravity to zero allows to examine the influence of this force on the accuracy of numerical solutions. In the present case, a single bubble was placed in a cubic box filled with a liquid. Similarly to the previous test case, parasitic currents occurred again, although the pressure jump across the interface was predicted correctly, as shown in Figure 7.44.

Again, the reason for the parasitic velocities is the interface/grid/force orientation, resulting in a systematic approximation error. As before, this effect can be overcome by applying a fine enough grid. Additionally, parasitic velocities diminish with increasing fluid viscosity. This, in turn, is related to increasing flow resistance.

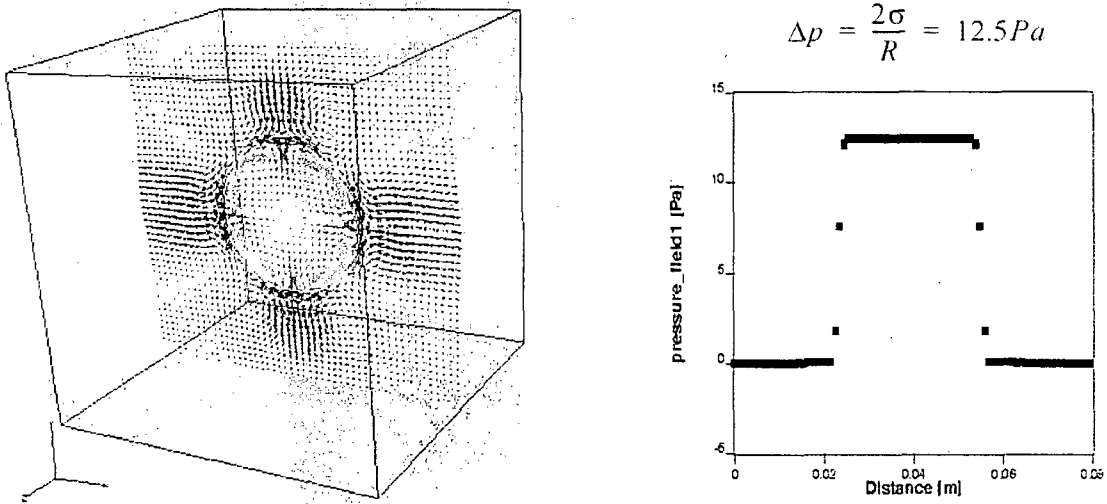
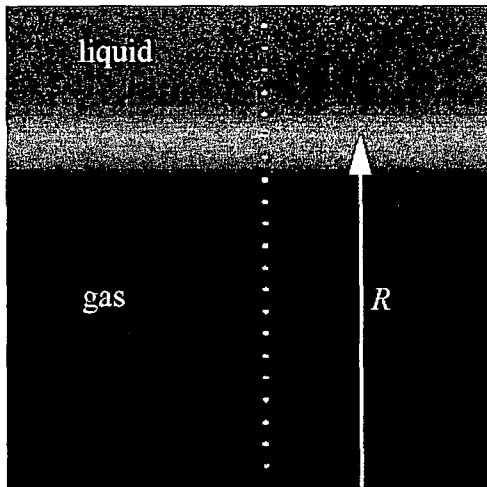


Figure 7.44. Surface tension effect and parasitic velocities.

In order to clearly see the effect of grid/interface orientation, the cylindrical coordinates were used as well. Specifically, as shown in Figure 7.45, a long smooth cylindrical bubble was positioned at the center of a pipe filled with a liquid. As can be seen, since in this case the interface was aligned with the grid (uniform squares), parasitic velocities did not appear (their magnitude was practically of the numerical zero range).



$$\Delta p = \frac{\sigma}{R} = 6.25 Pa$$

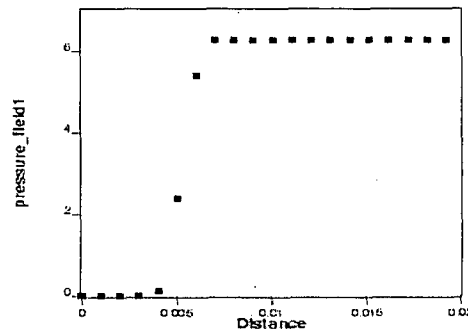


Figure 7.45. Surface tension effect - parasitic velocities do not appear.

7.3.4. Motion of Cap Bubble in Vertical Tube

Simulations have been performed for a cap bubble flowing in a quiescent liquid. The conditions are similar to those used by Collins [1965], and correspond to theoretical “planar” bubbles. A moving system of coordinates has been used in such a way that the bubble would assume a fixed position if its terminal rise velocity was equal to the coordinate system velocity. The results for a transient flow are shown in Figure 7.46.

The calculated bubble velocity was approximately 15 cm/s, versus 16 cm/s for the theoretical value. The theoretical result is an approximation only, both due to the necessary model simplifications (such as: steady-state flow, axisymmetric, etc.), and also because the bubble rise velocity is determined based on the curvature at the bubble tip, which experiences variations. Once the symmetry was lost approximately after 0.6 s, the bubble started oscillating. This result confirms qualitatively the experimental evidence that cap bubbles normally do not assume steady state flow conditions.

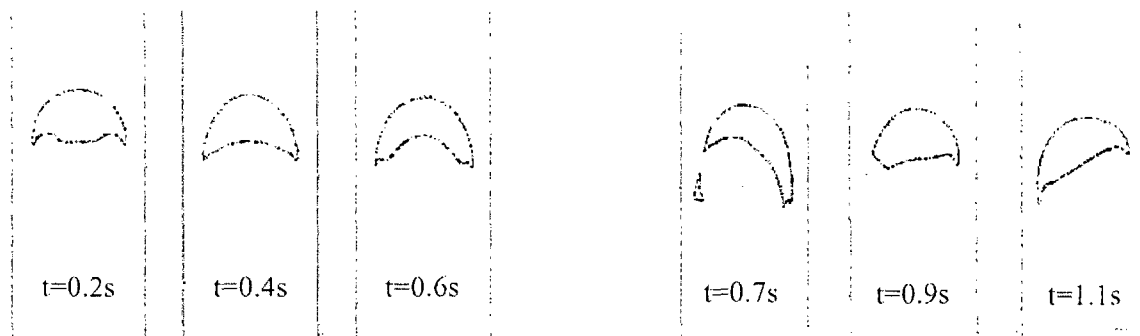


Figure 7.46. Transient cap bubble flow (2-D).

7.3.5. Influence of Liquid Viscosity

The viscosity of the liquid surrounding a gas bubble affects not only the bubble rise velocity, but also may determine the bubble flow regime. Figures 7.47 and 7.48 present two initially identical air bubbles submerged in two different fluids (glycerin and water).

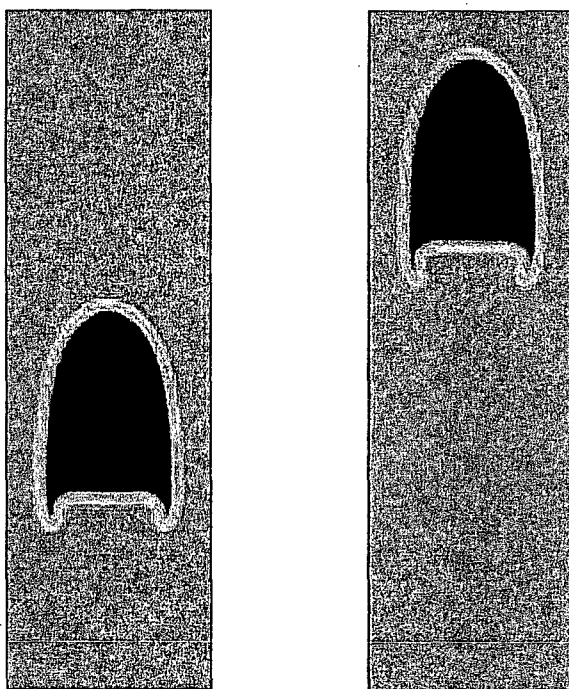


Figure 7.47. Air bubble flow in glycerin.

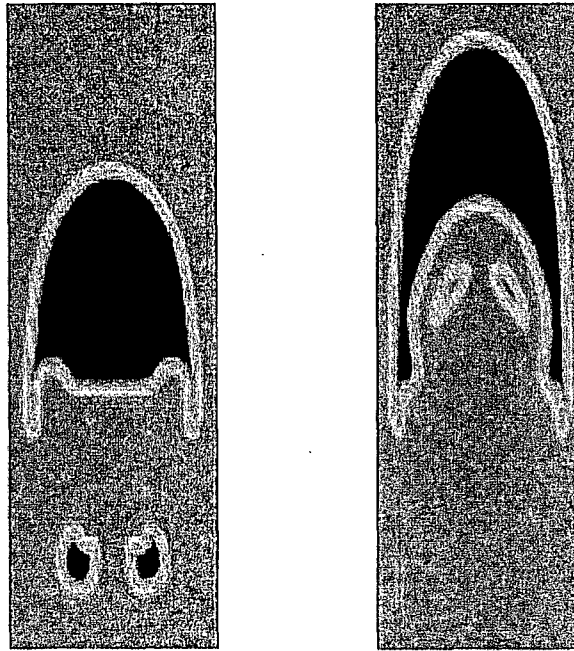


Figure 7.48. Air bubble flow in water.

As can be readily seen, the less viscous the liquid, the more unsteady the flow, so that the bubble may experience breakup more easily. In both cases, the initial velocity was set to zero. Once the transient flow begins, a liquid jet forms at the bottom of the bubble and tries to penetrate it. Since the flow resistance is higher for the viscous case, this jet is much weaker than for the low viscosity liquid.

7.3.6. Effect of Surface Tension

The influence of surface tension on the stability of Taylor bubble shape was examined in this case. The results are shown in Figure 7.49.

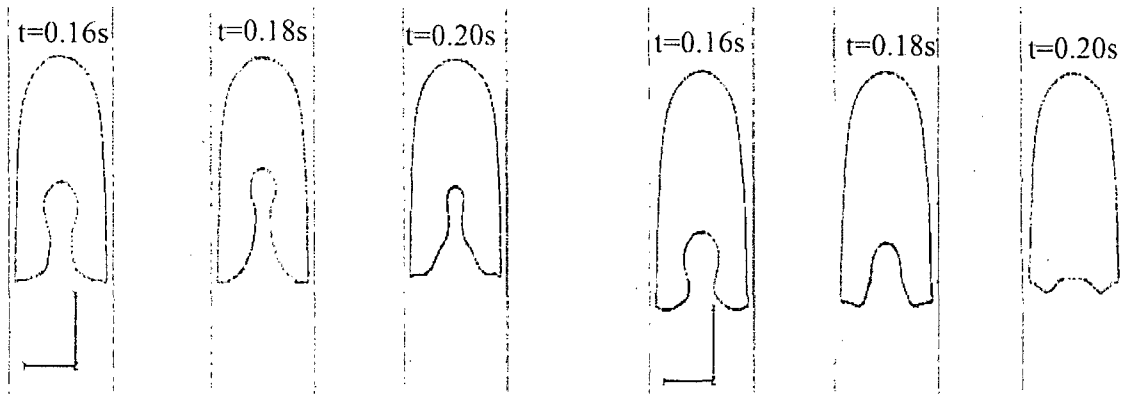


Figure 7.49. Air - water system (density and viscosity at normal conditions): (a) $\sigma = 0.07$ N/m, (b) $\sigma = 0.14$ N/m.

As expected, surface tension has a stabilizing effect on Taylor bubble shape, so that the shape of bubble cap is similar for both cases. As in the previous example, the initial velocity field is set to zero, and the liquid jet penetrates the bubble more easily for the lower surface tension case. These are two-dimensional simulations, and it should be noted that if the same cross section shape corresponded to a three dimensional bubble, the effect of curvature (and thus surface tension), would be stronger (approximately by a factor of two near the nearly-spherical cap).

7.3.7. Effect of Channel Inclination Angle on Maximum Rise Velocity

It is well known from experimental data that in the case of a large bubble flowing in a confined channel, there is a certain inclination angle, for which the bubble rise velocity reaches a maximum. In order to show that the present Level-Set/NPHASE based multidimensional model can properly predict this interesting phenomenon, the results of three dimensional simulations have been compared against the experimental evidence of

Shosho and Ryan [2001]. The computation model is illustrated in Figure 7.50. Since the conditions used in the simulations were slightly simplified compared to those used in the experiments, the objective of the comparison was mainly to verify the varying velocity trend and the range of velocity change. Specifically, the predicted bubble velocity in the 80o-inclined channel (0.197 m/s) exceeded that in the vertical channel (0.18 m/s) by 9.5%, whereas the corresponding experimental result for the same inclination angles was 10.2%.

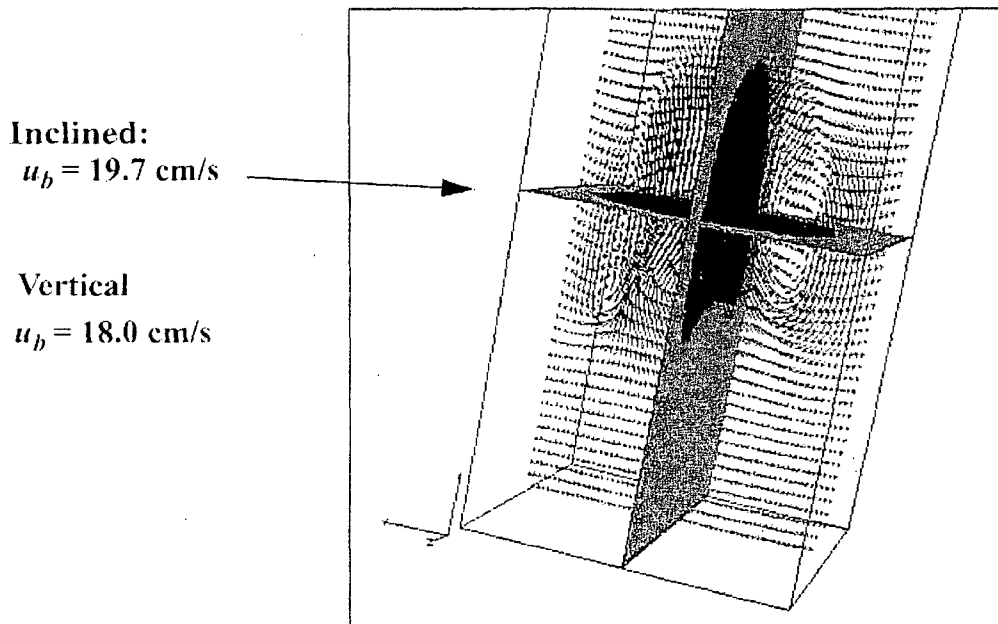


Figure 7.50. Air bubble flow in rectangular channel (80° inclination angle) filled with glycerin.

7.3.8. Large bubble rising in Converging Nozzle

In order to demonstrate the potential of the overall computational model combining the Level-Set method and the NPHASE finite volume CFD solver, a simulation was performed of large bubble entering a converging section of a conduit. In this case, a very important

issue is the use of unstructured grids to discretize channel geometry. The geometry of the grid used in the present simulations is shown in Figure 7.51(a). The results of predictions by the present model, including both the instantaneous bubble shape and the corresponding velocity vectors at a certain location along the nozzle, are shown in Figure 7.51(b). In both cases, the blue color shows the velocity vectors that correspond to the negative values of the level set function (inside the bubble), and the red-colored velocity vectors refer to the positive values of this function. As it can be seen, that bubble side interface quickly aligns with the wall orientation.

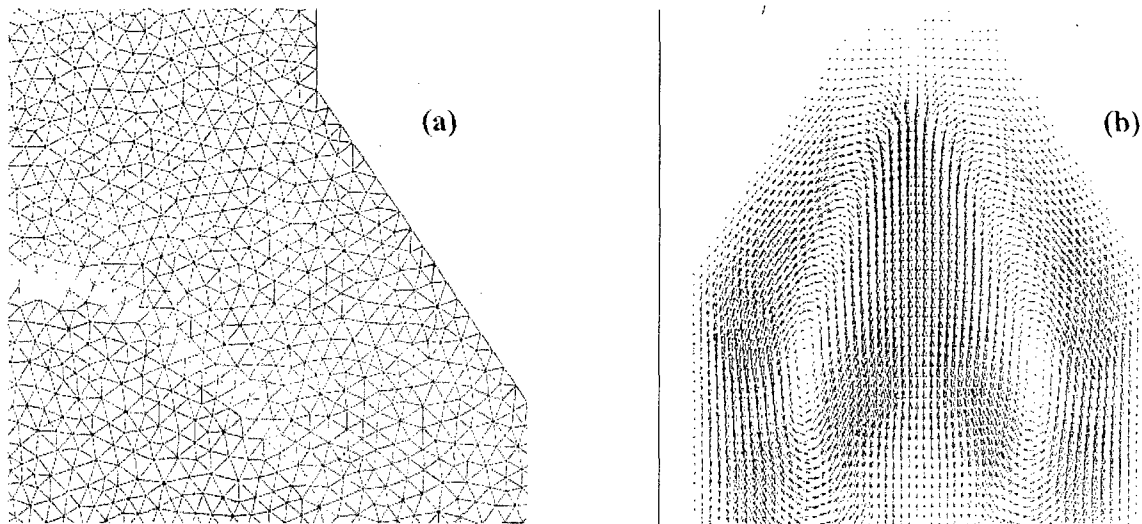
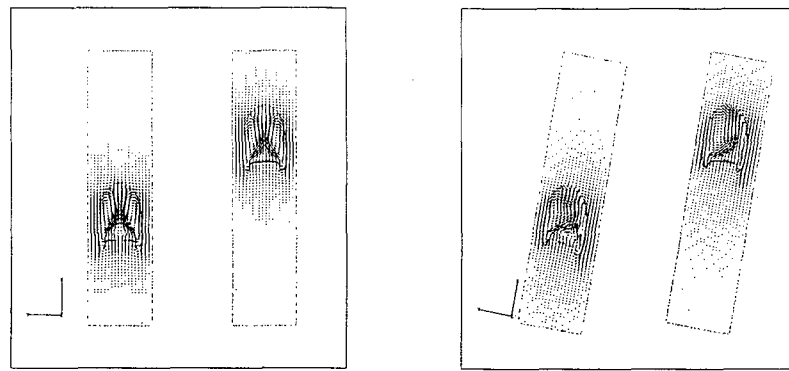


Figure 7.51. Bubble rising in a converging channel (velocity vectors with zero level set and unstructured grid colored by the density field): (a) unstructured grid, (b) bubble shape and velocity vectors.

7.3.9. Large Bubble Moving along Inclined Wall

Typical results of the testing and applications of the present model are shown in Figure 7.52. As can be seen, the calculated bubble velocity for the slightly inclined (10° from the vertical) channel case is higher by about 5% compared to the vertical channel case. Such increase is in agreement with experimental data [Shosho and Ryan [2001], thus confirming the consistency and accuracy of the current coupled level-set/finite volume numerical method.



(a) $u_b=14.25$

(b) $u_b=15.02$

Figure 7.52. Effect of tube inclination angle on the velocity of a large bubble: (a) vertical tube, (b) tube inclined 10° from the vertical.

Figures 7.53 and 7.54 shows the results of test calculations for a rigid section of the gas/liquid interface, moving along the solid surface at a prescribed angle of 45° . The problem was formulated in such a way that, instead of explicitly introducing a boundary condition associated with the interface, the effect of the interface (in particular, of its inclination angle) was accounted for by introducing an external force normal to the interface.

The main purpose of the calculations was to check if the velocity vectors around the interface become indeed parallel to the interface, as well as to assess the convergence and stability of the overall solver concerning the velocity field calculations in the entire computational domain. As can be seen, both the calculated absolute velocity and the velocity relative to the interface are consistent with the boundary conditions imposed by the geometry of the moving rigid interface, thus confirming the applicability of the external force concept.

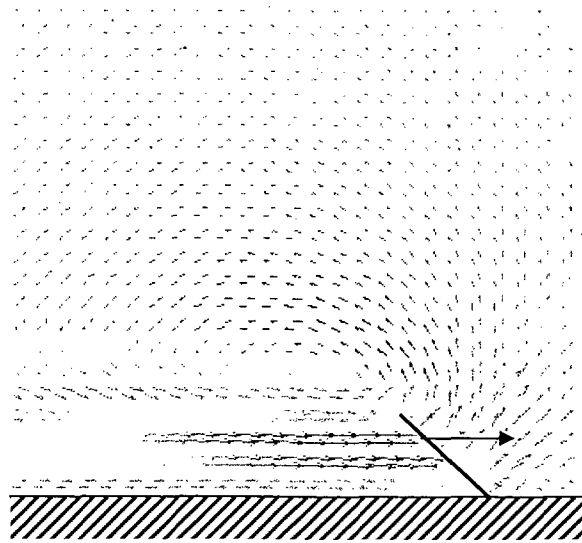


Figure 7.53. Fluid velocity induced by a force applied near the wall and perpendicular to a moving rigid surface simulating gas/liquid interface near the wall.

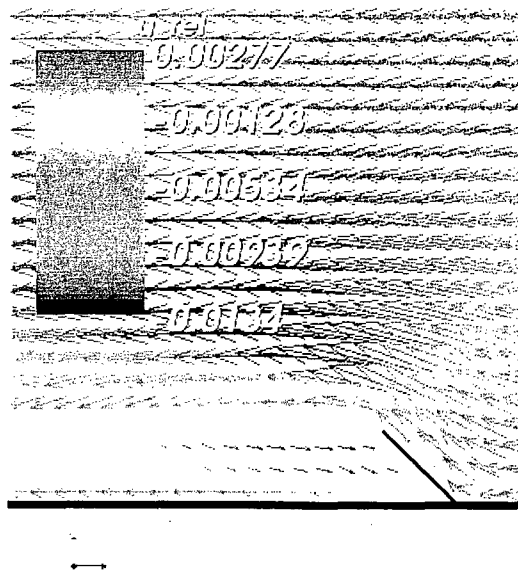


Figure 7.54. Fluid-to-interface relative velocity induced by the external force (same conditions as in Figure 7.53).

Finally, typical results of the coupled Level-Set/NPHASE simulations for a gravity-driven bubble moving along an inclined channel are given in Figures 7.55 and 7.56. The shape evolution of the bubble accelerating along the wall is shown in Figure 7.55, whereas the steady bubble motion at/near fully-developed flow conditions is presented in Figure 7.56. Both results clearly indicate that the proposed external force concept allows one to model the shape evolution and motion of large bubbles in contact with solid walls.

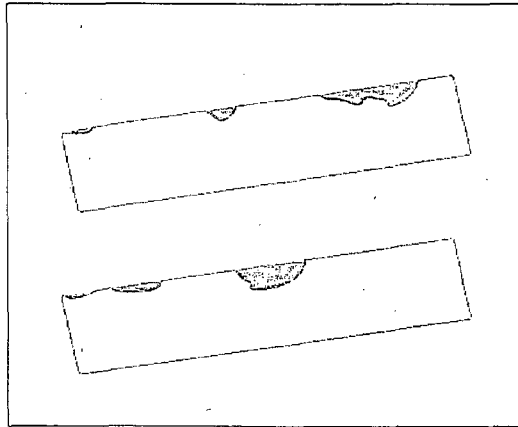


Figure 7.55. The shape evolution of a large deformable bubble accelerating along the wall of a 10° inclined channel, predicted by the NPHASE code.

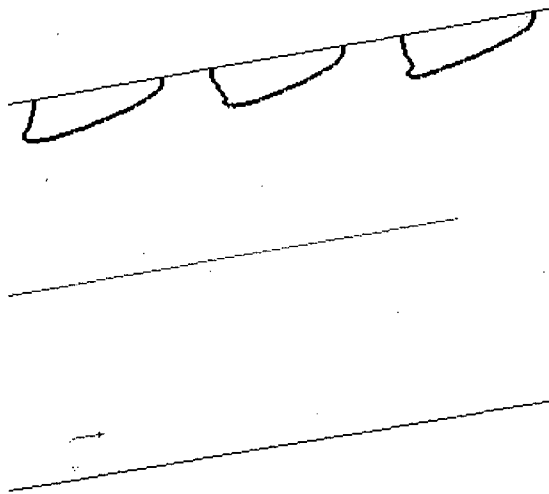


Figure 7.56. The motion of a bubble underneath a solid surface.

8. CONCLUSIONS AND RECOMMENDATIONS FOR FUTURE WORK

The purpose of this report was to document recent developments concerning the development of mechanistic models of two- and multiphase flow and the implementation of those models in the NPHASE Computational Multiphase Fluid Dynamics (CMFD) code.

The modeling issues can be divided into two major groups. The first group of tasks was concerned with the multifield modeling concept and its application to gas(vapor)/liquid two-phase flows. Details of model development have been discussed in Chapters 2 through 5, and the results of model testing and validation have been presented in Chapter 7 (Sections 7.1 and 7.2). Among the various novel aspects of the present work, the following specific accomplishments can be identified:

- The formulation and analysis of a consistent multifield framework for dispersed two- and multiphase flows.
- The formulation of a consistent mechanistic concept for the turbulence-induced bubble/liquid (or particle/liquid) interfacial force.
- The derivation of a new mechanistic multidimensional model of gas/liquid two-phase flows in horizontal conduits.
- The implementation of the new models of two-phase flow in the NPHASE code.
- The demonstration of the consistency and accuracy of the overall multifield modeling approach developed for, and encoded in, the NPHASE code, including model testing and validation against experimental data.

The other group of issues deals with a new approach used to directly model gas/liquid interfaces in two-phase flows containing large deformable bubbles. A detailed model derivation has been shown in Chapter 6 and the numerical results of testing and validation of

the new model has been given in Chapter 7 (Section 7.3). The novel aspects of the work include the following:

- The development of a general, computationally-efficient model for the simulation of time-dependent shape of gas/liquid interfaces in conduits of various orientations.
- The development of a new concept for the modeling of the effect of solid walls on shape evolution and motion of large bubbles flowing underneath the surface of inclined channels.
- The coupling of a modified/enhanced level-set method of interface tracking with the numerical solver of the NPHASE code.
- The application of the coupled level-set/NPHASE solver to simulate a broad range of situations concerning the motion of large deformable bubbles.
- The demonstration of the consistency, numerical efficiency and robustness, and physical accuracy of the proposed approach.

Whereas the results presented in this report clearly show the potential of multidimensional models of two-phase flow, and of the CMFD method for application in the analysis of nuclear reactor thermal-hydraulics and safety, more work is clearly needed to fully demonstrate the advantages and range of possible future applications of the NPHASE-based computer simulations of two-phase fluid flow and heat transfer in nuclear reactor components and systems. In particular, the following directions of future work are recommended:

- Capitalize on the newly acquired capability of the NPHASE code to simulate the shape and motion of large deformable bubbles to establish a 'virtual' data base for the development of mechanistic multidimensional models of two-phase flows encountered in

nuclear reactor systems. Examples include the modeling of churn and slug flows, and of the mechanisms governing flow regime transition.

- Furthermore, use and expand the ability to model the effect of the solid wall/bubble interaction on flow conditions, to improve the understanding of transients in complex geometries of reactor systems.
- Continue the development of consistent mechanistic multifield models of gas/liquid two-phase flows, including the ability to predict interactions between bubbles of different sizes (coalescence and breakup) and the entrainment and deposition of liquid droplet in annular flows, for various conduit orientations and geometries.
- Enhance the capabilities of the NPHASE code for application to massive three-dimensional simulations of transient two- and multiphase flows. Examples of specific issues include: solver parallelization and the development of faster and more robust solution algorithms for the combined equations governing the conservation of mass, momentum and energy of the individual flow components.
- Develop a broad and consistent data base for the validation of new two-phase flow models and of the NPHASE-based CMFD solver as a whole.

References

Anglart, H., Nylund, O., Kurul, N. and Podowski, M.Z., "CFD Simulation of Flow and Phase Distribution in Fuel Assemblies with Spacers", *Nuclear Science and Engineering*, 177 pp.215-228 (1997).

Anglart, H. and Podowski, M.Z., *Nuclear Science & Engineering*, V.140, No.2 (2002).

Antal, S.P., Lahey, R.T., Jr. and Flaherty, J.E., *Int. J. Multiphase Flow*, 17(5) (1991) 625-652.

Antal, S.P., Kunz, R., Ettore, S. and Podowski, M.Z., "Development of a Next Generation Computer Code for the Prediction of Multicomponent Multiphase Flows", Proc. International Meeting on Trends in Numerical and Physical Modeling for Industrial Multiphase Flows, Cargese, France, 2000.

Brackbill, J.U., Kothe, D.B., Zemach, C., "A continuum method for modeling surface tension", *Journal of Computational Physics*, Vol.100, 335, 1992

Chen, L., Garimella, S. V., Reizes, J. A., Leonardi, E., "The development of a bubble rising in a viscous liquid", *J. Fluid Mech.*, vol. 387, 61-96, 1999.

Collins, R., "A simple model of the plane gas bubble in a finite liquid", *J. Fluid Mech.*, vol. 22, part4, 763-771, 1965.

Couet, B., Strumolo, G. S., "The effects of surface tension and tube inclination on a two-dimensional rising bubble", *J. Fluid Mech.*, Vol. 184, 1-14, 1987.

DeBisschop, K., Miksis, M., Eckmann, D., "Bubble rising in an inclined channel", *Physics of Fluids*, vol. 14, No. 1, 93-106, 2002.

Drew, D.A. and Passman, S.L., "Theory of Multicomponent Fluids" Springer-Verlag, NY (1998).

"FIELDVIEW 6 Reference Manual", Intelligent Light, 1999.

"Gridgen User Manual", Version 13.3, Pointwise, 1999.

"Gridpro User Manual", Program Development Corp., 1998 22.

Ishii, M. and Zuber, N., "Relative motion and interfacial drag coefficient in dispersed two-phase flow of bubbles, drops and particles", *AIChE J.*, 25 pp. 843-855 (1979).

Kim, S., Talley, J. and Callender, K., "Data Report for Slug Flow in Air/Water Horizontal Two-Phase Flow with 90-degree Elbow, UMR/NE-TFTL-05-03 (2005).

Kurul, N. and Podowski, M.Z., "Grid Generation for the Analysis of Dispersed-Phase Motion in Two-Phase Flows", in *Numerical Grid Generation in Computational Fluid Mechanics*, Pineridge Press (1988).

Lakehal, D., Meier, M., Fulgosi, M., "Interface tracking towards the direct simulation of heat and mass transfer in multiphase flows", *Int. J. of Heat and Fluid Flow*, 23, p. 242-257, 2002.

Maneri, C. C., Zuber N., "An Experimental Study of Plane Bubbles Rising at Inclination", *Int. J. Multiphase Flow*, 1, 623, 1974.

Nickens, H. V., Yannitell, D. W., "The Effects of Surface Tension and Viscosity on the Rise Velocity of a Large Gas Bubble in a Closed, Vertical Liquid-Filled Tube", *Int. J. Multiphase Flow*, vol. 13, No. 1, 57-69, 1987.

Podowski, M.Z., "Understanding Multiphase Flow and Heat Transfer; Perception, Reality, Future Needs", *Archives of Thermodynamics*, 26, 3 (2005), pp.1-18.

M.Z. Podowski, "On the Mechanistic Modeling of Interfacial Phenomena in Gas/Liquid Two-Phase Flows", *Proc. 6th International Conference on Multiphase Flow*, Leipzig, Germany (2007).

Rhie, C.M., Chow, W.L. "Numerical Study of the Turbulence Flow Past an Airfoil with Trailing Edge Separation," *AIAA Journal*, Vol. 21, p. 1527, 1983.

Rudman, M., "A Volume-Tracking Method for Incompressible Multifluid Flows with Large Density Variations", *Int. J. Numer. Meth. Fluids*, 28, 357-378, 1998.

Sato, Y. and Sekoguchi, K., "Liquid Velocity Distribution in Two-Phase Bubble Flow," *Int. J. Multiphase Flow*, Vol 2, 79-95, 1975

Serizawa, A., Kataoka, I. and Michiyoshi, I. *Int. J. Multiphase Flow*, 2(3), 221-260, 1975.

Shosho, C. E., Ryan, M.E., "An experimental study of the motion of ong bubbles in inclined

tubes”, Chem. Eng. Sci., 56, 2191-2204, 2001.

Sussman, M., Almgren, A.S, Bell, J.B., Colella, P., Howell, L.H., Welcome, M.L. “An Adaptive Level Set Approach for Incompressible Two-Phase Flows”, *Journal of Computational Physics*, Vol.148, 81-124,1999.

Sussman, M., Smereka, P., Osher, S.J., “A Level Set Approach for Computing Solutions to Incompressible Two-Phase Flow”, *Journal of Computational Physics*, Vol.114, p. 146, 1994.

Tiwari, P., Antal S.P. and Podowski M.Z., (2003) “On the Modeling of Dispersed Particulate Flows using a Multifield Model”, in Computational Fluid and Solid Mechanics, (Ed.: Bathe, K. J.), 1 (2003) 1160-1165.

Tiwari, P., Antal, S.P. and Podowski, M.Z., "Three-Dimensional Fluid Mechanics of Particulate Two-Phase Flows in U-bend and Helical Conduits", *Physics of Fluids*, 18, 4 pp.1. (2006),

Tselishcheva, E.A., Antal, S.P., Podowski, M.Z. and Marshall, S. “Mechanistic Multidimensional Analysis of Two-Phase Flow in Horizontal Tube with 90° Elbow”, Proc. Int. Congress on Advancements in Nuclear Power Plants, Nice, France (2007).

Valukina, N.V., Kozmenko, B.K. and Kashinskii, O.N., *Inzhenerno-Rizichenskij Zhurnal*, 36, 4 (1979).

Vafaei, S. and Podowski, M.Z., “Analysis of the Relationship between Liquid Droplet Size and Contact Angle”, *Advances in Colloid and Interface Science*, 113, pp. 133-146 (2005).

Van Doormal, J.P., Raithby, G.D., “Enhancements of the SIMPLE Method for Predicting Incompressible Fluid Flows,” *Numerical Heat Transfer*, Vol. 7, pp. 147-163, 1984.

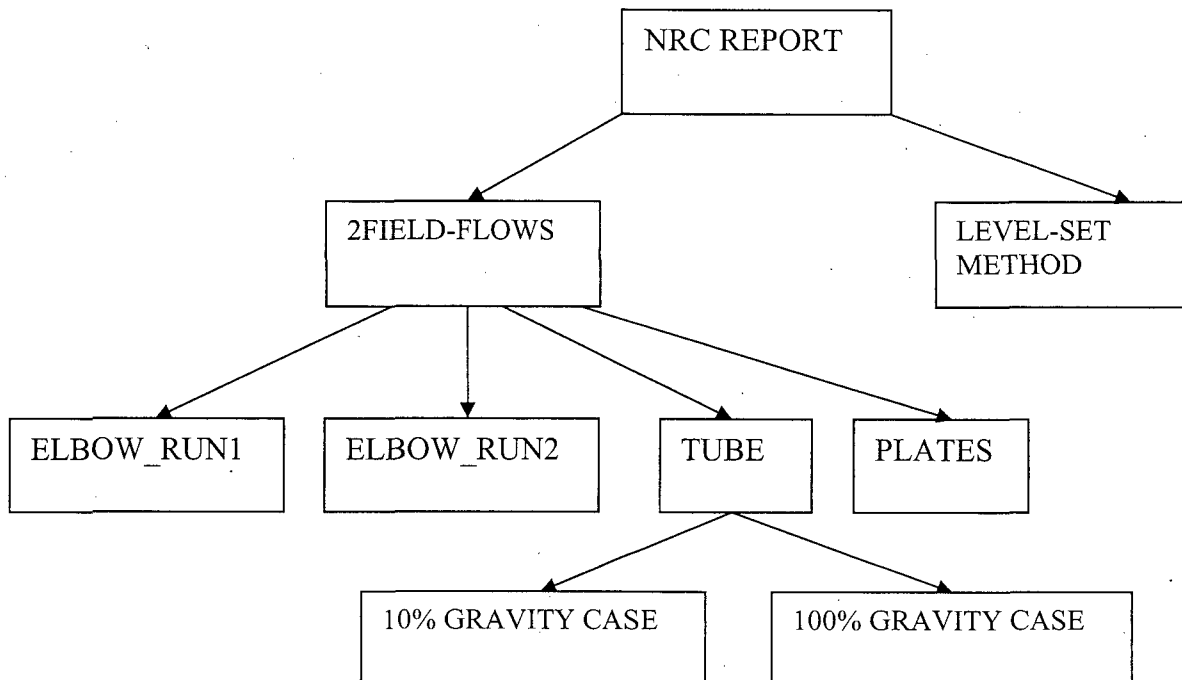
Wang, S.K., Lee, S.J., Jones, O.C. and Lahey, R.T., Jr., *Int. J. Multiphase Flow*, 13(3) (1987) 327-343.

Wierzbicki, B.W., Antal, S.P. and Podowski, M.Z., “Development of Coupled Level-Set/ Unstructured Finite-Volume Computational Model for Interface Tracking in Two-Phase Flows”, Proc. 5th Int. Conf. on Multiphase Flow, ICMF'04, Yokohama, Japan, 2004.

Zukoski, E.E, "Influence of viscosity, surface tension, and inclination angle on motion of long bubbles in closed tubes", *J. Fluid Mech.*, Vol. 25, part4, 821-837, 1966.

Appendix. NPHASE Files

A.1. Directory Structure



A.2. Sample *nphase.dat* file

```
#!SOURCE FILES
#source file 1:user_initialize.c
#source file 2:user_drag.c
#source file 8:printmassflow.c
#source file 3:user_vfdispforce.c

#!JOB CONTROLS
iterations to perform 500
restart file write frequency 20
initialize run with restart file
#overwrite inlet patch boundary conditions on restart
#overwrite pressure patch boundary conditions on restart

#!MODELS
number of fields 2
#cylindrical coordinates
adiabatic flow
turbulent flow high reynolds number k epsilon
turbulence model for each field 1 0
dispersed field shear model 1 1
gravity vector 0 -9.8 0
interfield drag models 1
1 2 0 1.
```

```

interfield non drag models 1
1 2 2 0 0.3
#BOUNDARY CONDITIONS
inlet patch 2 0
0 0. 0.844 1000. 0.76 0.0025 0.0001125
0 0. 0.844 1 0.24 0.0025 0.0001125
pressure profile patch 2 0
0. 1000. 1 .0025 .0001125 0.
0. 1 0 .0025 .0001125 0.

#!PHYSICAL PROPERTIES
constant fluid molecular viscosity 1.e-3 1.e-30
constant fluid density 1000. 1
constant field characteristic diameter 5.e-3 5.e-3
constant fluid surface tension 0.0173 0.0173
constant fluid thermal conductivity 0.1 0.1
constant fluid specific heat at constant pressure 10000 10000
constant fluid reference enthalpy 0 0
constant fluid reference temperature 0 0

#!INITIAL GUESS
initialize u field 0 0
initialize v field 0 0
initialize w field 0.844 0.844
initialize p field 0 0
initialize a field 0.76 0.24
initialize k field 0.0025 0
initialize e field 0.0001125 0
initialize h field 0 0

#!NUMERICAL CONTROL
relaxation factor for u 0.5 0.5
relaxation factor for v 0.5 0.5
relaxation factor for w 0.6 0.6
relaxation factor for p 0.5 0.5
relaxation factor for a 0.3 0.3
relaxation factor for k 0.5 0.5
relaxation factor for e 0.5 0.5
relaxation factor for h 0.5 0.5
false time step for u 0.001 0.001
false time step for v 0.001 0.001
false time step for w 0.001 0.001
false time step for k 1e+30 1e+30
false time step for e 1e+30 1e+30
false time step for a 0.0001

#!SOLVER CONTROL
#coupled block solver for continuity and momentum equations
solver sweeps for u 10 10
solver sweeps for v 10 10
solver sweeps for w 10 10
solver sweeps for p 50 50
solver sweeps for a 10 10
solver sweeps for k 10 10
solver sweeps for e 10 10
solver sweeps for h 10 10

```

A.3. Sample nphase.out file

reading input restart file(s)

finished reading input restart file(s) at iter = 29148

rk	iter	fld	ru	rv	rw	rp	ra	rh
	29148	1	2.794e-06	4.117e-07	1.868e-06	5.039e-03	4.788e-06	
	0.000e+00		7.358e-08	2.366e-06				
	29148	2	2.184e-06	2.983e-06	1.580e-06	5.039e-03	4.780e-06	
	0.000e+00		0.000e+00	0.000e+00				
	29149	1	2.794e-06	4.122e-07	1.868e-06	5.027e-03	4.788e-06	
	0.000e+00		7.354e-08	2.366e-06				
	29149	2	2.185e-06	2.986e-06	1.602e-06	5.027e-03	4.780e-06	
	0.000e+00		0.000e+00	0.000e+00				
	29150	1	2.794e-06	4.120e-07	1.868e-06	5.026e-03	4.788e-06	
	0.000e+00		7.353e-08	2.365e-06				
	29150	2	2.181e-06	2.981e-06	1.581e-06	5.026e-03	4.779e-06	
	0.000e+00		0.000e+00	0.000e+00				

finished writing output restart file(s) at iter = 29150

Number of Inlet Boundaries = 1

Area and Average Pressure for Inlet Boundary ID 0 = 0.00193645 m**2,
1560.72 Pa

Mass Flow for Field 0 Through Inlet Boundary ID 0 = -1.24211 Kg/s

Volumetric Flow for Field 0 Through Inlet Boundary ID 0 = 0 m^3/s

Mass Flow for Field 1 Through Inlet Boundary ID 0 = -0.000392247 Kg/s

Volumetric Flow for Field 1 Through Inlet Boundary ID 0 = 0 m^3/s

Mass Flow for Field 0 Through All Inlet Boundaries = -1.24211 Kg/s

Volumetric Flow for Field 0 Through All Inlet Boundaries = -0.00124211
m^3/s

Mass Flow for Field 1 Through All Inlet Boundaries = -0.000392247 Kg/s

Volumetric Flow for Field 1 Through All Inlet Boundaries = -0.000392247
m^3/s

Number of Pressure Boundaries = 1

Area and Average Pressure for Pressure Boundary ID 0 = 0.00193645 m**2,
P_bar=-1.48053e-15 Pa

Mass Flow and Average Volume Fraction for Field 0 Through Pressure
Boundary ID 0 = 1.21075 Kg/s VF_bar=0.723705

Volumetric Flow for Field 0 Through Pressure Boundary ID 0 = 0.00121075
m^3/s

Mass Flow and Average Volume Fraction for Field 1 Through Pressure
Boundary ID 0 = 0.000423613 Kg/s VF_bar=0.276309

Volumetric Flow for Field 1 Through Pressure Boundary ID 0 = 0.00042361
m^3/s

Mass Flow for Field 0 Through All Pressure Boundaries = 1.21075 Kg/s

Volumetric Flow for Field 0 Through All Pressure Boundaries = 0.00121075
m³/s

Mass Flow for Field 1 Through All Pressure Boundaries = 0.000423613 Kg/s
Volumetric Flow for Field 1 Through All Pressure Boundaries = 0.00042361
m³/s

Volumetric Flow Fraction for Field 1 Beta = 0.25919

Total Volumetric Flow = 0.00163436 m³/s
Volumetric Flow Fraction Beta = 0.25919

Number of Wall Boundaries = 1

Area for Wall Boundary ID 0 = 1.27466 m²
Field 0, Average Wall Shear = 1.93859 n/m² , Summed Force (tau*area)=
2.47106 n, for Wall Boundary ID 0
Field 1, Average Wall Shear = 0.608709 n/m² , Summed Force (tau*area)=
0.775899 n, for Wall Boundary ID 0

A.4. Drag force user-routine *user_drag.c*

```
#include <stdio.h>
#include <math.h>
#include "nphase_struct.h"
#include "definitions.h"
    int user_drag(int idrag)
{
/*-----
    user drag model (model id 0)

    called from:
    forces_mom

    V2.0 baseline code
    initials      comment
    spa

-----*/

    int inode , nstrideb;
    int field_continuous,field_dispersed ;
    int *drag_fielda=var.drag_fielda ;
    int *drag_fielddb=var.drag_fielddb ;

    real *drag_usermultiplier=var.drag_usermultiplier ;
    real *debugvar1=var.debugvar1;
    real term,usermult,cd,eighththirds=8./3. ;
    real gmag,twothirds=2./3. ;
    real urel,vrel,wrel,velrelmag,dia2 ;
    real vf,vf23, vfmin=1.e-3, velrelmin=1.e-3;

// determine continuous and dispersed fields
    field_continuous = DragModelContinuousField(idrag) ;
    field_dispersed  = DragModelDispersedField(idrag) ;
```

```

// determine user multiplier for drag coefficient
usermult= DragModelUserMultiplier(idrag) ;
// field1/field2 small bubble drag model (segregated solver )
if(field_continuous==1 && field_dispersed==2) {
    gmag= sqrt( XGravity*XGravity + YGravity*YGravity +
ZGravity*ZGravity ) ;

        for(inode=0 ; inode<=NumberNodes-1 ; ++inode) {

            urel=UVelocity_InternalNode(inode,field_dispersed)-
UVelocity_InternalNode(inode,field_continuous) ;

            vrel=VVelocity_InternalNode(inode,field_dispersed)-
VVelocity_InternalNode(inode,field_continuous) ;

            wrel=WVelocity_InternalNode(inode,field_dispersed)-
WVelocity_InternalNode(inode,field_continuous) ;

                velrelmag = sqrt( urel*urel + vrel*vrel +
wrel*wrel) ;

                velrelmag = MAX( velrelmag, velrelmin);
vf = MAX( VolumeFraction_InternalNode(inode,field_dispersed) , vfmin ) ;
                cd = 0.4;

term = usermult* 0.75 * cd /
BubbleDiameter_InternalNode(inode,field_dispersed)* vf *
Density_InternalNode(inode,field_continuous)* velrelmag*
NodeVolume_InternalNode(inode);
        DragContinuousField_SegregatedSolver(inode,idrag) = term ;
        DragDispersedField_SegregatedSolver(inode,idrag) = term ;
    }
}
// field1/field3 large bubble drag model (segregated solver )

if(field_continuous==1 && field_dispersed==3) {

    for(inode=0 ; inode<=NumberNodes-1 ; ++inode) {

        urel=UVelocity_InternalNode(inode,field_dispersed)-
UVelocity_InternalNode(inode,field_continuous) ;

        vrel=VVelocity_InternalNode(inode,field_dispersed)-
VVelocity_InternalNode(inode,field_continuous) ;

        wrel=WVelocity_InternalNode(inode,field_dispersed)-
WVelocity_InternalNode(inode,field_continuous) ;

            velrelmag = sqrt( urel*urel + vrel*vrel +
wrel*wrel) ;

            velrelmag = MAX( velrelmag, velrelmin);

vf = MAX( VolumeFraction_InternalNode(inode,field_dispersed) , vfmin ) ;

                cd = 0.4;

```

```

term = usermult* 0.75 * cd /
BubbleDiameter_InternalNode(inode,field_dispersed)* vf *
Density_InternalNode(inode,field_continuous)* velrelmag*
NodeVolume_InternalNode(inode);
    DragContinuousField_SegregatedSolver(inode,idrag) = term ;
    DragDispersedField_SegregatedSolver(inode,idrag) = term ;
}
}
return 0 ;
}

```

A.5. User-routine to define pressure *user_initialize.c*

```

#include "nphase_struct.h"
#include <math.h>
#include "definitions.h"

int user_initialize()
{
/*-----
routine to initialize variables and set boundary conditions

called from:
initialize

initials      comment
-----*/

real *rhoc=var.rhoc ;

int inode,iface,field,ibf ;

real *rhomix,rad,ubar,seven=7 ;
real Y_reference_location,p_reference_location ;
real Radius=0.02515;
real *tempralloc(),*temprdealloc() ;

entered("user_initialize") ;

// Example: setting hydrostatic pressure in the x-direction
// /* evaluate mixture density */
//
rhomix = tempralloc(NumberNodes) ;

for(inode=0 ; inode<=NumberNodes-1 ; ++inode)
*(rhomix+inode)=VolumeFraction_InternalNode(inode,1)* InputFileDensity(1)
;

if(NumberFields>=2) {
    for(field=2 ; field<=NumberFields ; ++field) {
        for(inode=0 ; inode<=NumberNodes-1 ; ++inode) {

```

```

                *(rhomix+inode)+=
VolumeFraction_InternalNode(inode,field)* InputFileDensity(field);
        }
    }

// initialize pressure to static elevation pressure
Y_reference_location = YCoordinate_PressureBoundary(0) ;
p_reference_location = Pressure_PressureBoundary(0,1) ;
for(inode=0 ; inode<=NumberNodes-1 ; ++inode) {
    Pressure_InternalNode(inode,1)=p_reference_location
        +( YCoordinate_InternalNode(inode) -
Y_reference_location)* *(rhomix+inode) * YGravity ;
}

for(ibf=0 ; ibf<=NumberFaces_PressureBoundary-1; ++ibf) {
    inode=AdjacentNodeNumber_PressureBoundary(ibf) ;
    Pressure_PressureBoundary(ibf,1) = p_reference_location
        +(YCoordinate_PressureBoundary(ibf) -
Y_reference_location)* *(rhomix+inode)* YGravity ;
}

for(ibf=0 ; ibf<=NumberFaces_WallBoundary-1; ++ibf) {
    inode=AdjacentNodeNumber_WallBoundary(ibf) ;
    Pressure_WallBoundary(ibf,1) = p_reference_location
        + ( YCoordinate_WallBoundary(ibf) -
Y_reference_location)* *(rhomix+inode)* YGravity ;
}

    temprdealloc (rhomix) ;

// Example: setting inlet velocity profile to 1/7 turbulent pipe flow
// profile

// for(field=1 ; field<=NumberFields ; ++field) {

//     if(field == 1) ubar=0.844 ;
//     if(field != 1) ubar=0.844;

//     for(ibf=0 ; ibf<=NumberFaces_InletBoundary-1; ++ibf) { //
inlet.nbcface is the total number of inlet boundary faces
//         rad = YCoordinate_InletBoundary(ibf) ;
//         UVelocity_InletBoundary(ibf,field) = 9./7.*ubar*( 1. -
pow((rad/Radius),seven) ) ; // setting u inlet velocity
//     }
// }

    exiting("user_initialize") ;

    return 0 ;
}

```

A.6. Turbulence dispersion force user-routine *user_vfdispforce.c*

```
#include <math.h>
#include "nphase_struct.h"
#include "definitions.h"

int user_vfdispforce(int inondrag)
{
/*-----
   user model for volume fraction dispersion force (nondrag model id
  2, subid 0)

   called from:
   vfdisp_mom

   date          initials    comment
   modified
   09/12/99      spa
   03/01/01      spa          use exp function to decay wall effect
-----*/

int *nondrag_fielda=var.nondrag_fielda ;
int *nondrag_fieldb=var.nondrag_fieldb ;

real *nondrag_usermultiplier=var.nondrag_usermultiplier ;

int field_continuous,field_dispersed ;
int inode,ivar, nstrideb,ibcface ;

real *gradu_cont,*gradv_cont,*gradw_cont ;
real *u_cont,*v_cont,*w_cont ;
real *xc=var.xc;
real xcn;
real *scalar, *gradvf, usermult;
real grad_vel_cont, liquid_vel_mag, *gradient_variable, gravity_mag;
real *grada_disp,*a_disp, vfhat ;
real ctd=1,term,term1,term2,vf,bot,vfmin=0.001 ;
real urel,vrel,wrel,velrelmag2,tke_cap ;
real termu,termv,termw, normx, normy, normz ;
real *debugvar2=var.debugvar2;
real *tempralloc(),*temprdealloc() ;
real *yc=var.yc, ycn;
entered("user_vfdispforce");

// determine continuous and dispersed fields
field_continuous = InterfacialForceContinuousField(inondrag) ;
field_dispersed  = InterfacialForceDispersedField(inondrag) ;
nstrideb = (field_dispersed-1)* NumberNodes;
// determine user multiplier (from input)
usermult = InterfacialForceUserMultiplier(inondrag) ;

// evaluate volume fraction gradient
grada_disp=tempralloc ( NumberNodes*3) ;
a_disp=&VolumeFraction_InternalNode(0,field_dispersed);
```

```

gradient(a_disp,grada_disp,ivar=98,field_dispersed) ;
gradu_cont=tempralloc ( 3* NumberNodes) ;
gradv_cont=tempralloc ( 3* NumberNodes) ;
gradw_cont=tempralloc ( 3* NumberNodes) ;

u_cont=var.u+ (field_continuous-1)* NumberNodes ;
v_cont=var.v+ (field_continuous-1)* NumberNodes ;
w_cont=var.w+ (field_continuous-1)* NumberNodes ;

gradient(u_cont,gradu_cont,ivar=98,field_continuous) ;
gradient(v_cont,gradv_cont,ivar=98,field_continuous) ;
gradient(w_cont,gradw_cont,ivar=98,field_continuous) ;

gradient_variable = tempralloc( NumberNodes) ;

/* turbulent dispersion force */
ctd*= usermult ;
// turbulent dispersion for small bubbles (no tke_cap)

if(field_continuous==1 && field_dispersed == 2){

// loop over all nodes
for(inode=0 ; inode<=NumberNodes-1 ; ++inode) {
// evaluate relative velocity

urel=UVelocity_InternalNode(inode,field_dispersed)-
UVelocity_InternalNode(inode,field_continuous) ;

vrel=VVelocity_InternalNode(inode,field_dispersed)-
VVelocity_InternalNode(inode,field_continuous) ;

wrel=WVelocity_InternalNode(inode,field_dispersed)-
WVelocity_InternalNode(inode,field_continuous) ;
velrelmag2 = urel*urel + vrel*vrel + wrel*wrel ;

gravity_mag=sqrt(XGravity*XGravity+YGravity*YGravity+ZGravity*ZGravi
ty);
// volume fraction numerical treatment

ycn=(yc+inode);
if (ycn>0.0025){
term1 = 9.5*
Density_InternalNode(inode,field_continuous)*(1-
VolumeFraction_InternalNode(inode,field_dispersed))*
VolumeFraction_InternalNode(inode,field_dispersed);
} else { term1 = 0;}
term = ctd*
Density_InternalNode(inode,field_continuous)*
TurbulentKineticEnergy_InternalNode(inode,field_continuous)*
VolumeFraction_InternalNode(inode,field_dispersed);

VolumeFractionSmoothing(inode,field_continuous)+= term ;
VolumeFractionSmoothing(inode,field_dispersed)+= term ;
VolumeFractionSmoothing(inode,field_continuous)+= term1

```

```

        VolumeFractionSmoothing(inode,field_dispersed)+= term1 ;

        term*= NodeVolume_InternalNode(inode) ;
        term1*= NodeVolume_InternalNode(inode) ;

termu= term* *(grada_disp+          inode) ;
termv= term* *(grada_disp+  NumberNodes+inode) -
term1*YGravity/gravity_mag;
termw= term* *(grada_disp+2* NumberNodes+inode) ;

// add entire force to right-hand-side (rhs) of momentum source for
segregated algorithm

SourceTerm_SegregatedSolver(inode,XMomentumSource,field_continuous)+=termu
;
SourceTerm_SegregatedSolver(inode,XMomentumSource,field_dispersed) -=termu
;
SourceTerm_SegregatedSolver(inode,YMomentumSource,field_continuous)+=termv
;
SourceTerm_SegregatedSolver(inode,YMomentumSource,field_dispersed) -=termv
;
SourceTerm_SegregatedSolver(inode,ZMomentumSource,field_continuous)+=termw
;
SourceTerm_SegregatedSolver(inode,ZMomentumSource,field_dispersed) -=termw
;

    }
}

// turbulent dispersion for large bubbles (with tke_cap)
    if(field_continuous==1 && field_dispersed == 3){
// loop over all nodes
        for(inode=0 ; inode<=NumberNodes-1 ; ++inode) {

// evaluate relative velocity

            urel=UVelocity_InternalNode(inode,field_dispersed)-
UVelocity_InternalNode(inode,field_continuous) ;

            vrel=VVelocity_InternalNode(inode,field_dispersed)-
VVelocity_InternalNode(inode,field_continuous) ;

            wrel=WVelocity_InternalNode(inode,field_dispersed)-
WVelocity_InternalNode(inode,field_continuous) ;
                velrelmag2 = urel*urel + vrel*vrel + wrel*wrel ;
            ycn=(yc+inode);
            if (ycn>0.0025){
                term1 = ctd* Density_InternalNode(inode,field_continuous)*
TurbulentKineticEnergy_InternalNode(inode,field_continuous)*
VolumeFraction_InternalNode(inode,field_dispersed);
                term =
term1+9.5*Density_InternalNode(inode,field_continuous)*(1-

```

```

VolumeFraction_InternalNode(inode, field_dispersed))*VolumeFraction_Interna
lNode(inode, field_dispersed);
        } else {
            term = ctd* Density_InternalNode(inode, field_continuous)*
TurbulentKineticEnergy_InternalNode(inode, field_continuous)*
VolumeFraction_InternalNode(inode, field_dispersed);
        }
// volume fraction numerical treatment
        VolumeFractionSmoothing(inode, field_continuous) +=
term ;
        VolumeFractionSmoothing(inode, field_dispersed) +=
term ;

        term*= NodeVolume_InternalNode(inode) ;
        term1*= NodeVolume_InternalNode(inode) ;
termu= term* *(grada_disp+        inode) ;
termv= term* *(grada_disp+ NumberNodes+inode) +
term1*YGravity/gravity_mag ;
termw= term* *(grada_disp+2* NumberNodes+inode) ;

// add entire force to right-hand-side (rhs) of momentum source for
segregated algorithm

SourceTerm_SegregatedSolver(inode, XMomentumSource, field_continuous) +=termu
;
SourceTerm_SegregatedSolver(inode, XMomentumSource, field_dispersed) -=termu
;
SourceTerm_SegregatedSolver(inode, YMomentumSource, field_continuous) +=termv
;
SourceTerm_SegregatedSolver(inode, YMomentumSource, field_dispersed) -=termv
;
SourceTerm_SegregatedSolver(inode, ZMomentumSource, field_continuous) +=termw
;
SourceTerm_SegregatedSolver(inode, ZMomentumSource, field_dispersed) -=termw
;
    }
}

    temprdealloc(grada_disp) ;

    exiting("user_vfdispforce");

    return 0 ;
}

```